Matter

CellPress
OPEN ACCESS

Article

Compositionally complex perovskite oxides: Discovering a new class of solid electrolytes with interface-enabled conductivity improvements

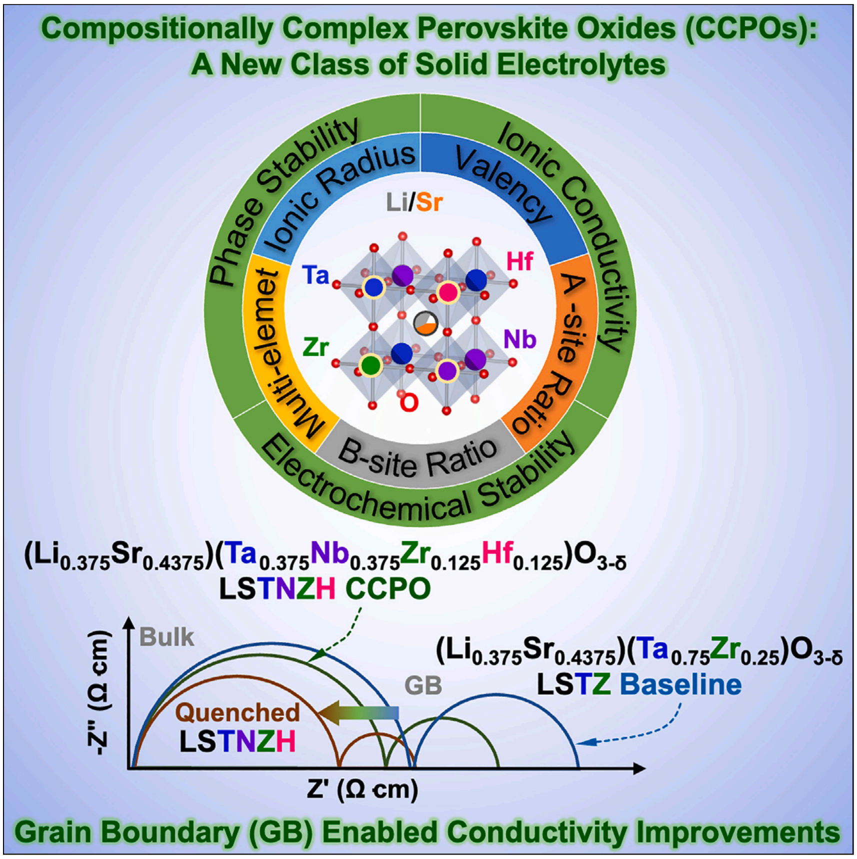

Shu-Ting Ko, Tom Lee, Ji Qi, ..., Shyue Ping Ong, Xiaoqing Pan, Jian Luo

ongsp@eng.ucsd.edu (S.P.O.)
xiaoqinp@uci.edu (X.P.)
jluo@alum.mit.edu (J.L.)

Highlights

Discovered compositionally complex perovskite oxides (CCPOs) as solid electrolytes

Compositionally complex designs can outperform conventional doping

Demonstrated grain-boundary-enabled conductivity improvements

Compositionally complex perovskite oxides (CCPOs) with enhanced conductivity are discovered as an exemplar of compositionally complex solid electrolytes. This study demonstrates that non-equimolar compositionally complex designs can achieve properties beyond the limit of conventional doping. Grain-boundary-enabled conductivity improvements are demonstrated. The materials discovery strategies via simultaneously exploiting non-equimolar complex compositional designs and controls of interfaces and microstructures can be utilized to discover and tailor a broader range of compositionally complex ceramics (CCCs) for energy storage and other applications.

1 **Discovery**
A new material or phenomena

Ko et al., Matter 6, 1–24
July 5, 2023 © 2023 The Author(s). Published by Elsevier Inc.
https://doi.org/10.1016/j.matt.2023.05.035

Please cite this article in press as: Ko et al., Compositionally complex perovskite oxides: Discovering a new class of solid electrolytes with interface-enabled conductivity improvements, Matter (2023), https://doi.org/10.1016/j.matt.2023.05.035

Matter

CellPress
OPEN ACCESS

Article

Compositionally complex perovskite oxides: Discovering a new class of solid electrolytes with interface-enabled conductivity improvements

Shu-Ting Ko,[1,6] Tom Lee,[2,6] Ji Qi,[1,6] Dawei Zhang,[1,6] Wei-Tao Peng,[3,6] Xin Wang,[2] Wei-Che Tsai,[1] Shikai Sun,[2] Zhaokun Wang,[2] William J. Bowman,[2] Shyue Ping Ong,[3,*] Xiaoqing Pan,[2,4,5,*] and Jian Luo[1,3,7,*]

SUMMARY

Compositionally complex ceramics (CCCs), including high-entropy ceramics, offer a vast, unexplored compositional space for materials discovery. Herein, we propose and demonstrate strategies for tailoring CCCs via a combination of non-equimolar compositional designs and control of grain boundaries (GBs) and microstructures. Using oxide solid electrolytes for all-solid-state batteries as an example, we have discovered a class of compositionally complex perovskite oxides (CCPOs) with improved lithium ionic conductivities beyond the limit of conventional doping. For example, we demonstrate that the ionic conductivity can be improved by >60% in $(Li_{0.375}Sr_{0.4375})(Ta_{0.375}Nb_{0.375}Zr_{0.125}Hf_{0.125})O_{3-\delta}$ compared with the $(Li_{0.375}Sr_{0.4375})(Ta_{0.75}Zr_{0.25})O_{3-\delta}$ (LSTZ) baseline. Furthermore, the ionic conductivity can be improved by another >70% via quenching, achieving >270% of the LSTZ. Notably, we demonstrate GB-enabled conductivity improvements via both promoting grain growth and altering GB structures through compositional designs and processing. In a broader perspective, this work suggests new routes for discovering and tailoring CCCs for energy storage and many other applications.

INTRODUCTION

The classical materials discovery methodology typically relies on searching for new stoichiometric compounds, where small amounts of dopants or additives are often introduced to modify or improve properties. The recent emergence of high-entropy ceramics (HECs) with diversifying crystal structures[1–8] unlocks vast compositional spaces with multi-principal (but no dominant) components. Specifically, high-entropy perovskite oxides (HEPOs), which were first reported in 2018,[5] attracted great research interest because of their interesting catalytic,[9] dielectric,[10,11] ferroelectric,[12] magnetic,[13] thermoelectric,[14] magnetocaloric,[15] and electrocaloric[11] properties, as well as promising applications as strongly correlated quantum materials[16] and in solid oxide fuel cells,[17] solar thermochemical hydrogen generation (water splitting),[18] lithium-ion batteries,[19] and supercapacitors.[20] In 2020, Luo and coworkers further proposed to broaden HECs to compositionally complex ceramics (CCCs)[1,21] to consider non-equimolar compositions and short- and long-range orders, which reduce the configurational entropy but are often essential for optimizing or further improving properties. Moreover, controlling the interfaces and microstructures of HECs and CCCs, along with non-equimolar compositional designs

PROGRESS AND POTENTIAL

The recent emergence of high-entropy ceramics and a broader class of compositionally complex ceramics (CCCs) unlocks vast compositional spaces for materials discovery. This study proposes and demonstrates strategies for tailoring CCCs via a combination of non-equimolar compositional designs and control of interfaces and microstructures to discover a new class of compositionally complex solid electrolytes. Consequently, compositionally complex perovskite oxides with enhanced ionic conductivity are unearthed. Notably, this study discovers grain-boundary-enabled conductivity improvements, where compositional designs and processing are utilized to alter microstructures and interfacial structures to improve properties. Promising applications in all-solid-state batteries are envisioned. More generally, these materials discovery strategies can be utilized to discover, design, and tailor a broader range of CCCs for energy storage and many other applications.

Please cite this article in press as: Ko et al., Compositionally complex perovskite oxides: Discovering a new class of solid electrolytes with interface-enabled conductivity improvements, Matter (2023), https://doi.org/10.1016/j.matt.2023.05.035

with aliovalent doping, represents additional (unexplored) opportunities that motivated this study.

Oxide solid electrolytes are promising candidates for building high-energy-density all-solid-state batteries (ASSBs) owing to their electrochemical, thermal, and structural stability.[22] Among the different oxide solid electrolytes, perovskite-type $Li_{0.5}La_{0.5}TiO_3$ (LLTO) drew significant attention owing to its high bulk Li-ion conductivity (σ_b) on the order of 10^{-3} S/cm. Its resistive grain boundaries (GBs), however, constrain its total ionic conductivity (σ_{gb} ~10^{-5} S/cm so that σ_{total} ~10^{-5} S/cm).[23] Furthermore, Ti^{4+} can be reduced to Ti^{3+} at potential below 1.8 V vs. Li/Li^+,[24,25] which transforms LLTO into an electronic conductor that will ultimately short circuit the battery cell.[26] In an attempt to address the shortcomings of LLTO, Chen et al. reported perovskite $Li_{0.375}Sr_{0.4375}Ta_{0.75}Zr_{0.25}O_3$ (LSTZ) holding one order of magnitude higher GB ionic conductivity (σ_{gb} ~10^{-4} S/cm) than that of LLTO, a σ_{bulk} of 2×10^{-4} S/cm, and a wider electrochemical stability window down to 1.0 V vs. Li/Li^+.[27] LSTZ has shown better performance compared with LLTO, but its ionic conductivity is still lower than other inorganic solid electrolyte candidates,[28,29] calling for innovative strategies to improve.

In general, ABO_3 perovskite oxides have broad applications. It is known that aliovalent doping can tune structures (e.g., ordering of A sites,[30,31] concentration of A-site vacancies,[32] lattice parameter[33,34]) and influence properties including Li-ion conductivity. To date, the majority of the studies have been limited to single and co-doping. The amount of dopants is typically below 10 mol % in A- or B-site sublattices to avoid precipitation.[33,35] The perovskite structure can tolerate a wide range of cation dopants following a criterion using Goldschmidt's tolerance factor,[36] which renders it promising as a model system for exploring complex or high-entropy compositions. However, only a single study explored HEPOs as a solid electrolyte, where the reported ionic conductivity was lower than that of baseline material LLTO.[37] In fact, the field of high-entropy solid electrolytes remains largely unexplored, with only few prior reports.[37–39] Notably, a recent study demonstrated a high-entropy mechanism to improve ionic conductivity, achieving 2.2×10^{-5} S/cm in $Li(Ti,Zr,Sn,Hf)_2(PO_4)_3$, which represents substantial improvements from their base materials (thereby being promising).[40,41] Herein, we discovered a new class of compositionally complex perovskite oxides (CCPOs) to achieve (an order of magnitude higher) 2.56×10^{-4} S/cm total ionic conductivity with improvements (from the LSTZ baseline) through not only the bulk compositional complexity but also microstructure and GB effects.

Specifically, we discovered a class of LSTZ-derived compositionally complex solid electrolytes (CCPOs) in this study. We further revealed the phase-microstructure-property relationship to enable us to achieve improved total ionic conductivity, achieving >270% of the state-of-the-art LSTZ baseline, yet with comparable electrochemical stability. In addition, we showed GB-enabled conductivity improvements, through both promoting grain growth and altering the GB structure and segregation profile via compositional designs and materials processing. To investigate the underlying mechanisms, aberration-corrected advanced microscopy and atomistic simulations using a state-of-the-art active learning moment tensor potential (MTP) and additional density functional theory (DFT) calculations were employed. This work highlights the significance of microstructure and GB controls of CCCs in boosting their ionic conductivities, in addition to non-equimolar compositional designs, which points to a new direction to design and tailor compositionally complex solid electrolytes and potentially many other functional CCCs.

[1]Materials Science and Engineering Program, University of California, San Diego, La Jolla, CA 92093, USA

[2]Department of Materials Science and Engineering, University of California at Irvine, Irvine, CA 92697, USA

[3]Department of NanoEngineering, University of California, San Diego, La Jolla, CA 92093, USA

[4]Department of Physics and Astronomy, University of California at Irvine, Irvine, CA 92697, USA

[5]Irvine Materials Research Institute, University of California at Irvine, Irvine, CA 92697, USA

[6]These authors contributed equally

[7]Lead contact

*Correspondence:
ongsp@eng.ucsd.edu (S.P.O.),
xiaoqinp@uci.edu (X.P.), jluo@alum.mit.edu (J.L.)

https://doi.org/10.1016/j.matt.2023.05.035

Please cite this article in press as: Ko et al., Compositionally complex perovskite oxides: Discovering a new class of solid electrolytes with interface-enabled conductivity improvements, Matter (2023), https://doi.org/10.1016/j.matt.2023.05.035

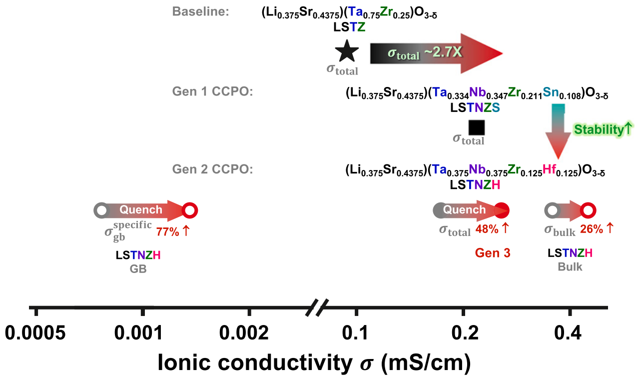

Figure 1. Several generations of CCPOs discovered in this work, benchmarked with the LSTZ baseline

The first-generation CCPO LSTNZS (square) shows a total ionic conductivity of 0.218 mS/cm, which is ~2.3× the 0.094 mS/cm of the LSTZ baseline (star), but the electrochemical stability of the Sn-containing LSTNZS is compromised. The second-generation Hf-containing (and Sn-free) CCPO LSTNZH (gray circle) shows comparable electrochemical stability with LSTZ and a total ionic conductivity of 0.151 mS/cm, which can be further enhanced through quenching (red circle) to 0.256 mS/cm. The improvement via quenching is primarily due to the increase of specific GB conductivity (by 77%, albeit the bulk conductivity is also improved moderately by 26%). Overall, the total conductivity of the air-quenched LSTNZH is ~2.7× that of the LSTZ baseline.

RESULTS AND DISCUSSION

Overview: CCPOs as solid electrolytes

In this study, we synthesized 28 different compositions of CCPOs (through high-energy ball milling and sintering at 1,300°C for 12 h in air; see experimental procedures) as a new class of lithium-ion solid electrolytes. The key results of three series of Sn-containing (Li,Sr)(Ta,Nb,Zr,Sn)$O_{3-\delta}$ (LSTNZS) CCPOs and two series of Hf-containing (Li,Sr)(Ta,Nb,Zr,Hf)$O_{3-\delta}$ (LSTNZH) CCPOs are summarized in supplemental information (Tables S1–S3). δ represents oxygen non-stoichiometry in perovskites. We showed that enhanced ionic conductivities, in comparison with the state-of-art LSTZ baseline, can be attained in these CCPOs via compositional designs and controlling GBs and microstructures, while maintaining comparable electrochemical stability.

Figure 1 presents an outline of several generations of CCPOs discovered in this study, in comparison with the LSTZ baseline. In the first generation, the best Sn-containing LSTNZS CCPO $(Li_{0.375}Sr_{0.4375})(Ta_{0.334}Nb_{0.347}Zr_{0.211}Sn_{0.108})O_{3-\delta}$ shows total ionic conductivity >2.3× higher than that of the LSTZ baseline; however, its electrochemical stability is compromised due to the presence of redox-active Sn (Figure S1). In the second generation, an Hf-containing (and Sn-free) LSTNZH CCPO $(Li_{0.375}Sr_{0.4375})(Ta_{0.375}Nb_{0.375}Zr_{0.125}Hf_{0.125})O_{3-\delta}$ shows electrochemical stability comparable with LSTZ with slightly lower ionic conductivity (but >60% improvement from the LSTZ baseline), which can be further improved to achieve 0.256 mS/cm total ionic conductivity or 270% of the LSTZ baseline via quenching. A notable discovery of this study is GB-enabled conductivity improvements through both promoting grain growth and altering the GB structure and segregation profile through compositional designs and materials processing. For example, the observed conductivity improvement via quenching is primarily from an increase in specific (true) GB ionic conductivity (Note S1),[42] resulting from changes in the GB compositional profile and structure, as shown by aberration-corrected (AC) scanning transmission electron microscopy (STEM) presented and discussed in a subsequent section.

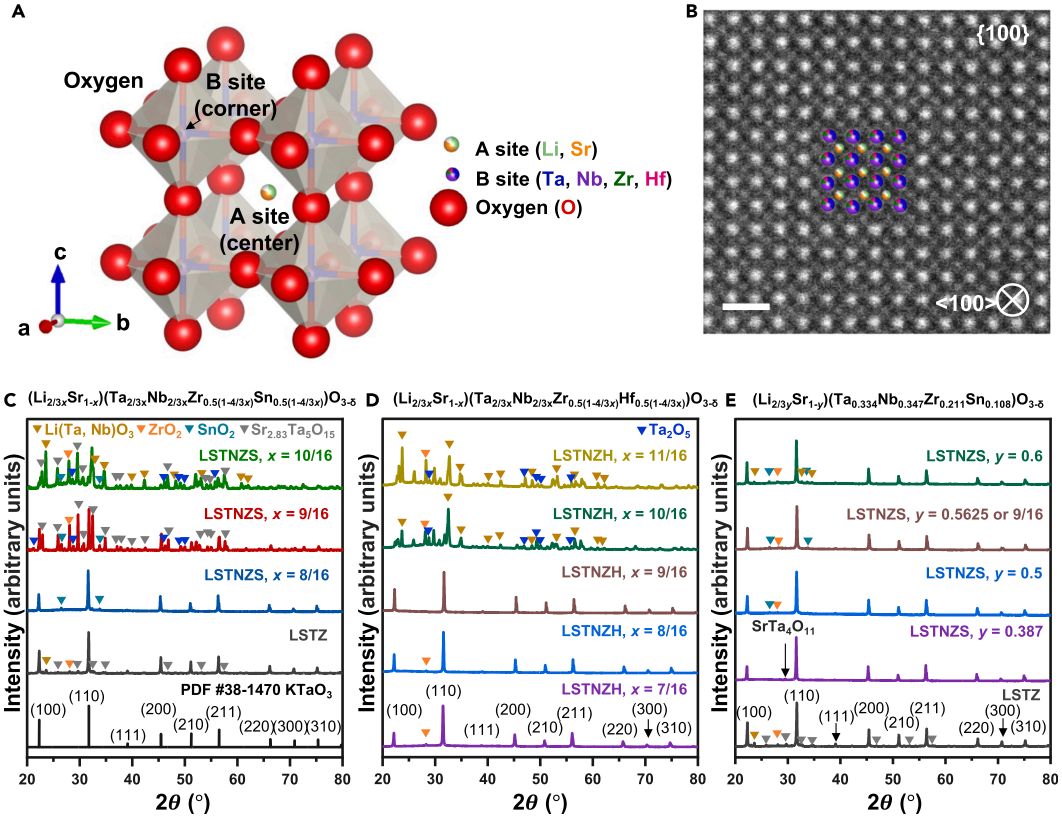

Figure 2. XRD patterns and crystal structure of new series of LSTNZS and LSTNZH CCPOs

(A) The crystal structure model obtained from XRD refinement of LSTNZH ($x = 9/16$). The A sites are occupied by Li and Sr cations, while the B sites are occupied by Ta, Nb, Zr, and Sn/Hf cations.

(B) The atom arrangement of LSTNZH ($x = 9/16$) bulk in {100} plane family shown in an HAADF-STEM image (scale bar, 1 nm). The atoms are labeled in accordance with the model in (A).

(C–E) XRD patterns of (C) the LSTNZS x series, benchmarked with LSTZ baseline, and (D) the LSTNZH x series CCPOs, respectively, both following a general formula $[Li_{(2/3)x}Sr_{1-x}][(5B)_{(4/3)x}(4B)_{1-(4/3)x}]O_{3-\delta}$, and (E) the LSTNZS y series with optimized B-site cation ratio (fixed) and changing A-site cation stoichiometry following $[Li_{(2/3)y}Sr_{1-y}][Ta_{0.334}Nb_{0.347}Zr_{0.211}Sn_{0.108}]O_{3-\delta}$.

Compositional designs and composition-phase-property relationship

Figure 2A displays a schematic of the CCPO unit cell of the ABO_3 perovskite (A-site-centered view). The atomic-resolution high-angle annular dark-field (HAADF) STEM image of a representative LSTNZH CCPO is shown in Figure 2B and its X-ray diffraction (XRD) pattern is shown in Figure 2D, which confirmed the cubic perovskite structure.

Next, we discuss the compositional designs of CCPOs and the resulting phase stability (any secondary phases) and properties (conductivities).

Expanding on a simpler compositional design for LSTZ,[27] we first designed our "x series" CCPOs following a general formula $[Li_{(2/3)x}Sr_{1-x}(V''_A)_{(1/3)x}][(5B)_{(4/3)x}(4B)_{1-(4/3)x}]O_{3-\delta}$. Here, the A site is occupied by Li^+, Sr^{2+}, and A-site vacancies V''_A (in the Kröger–Vink notation), and the B site is occupied by a (presumably random) mixture of 5B (5+ B-site) cations, which are equal moles of Ta^{5+} and Nb^{5+} cations, and 4B (4+ B-site) cations, which are equal moles of Zr^{4+} and Sn^{4+} (or Hf^{4+}) cations for LSTNZS (or LSTNZH). Omitting V''_A for brevity, the chemical formulas are $(Li_{2/3x}Sr_{1-x})(Ta_{2/3x}Nb_{2/3x}Zr_{0.5(1-4/3x)}Sn_{0.5(1-4/3x)}O_{3-\delta}$ for the x series of LSTNZS and $(Li_{2/3x}Sr_{1-x})(Ta_{2/3x}Nb_{2/3x}Zr_{0.5(1-4/3x)}Hf_{0.5(1-4/3x)}O_{3-\delta}$ for the x series of LSTNZH.

Please cite this article in press as: Ko et al., Compositionally complex perovskite oxides: Discovering a new class of solid electrolytes with interface-enabled conductivity improvements, Matter (2023), https://doi.org/10.1016/j.matt.2023.05.035

Here, we first investigated the (primary vs. secondary) phase formation and stability using XRD. Figures 2C and 2D present the XRD patterns of x series of LSTNZS and LSTNZH, respectively. For $x = 8/16$, the Sn-containing LSTNZS shows a cubic perovskite structure in the space group Pm $\bar{3}$ m, which matches the crystal structure of $KTaO_3$ (PDF #38–1,470) and that of LSTZ. The amounts of secondary phases increase as the x value increases to 9/16 and higher. At $x \geq 9/16$, $LiNbO_3$-prototyped rhombohedral structure (space group R3c) and $Sr_{2.83}Ta_5O_{15}$-prototyped with tetragonal structure (space group P4/mbm) formed, which consequently triggered the precipitation of secondary SnO_2 and ZrO_2 phases. The corresponding phase separation is evident in scanning electron microscopy (SEM) energy-dispersive X-ray spectroscopy (EDS) maps in Figure S2. The Hf-containing LSTNZH system shows a wider single-phase range of up to $x = 9/16$, with only trace amounts of ZrO_2 secondary phase found. At $x > 9/16$, however, the primary phase becomes $LiNbO_3$-prototyped rhombohedral instead of the cubic perovskite phase.

Based on these results, we conclude the primarily single-phase range of CCPOs in the x series is mainly determined by the x value, and the threshold (for the appearance of large amounts of secondary phases) depends on the difference in cation ionic radii. The Sn-containing LSTNZS x series has a lower threshold ($x \geq 9/16$) than the Hf-containing LSTNZH x series, which can be attributed to the larger difference in ionic radii between Sn^{4+} and Zr^{4+} (~4.17%) than that between Hf^{4+} and Zr^{4+} (1.39%), calculated using Shannon ionic radii (Table S4).[43] This large ionic radius difference makes it more difficult for LSTNZS to form stable cubic perovskite solid solution at $x \geq 9/16$ and results in precipitation of the secondary SnO_2 and ZrO_2 phases. To further test this hypothesis, LSTNZS ($x = 9/16$) was benchmarked with Nb and Sn co-doped LSTZ counterparts in Figure S3, which again implies that the poor single-phase formation is due to the large ionic radii difference on the B site.

To further improve the single-phase formability of the LSTNZS system, we adopted a "natural selection" composition optimization strategy described in the supplemental information (Figures S4–S6; Tables S5 and S6; Note S2) to synthesize the composition of the primary phase guided from SEM-EDS compositional quantification results of the single-phase region of the prior generation, in an iterative procedure. Accordingly, an LSTNZS "y series" with the optimal B-site cation ratio $(Li_{2/3y}Sr_{1-y})(Ta_{0.334}Nb_{0.347}Zr_{0.211}Sn_{0.108})O_{3-\delta}$ was developed. XRD patterns of the LSTNZS y series (Figure 2E) exhibit improved single-phase formation compared with the LSTNZS x series. For LSTNZS ($y = 0.6$), the main secondary phase was determined to be $Li(Ta,Nb)O_3$. The design workflows of x and y series are illustrated in Figure S7.

For subsequent characterizations, we will focus on the Sn-containing LSTNZS y series and Hf-containing LSTNZH x series, which are the two best series obtained in this study.

To quantify the primary phase fractions, we performed Rietveld refinements of XRD patterns of LSTNZS y series (Figure S8) and LSTNZH x series (Figure S9). The results are summarized in Table S7. We also quantify the primary phase fractions from SEM-EDS maps (Figure S10) and the results are shown in Figures 3A and 3B for the Sn-containing LSTNZS y series and the Hf-containing LSTNZH x series, respectively. Figure S11 compares results obtained from the two methods, which are largely consistent. The exception is for LSTNZH ($x = 10/16$), where the refinement accuracy is low due to the presence of multiple secondary phases and peak overlaps and quantification from SEM-EDS maps is likely more accurate.

Please cite this article in press as: Ko et al., Compositionally complex perovskite oxides: Discovering a new class of solid electrolytes with interface-enabled conductivity improvements, Matter (2023), https://doi.org/10.1016/j.matt.2023.05.035

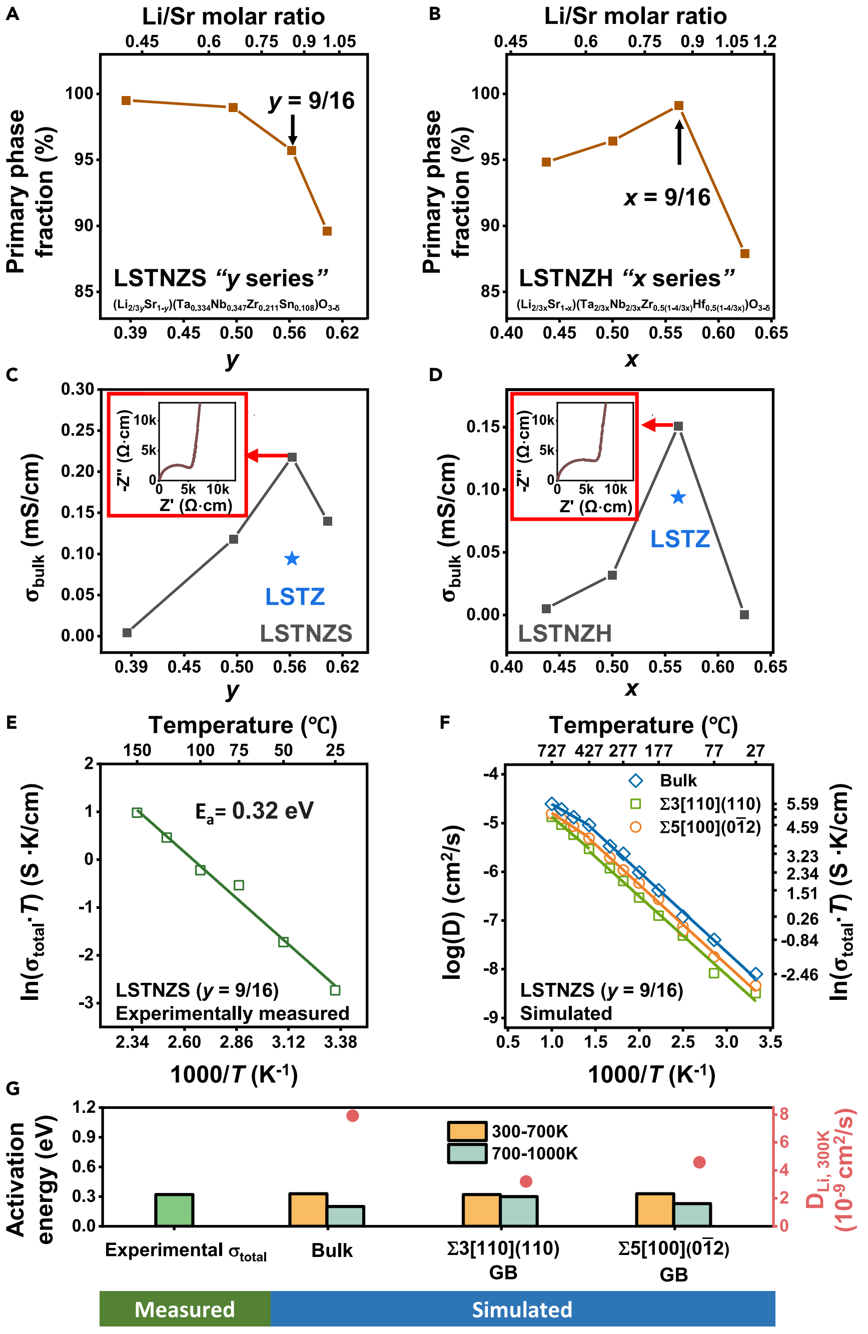

Figure 3. Plots of primary phase fraction and bulk ionic conductivity for the LSTNZS *y* series [$(Li_{2/3y}Sr_{1-y})(Ta_{0.334}Nb_{0.347}Zr_{0.211}Sn_{0.108})O_{3-\delta}$] and the LSTNZH *x* series [$(Li_{2/3x}Sr_{1-x})(Ta_{2/3x}Nb_{2/3x}Zr_{0.5(1-4/3x)}Hf_{0.5(1-4/3x)})O_{3-\delta}$], experimentally measured Arrhenius plot vs. simulated Li-ion diffusivities for LSTNZS (*y* = 9/16)

(A and B) The areal fraction of the primary phase for (A) the LSTNZS *y* series and (B) the LSTNZH *x* series, quantified from elemental EDS maps (that are consistent with XRD Rietveld refinement as shown in Figure S11), as function of *y* or *x* values (bottom axis) and Li/Sr ratio (top axis).

(C and D) Correlation plots of fitted σ_{bulk} vs. *y* or *x* values for (C) LSTNZS *y* series and (D) LSTNZH *x* series. The σ_{bulk} is optimized when *y* or *x* = 9/16 or 0.5625 for both the Sn-containing LSTNZS *y* series and the Hf-containing LSTNZH *x* series. The total conductivities of two series are benchmarked with the LSTZ baseline (star). Insets are Nyquist plots.

Please cite this article in press as: Ko et al., Compositionally complex perovskite oxides: Discovering a new class of solid electrolytes with interface-enabled conductivity improvements, Matter (2023), https://doi.org/10.1016/j.matt.2023.05.035

Figure 3. *Continued*

(E) The Arrhenius plot of the experimentally measured total ionic conductivity for LSTNZS ($y = 9/16$) in the temperature range from 25°C to 150°*C*.

(F) The Arrhenius plot of Li diffusivity calculated using the bulk model and two selected LSTNZS ($y = 9/16$) GBs equilibrated with MC/MD simulations at 1,573 K.

(G) The corresponding $D_{\mathrm{Li,\ 300K}}$ (right y axis) and activation energies (left y axis).

In addition, we measured the Li-ion conductivities of the as-synthesized specimens. Figure 3C illustrates the influence of the compositional variable y (that correlates with the Li^+ concentration, $\frac{2}{3}y$, and the V_A'' concentration, $\frac{1}{3}y$, in the A site) on the bulk ionic conductivity σ_{bulk} (fitted from the measured impedance spectra by the model discussed in Note S1) of the Sn-containing LSTNZS y series. When $y = 0.387$, $\sigma_{\mathrm{bulk}}^{\mathrm{LSTNZS}}$ is 0.004 mS/cm (the lowest). As y increases to 0.5, $\sigma_{\mathrm{bulk}}^{\mathrm{LSTNZS}}$ is improved by two orders of magnitude to 0.118 mS/cm. The bulk ionic conductivity is maximized at $y = 9/16$, even with the increase of secondary phase fractions. Hence, the change of $\sigma_{\mathrm{bulk}}^{\mathrm{LSTNZS}}$ is dominant by A-site carrier and vacancy amount (rather than phase purities) at $y \leq 9/16$ region. In contrast, the influence of secondary phases becomes dominant when $y > 9/16$. Although the nominal A-site carrier and vacancy amount are the highest at $y = 0.6$ in Figure 3C, the existence of $\mathrm{Sr_{2.83}Ta_5O_{15}}$, $\mathrm{LiTaO_3}$, and $\mathrm{LiNbO_3}$ secondary phases indicates the actual Li^+ in the main phase is less than the nominal amount. Therefore, the $\sigma_{\mathrm{bulk}}^{\mathrm{LSTNZS}}$ value reduces to 0.14 mS/cm at $y = 0.6$. The maximum of $\sigma_{\mathrm{bulk}}^{\mathrm{LSTNZS}}$ is 0.218 mS/cm at $y = 9/16$, which is higher than that of optimal LSTNZS x series composition ($x = 8/16$; 0.11 mS/cm).

Given that both samples exhibit similar phase stability (LSTNZS, $y = 9/16$ vs. $x = 8/16$), the improvement can be attributed to the higher A-site carrier and vacancy concentration while maintaining cubic perovskite structure. To justify the selection of B-site stoichiometry that gives optimal ionic conductivity, an additional LSTNZS "w series" was fabricated following the formula $\mathrm{(Li_{0.375}Sr_{0.4375})(Ta_{0.334}Nb_{0.347}Zr_{0.319\text{-}\mathit{w}}Sn_{\mathit{w}})O_{3\text{-}\delta}}$, where w variable dictates the Sn cation fraction on the B site. The results shown in Figures S12A and S12C indicate the improvement of both phase stability and $\sigma_{\mathrm{bulk}}^{\mathrm{LSTNZS}}$ upon increasing the Sn/Zr fraction until more $\mathrm{SnO_2}$ secondary phase precipitates. Furthermore, the lattice constant of the primary phase reduces linearly with w (the Sn fraction on the B site), which is consistent with the solid solution formation (Figure S13). Further discussion can be found in supplemental information. Table S1 summarizes the results for the three Sn-containing LSTNZS series, which shows that $y = 9/16$ in the y series is the composition exhibiting the highest ionic conductivity (0.218 mS/cm) in all Sn-containing LSTNZS specimens made in this study.

Likewise, Figure 3D shows the influence of the compositional variable x (which is again equal to the total Li^+ and V_A'' concentrations in the A site) on the bulk conductivity σ_{bulk} of the LSTNZH series. The measured $\sigma_{\mathrm{bulk}}^{\mathrm{LSTNZH}}$ value increases as x increases from 7/16 to 9/16, indicating an increase in the ionic conductivity with concentration of Li^+ and Sr vacancies at the single-phase stable regime. Beyond the threshold at $x = 9/16$, $\sigma_{\mathrm{bulk}}^{\mathrm{LSTNZH}}$ decreases again due to the presence of secondary phases shown in Figure 3B. Similar to LSTNZS, the optimal A-site ratio takes place at the value where the total A-site charge carrier and vacancy amount equals 9/16. Table S2 displays the properties for the LSTNZH series discussed above.

Table 1 provides a summary of compositions, sintering conditions, and total ionic conductivity values of representative samples (of optimized compositions) in the

Please cite this article in press as: Ko et al., Compositionally complex perovskite oxides: Discovering a new class of solid electrolytes with interface-enabled conductivity improvements, Matter (2023), https://doi.org/10.1016/j.matt.2023.05.035

Table 1. Chemical composition, sintering condition, and total ionic conductivity for the optimized LSTNZS, LSTNZH, and LSTZ in this work, benchmarked with LSTZ-related compounds and LLTO from the literature

Composition	Sintering condition	σ_{total} (mS/cm)	Reference
$(Li_{0.332}Sr_{0.5})(Ta_{0.334}Nb_{0.347}Zr_{0.211}Sn_{0.108})O_{3-\delta}$	1,300°C, 12 h	0.218	this work
$(Li_{0.375}Sr_{0.4375})(Ta_{0.375}Nb_{0.375}Zr_{0.125}Hf_{0.125})O_{3-\delta}$	1,300°C, 12 h air quenched	0.151 0.256	this work
$(Li_{0.375}Sr_{0.4375})(Ta_{0.75}Zr_{0.25})O_{3-\delta}$	1,300°C, 12 h	0.094	this work
$(Li_{0.375}Sr_{0.4375})(Ta_{0.75}Zr_{0.25})O_{3-\delta}$	1,300°C, 15 h	0.08	Chen et al.[27]
$(Li_{0.375}Sr_{0.4375})(Nb_{0.75}Zr_{0.25})O_{3-\delta}$	1,200°C, 15 h	0.02	Yu et al.[44]
$(Li_{0.375}Sr_{0.4375})(Ta_{0.75}Sn_{0.25})O_{3-\delta}$	1,450°C, 15 h	0.046	Thangadurai et al.[46]
$(Li_{0.375}Sr_{0.4375})(Nb_{0.75}Sn_{0.25})O_{3-\delta}$	1,450°C, 15 h	0.00182	Thangadurai et al.[46]
$(Li_{0.34}La_{0.51})TiO_{3-\delta}$	1,350°C, 6 h	0.02	Inaguma et al.[47]

All specimens, except for the one labeled "air-quenched," were furnace-cooled.

present work compared with the results of LSTZ-related compounds reported in the literature.[27,44–47]

Complementary to Nyquist plots, we further conducted the distribution of relaxation time (DRT) analysis to deconvolute resistor–capacitor (RC) circuit components (polarization processes) involved.[48–51] According to the overlay of DRT peaks with Bode plots in Figure S14, CCPOs show polarization processes (P_1 and P_2) at only high-frequency regime (10^6 Hz), which are assigned to the responses from bulk. In contrast, additional polarization response is presented in the LSTZ at low-frequency regime (10^4 Hz), which may come from GB or resistive secondary phase components that requires further investigation. It is worth noting that only one semicircle is shown on the Nyquist plot for these CCPOs (Figures 3C, 3D, and S15) and no DRT peaks exists at the low-frequency regime. Thus, the GB contribution is not the determining factor constraining the total ionic conductivity (a desirable feature), which is different from the case in the well-known $Li_{0.5}La_{0.5}TiO_3$ ($\sigma_{gb} \approx \sigma_{total} \approx 10^{-5}$ S/cm).[23]

Temperature-dependent conductivity: Experiments vs. simulations

Temperature dependence of ionic conductivity and Li diffusivity for LSTNZS (y = 9/16) were obtained by experiments and simulations, respectively, and compared. Figure 3E shows the Arrhenius plot measured in the temperature range from 25°C to 150°C with the calculated activation energy, E_a, of ionic conductivity of 0.32 eV (see experimental procedures).

Since only one semicircle is observed in the experimentally measured impendence spectrum, Li diffusivities (D_{Li}) of the bulk and GB components were simulated to better understand the role of each. An MTP for LSTNZS (y = 9/16) is fitted using an active learning strategy and subsequent MD simulations were performed on three equilibrated structures, i.e., bulk, twist $\Sigma3\,[110](110)$ GB, and symmetric tilt $\Sigma5\,[100](0\bar{1}2)$ GB to obtain the Arrhenius plots in Figure 3F. It can be observed that, regardless of the temperature, the magnitude of D_{Li} follows the order: bulk > simple twist $\Sigma3\,[110](110)$ GB > symmetric tilt $\Sigma5\,[100](0\bar{1}2)$ GB.

To convert the simulated Li diffusivity to ionic conductivity at temperature T, we use the Nernst-Einstein equation:

$$\sigma(T) = \frac{\rho Z^2 F^2}{RT} \frac{D^*(T)}{H_R} \qquad \text{(Equation 1)}$$

where ρ is the molar density of diffusing ions in the unit cell, and z, F, and R are the charge of Li^+ ions ($z = 1$), the Faraday constant, and the gas constant, respectively.

D^* is the tracer diffusion coefficient and H_R is the haven ratio ($H_R = D^*/D_{Li}$), and, in line with previous studies,[52–57] it is set as unity in this study.

At 300 K, the simulated bulk ionic conductivity is 0.285 mS/cm, matching well with the experimentally measured value of 0.218 mS/cm. Furthermore, the simulated E_a of bulk D_{Li}/σ is 0.33 eV, also matching well with the experimentally obtained value of 0.32 eV. The activation energy data are summarized in Figure 3G and Table S8.

A slightly lower activation energy occurs at and above 700 K, comparable with the non-Arrhenius behavior observed in the LSTZ.[53] In addition, D_{Li} at low-Σ GBs is in the same order of magnitude as D_{Li} in bulk, which matches with the reference LSTZ and differs significantly from that in LLTO. The origin of low GB resistance in LSTZ has been reported in our previous study.[53] It is worth mentioning that the Li diffusivities at GB and bulk of LSTNZS ($y = 9/16$) are similar to those of LSTZ, while GB resistance of LSTNZS ($y = 9/16$) could not be measured in Nyquist plots. Thus, the difference in microstructure between LSTZ and CCPOs likely plays a role in the observed ionic conductivity enhancement.

Evaluation of a high-entropy mechanism on the bulk conductivity

Most recently, a high-entropy mechanism was proposed to lower the energy difference between two different Li sites via high-entropy mixing at the transition metal sites and thereby effectively decreases diffusion barriers and improves ionic conductivities for one to two orders of magnitude.[40] To examine and evaluate this mechanism in our specific CCPOs, the excess energies are calculated to evaluate the energy difference between atomic energy and the averaged atomic energy of all atoms in the system (Note S3). Figure S16 shows the narrower range of distribution of excess energies in LSTNZS ($y = 9/16$) than that in LSTZ, which indicates lower energy differences between different atom sites of same elements. However, in our LSTNZS ($y = 9/16$), we observed comparable activation energy with that of LSTZ. We attribute this to the fact that there is just one type of Li site in the perovskite structure. Therefore, the high-entropy effect has minimal effect on the activation energy in our CCPOs. For future material designs with the aim of achieving lower diffusion barriers, this high-entropy mechanism can be more helpful for materials with different Li sites.

Conductivity improvements via enhanced grain growth: The microstructure effect

To investigate microstructures of the CCPOs, electron backscattered diffraction (EBSD) in SEM was used to obtain information on grain sizes and orientations. Figures 4A, 4B, and 4C present the orientation maps of representative regions in the LSTZ, LSTNZS ($y = 9/16$), and LSTNZH ($x = 9/16$) pellets along with their corresponding grain size distribution statistics (Figures 4D–4F). The color-coded inverse pole figures (Figures 4A–4C) indicate both LSTZ and the CCPOs experienced isotropic grain growth and the resulting pellets consisted of largely randomly oriented grains (Figure S17A). However, both LSTNZS ($y = 9/16$, ~9.5 μm) and LSTNZH ($x = 9/16$, ~10.7 μm) have average grain size that are three times greater than that of the LSTZ reference (~2.9 μm). Additionally, their larger standard deviations (SDs) translate to a broader distribution in grain sizes, which correspond to larger kurtosis (sharpness) and skewness (asymmetry) values. Notably, the maxima of grain sizes are ~51.5 μm (LSTNZS) and ~64.4 μm (LSTNZH), respectively, in CCPOs, which indicate faster grain growth. The grain size enlargement effectively reduces the overall volume fraction of GBs. As a result, the total ionic conductivities are primarily determined by the bulk conductivity for CCPOs. Thus, only a single

Please cite this article in press as: Ko et al., Compositionally complex perovskite oxides: Discovering a new class of solid electrolytes with interface-enabled conductivity improvements, Matter (2023), https://doi.org/10.1016/j.matt.2023.05.035

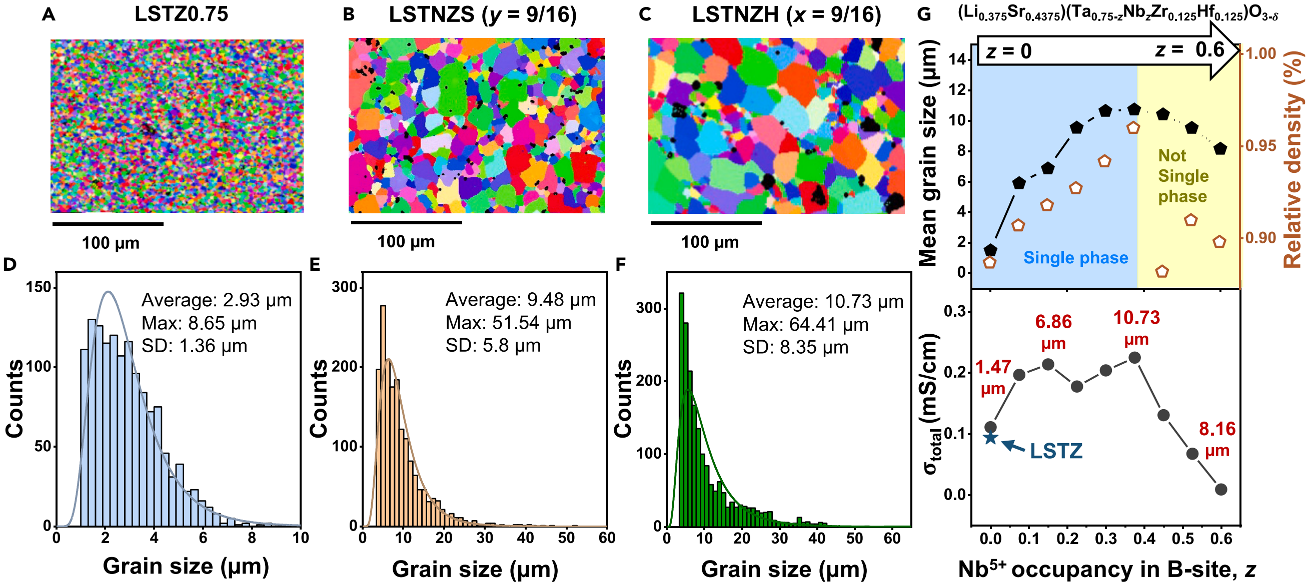

Figure 4. The inverse pole figures of EBSD; grain size statistics of LSTZ, LSTNZS (y = 9/16), and LSTNZH (x = 9/16); and the correlation plots of mean grain size and total ionic conductivity with the Nb^{5+} occupancy

(A–F) The inverse pole figures along the normal direction of (A) LSTZ, (B) LSTNZS (y = 9/16), and (C) LSTNZH (x = 9/16) pellets. The corresponding grain size distribution histograms of (D) LSTZ, (E) LSTNZS (y = 9/16), and (F) LSTNZH (x = 9/16) extracted from (A)–(C), respectively.

(G) The correlation of mean grain size (top left y axis), relative density (top right y axis), phase stability (single phase with bule shade; not a single phase with yellow shade), and total ionic conductivity (bottom left y axis) with the Nb^{5+} occupancy (z in $(Li_{0.375}Sr_{0.4375})(Ta_{0.75-z}Nb_zZr_{0.125}Hf_{0.125})O_{3-\delta}$) in B site.

semicircle is observed in the Nyquist plots of measured impedance spectra (Figures 3C and 3D).

To further probe the origin of larger grain sizes in CCPOs, an additional "z series" of LSTNZH $(Li_{0.375}Sr_{0.4375})(Ta_{0.75-z}Nb_zZr_{0.125}Hf_{0.125})O_{3-\delta}$, where only the Ta/Nb ratio was varied and all other cations are kept to the same stoichiometry as that in LSTNZH (x = 9/16), were synthesized and characterized. The Nb^{5+} substitution shows an independent relationship with the lattice constant in Figure S18 because of the identical ionic radii of Ta^{5+} and Nb^{5+} (Table S4). Figure 4G plots the measured mean grain size, relative density, and total ionic conductivity of $(Li_{0.375}Sr_{0.4375})(Ta_{0.75-z}Nb_zZr_{0.125}Hf_{0.125})O_{3-\delta}$ against z (i.e., the Nb fraction on the B site). In general, all three parameters (grain size, relative density, and total ionic conductivity) increase with the Nb fraction z up to $z = 0.375$. At $z > 0.375$, a single phase is no longer maintained, and all three parameters generally decrease with the further increasing Nb fraction z. The characterization of phase stability, grain size distribution, and ionic conductivity are summarized in Figures S19–S22. These results suggest that Nb^{5+} substitution in B site promotes grain growth and broadens the grain size distribution, coincident with the ionic conductivity enhancement until the single-phase stability threshold. The large grains are homogeneously distributed throughout the samples, as shown in Figure S20. Nb_2O_5 is known as a sintering additive and has been reported to promote grain growth.[58,59] In fact, single crystals are favorable for improving total ionic conductivity and enhancing material rigidity by completely eliminating GBs.[60,61] However, the cost of growing single crystals makes this approach impractical for large-scale manufacturing. Here, our series of $(Li_{0.375}Sr_{0.4375})(Ta_{0.75-z}Nb_zZr_{0.125}Hf_{0.125})O_{3-\delta}$ demonstrates a simple, cost-effective way to decrease volume fraction of GBs and increase ionic conductivity via the addition of Nb_2O_5 to promote grain growth.

Please cite this article in press as: Ko et al., Compositionally complex perovskite oxides: Discovering a new class of solid electrolytes with interface-enabled conductivity improvements, Matter (2023), https://doi.org/10.1016/j.matt.2023.05.035

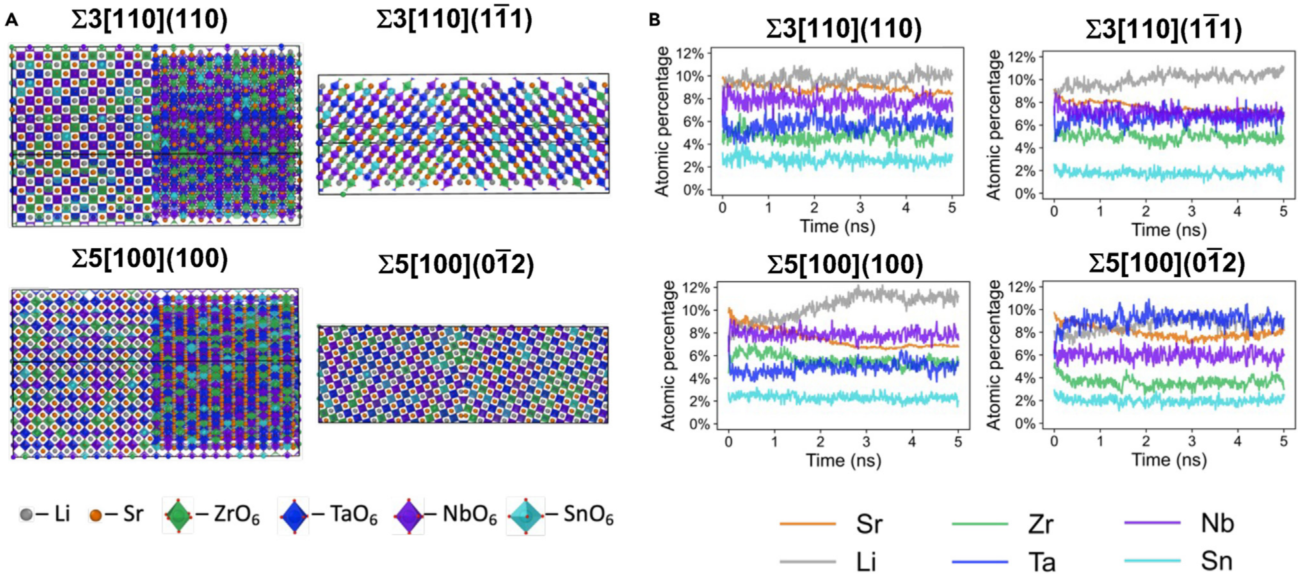

Figure 5. MC/MD simulated GB structures of LSTNZS (*y* = 9/16) based on active learning MTP

(A) Four GB structures of LSTNZS (*y* = 9/16) before MC/MD simulations were constructed with large-scale GB models with over 10,000 atoms. Elements on A and B sites are randomly assigned. The exact geometric information of those GB models is provided in Table S9.

(B) The evolution of the atomic percentage of cations at GB regions of the four GB models during the MC/MD simulations at 1,573 K.

The beneficial effects of adding Nb_2O_5 to promote grain growth in CCPOs can be attributed to the relative low melting temperature of Nb_2O_5 (1,512°C), in comparison with other B-site oxide components: ZrO_2 (2,715°C), HfO_2 (2,758°C), and Ta_2O_5 (1,871°C). Here, we hypothesize that segregation of a relatively low-melting component Nb_2O_5 can induce GB premelting like interfacial structures (liquid-like complexion) to promote GB kinetics, akin to those observed for activated sintering of refractory metals[62–65] and ceramics.[63,66] Note that Nb segregation was observed in quenched (but not furnace-cooled) specimens with apparently more disordered GBs (in AC STEM and EDS elemental mapping shown in Figures 6E and 6F, as discussed later), which supports this hypothesized mechanism.

The GB structures in LSTNZS: Experiments vs. atomistic simulations

Apart from the microstructure observations, Figures S23A and S23B display atomic-resolution HAADF-STEM images of LSTNZS (*y* = 9/16) general GB and (010) faceted GBs (with respect to the left-side grain), respectively. The dark bands observed at both GBs can indicate compositional or mean density variation across the GB. Hence, STEM electron energy loss spectroscopy (EELS) measurements were performed to unravel the change of compositions at GBs. However, owing to the lower volume densities of Li^+ ions compared with other types of electrolytes and the poor scattering power of Li (Z = 3),[46,47] the Li-K edges cannot be detected in the STEM-EELS spectrum shown in Figure S24A. More details are discussed in Note S4.

To further investigate the local composition of LSTNZS (*y* = 9/16) GBs beyond experimental limitations, we have fitted an active learning MTP potential to simulate and compare bulk and GB structures of LSTNZS (*y* = 9/16). Our MTP is verified to have excellent accuracy in reproducing DFT energies, forces, stresses, and GB energies (see supplemental experimental procedures). With this MTP, hybrid MC/MD simulations were conducted at the experimental calcination temperature of 1,573 K. The evolution of GB composition is shown in Figure 5B and Table 2. In line with our previous computational results in the LSTZ reference,[53] A-site Sr vacancies and

Table 2. Local composition of the GB regions in the four GB models before and after 5 ns MC/MD simulations at 1,573 K

Elements	Sr	Li	Zr	Ta	Nb	Sn	O
Pristine	9.7%	8.0%	4.6%	6.9%	6.9%	2.3%	61.7%
Simple twist Σ3 [110](110)							
MC/MD 0 ns	9.8%	9.1%	4.2%	7.0%	6.6%	3.2%	60.1%
MC/MD 5 ns	8.5%	10.1%	4.7%	6.3%	6.9%	3.0%	60.4%
Symmetric tilt Σ3 [110]$(1\bar{1}1)$							
MC/MD 0 ns	9.1%	8.8%	4.6%	7.6%	6.9%	2.5%	60.6%
MC/MD 5 ns	7.0%	11.1%	4.8%	6.8%	7.1%	2.0%	61.1%
Simple twist Σ5 [100](100)							
MC/MD 0 ns	9.5%	7.3%	4.4%	7.8%	6.4%	2.7%	61.9%
MC/MD 5 ns	6.8%	11.2%	5.6%	5.4%	7.4%	2.0%	61.5%
Symmetric tilt Σ5 [100]$(0\bar{1}2)$							
MC/MD 0 ns	9.7%	8.1%	4.9%	6.4%	6.2%	2.9%	61.7%
MC/MD 5 ns	8.2%	8.4%	3.0%	9.2%	6.0%	2.5%	62.6%

The atomic percentage of pristine LSTNZS (y = 9/16) was listed for reference.

preserved or increased Li concentration were generally observed at the GB regions of LSTNZS (y = 9/16). The absence of Li depletion at GB regions, which is observed in the resistive GB of the LLTO, promotes Li diffusion at GB regions. In terms of B-site composition, the equilibrated atomic percentage at GB is generally comparable with that of bulk, while slight variations are found to be GB orientation dependent. For instance, the atomic percentage of Ta atoms increased from 6.4% to 9.2%, which is the highest among all other elements at the symmetric tilt Σ5 [100]$(0\bar{1}2)$ GB. On the other hand, Nb atoms become enriched at the simple twist Σ5 [100](100) GB, whereas the atomic percentage of Ta decreases from 7.8% to 5.4%. This result indicates the variations in B-site compositions at GB regions at 1,573 K. Therefore, the elemental segregation observed in STEM-EELS map in Figure S25C can be a phenomenon depending on the GB character (crystallographic anisotropy).

Further conductivity improvements via GB engineering through quenching

Having improved the ionic conductivities of CCPOs to higher than those of the baseline LSTZ, we further demonstrated the performances (conductivity) of CCPOs can be further tuned and improved via employing different cooling rates, which can change (hopefully improve) the total conductivity through changing the GB segregation (compositional profiles) and structure to increase the specific GB conductivity (and potentially also bulk conductivity). This opens a new window to tailor and improve CCPOs and potential other solid electrolytes. Here, we attempted to employ quenching to improve the conductivity of both LSTNZS (unsuccessful) and LSTNZH (successful), which are discussed below.

On the one hand, Figure S26A displays the Nyquist plots of furnace-cooled (brown curve) and air-quenched (orange curve) Sn-containing LSTNZS (y = 9/16). For the air-quenched sample, a second arc attributed to polarization of GBs, secondary phase, and defects has appeared; the calculated bulk, GB, and total ionic conductivity (σ_{bulk}, σ_{gb}, and σ_{total}, respectively, following Note S1) are $\sigma_{bulk} = 2.37 \times 10^{-4}$ S/cm, $\sigma_{gb} = 3.90 \times 10^{-4}$ S/cm, and $\sigma_{total} = 1.47 \times 10^{-4}$ S/cm. When comparing the XRD patterns of the furnace-cooled and air-quenched sample (Figure S26B), the latter shows more pronounced ZrO_2 and SnO_2 peaks as well as appearance of the SrO peaks. SEM-EDS data (Figure S26C) further confirm the increase in the amounts of the secondary phases in the air-quenched LSTNZS (y = 9/16). In summary, quenching generated additional secondary phases and caused the total

Please cite this article in press as: Ko et al., Compositionally complex perovskite oxides: Discovering a new class of solid electrolytes with interface-enabled conductivity improvements, Matter (2023), https://doi.org/10.1016/j.matt.2023.05.035

conductivity σ_{total} to decrease (by ~32.6%) in Sn-containing LSTNZS (despite a slight increase of bulk conductivity), which is undesirable.

On the other hand, similar experiments and characterization were performed on the Hf-containing LSTNZH (x = 9/16) samples to show a beneficial effect of quenching. Figure S26D shows the Nyquist plots of furnace-cooled (gray curve) and air-quenched (red curve) pellets. A smaller arc measured from the latter indicates quenching LSTNZH (x = 9/16) resulted in a desirable increase in the total conductivity σ_{total}. When comparing data of the air-quenched sample with those of furnace cooled, XRD pattern (Figure S26E) and SEM-EDS analysis (Figure S26F) both confirm that quenching LSTNZH (x = 9/16) does not generate additional secondary phases. The results thus suggest that $(Li_{2/3x}Sr_{1-x})(Ta_{2/3x}Nb_{2/3x}Zr_{0.5(1-4/3x)}Hf_{0.5(1-4/3x)})O_{3-\delta}$ has a greater stability threshold than both $(Li_{2/3x}Sr_{1-x})(Ta_{2/3x}Nb_{2/3x}Zr_{0.5(1-4/3x)}Sn_{0.5(1-4/3x)})O_{3-\delta}$ and $(Li_{2/3y}Sr_{1-y})(Ta_{0.334}Nb_{0.347}Zr_{0.211}Sn_{0.108})O_{3-\delta}$. This is likely due to the smaller difference in ionic radii between Hf^{4+} and Zr^{4+} (1.39%) than that between Sn^{4+} and Zr^{4+} (4.17%).

Comparing Sn-containing LSTNZS and Hf-containing LSTNZH, we can conclude that the choice of elements, stoichiometric ratio, differences in ionic radii, and overall valency concurrently influence the phase stability and consequently macroscopic property. It is possible to achieve desirable conductivity improvement via quenching (through the improvement in the specific GB conductivity as we will show next) in Hf-containing LSTNZH where the primary phase is sufficiently stable.

To better understand the influence of cooling rate to the conductivity improvement of the LSTNZH (x = 9/16), larger pellets were synthesized to give greater number of GBs, so that the polarization of the GB component is more pronounced in the AC impedance measurement. Figure 6A shows the Nyquist plots of furnace-cooled (gray curve) and air-quenched (red curve) LSTNZH (x = 9/16). For the air-quenched sample, the calculated bulk, (apparent) GB, and total resistivity (ρ_{bulk}, ρ_{gb}, and ρ_{total}, respectively) are $\rho_{bulk} \approx 2.22 \times 10^3\ \Omega$ cm, $\rho_{gb} \approx 1.69 \times 10^3\ \Omega$ cm, and $\rho_{total} \approx 3.91 \times 10^3\ \Omega$ cm, which are ~21%, ~43%, and ~32% lower than those of the furnace-cooled sample (Figure 6B). The corresponding bulk, (apparent) GB, and total ionic conductivities of the air-quenched LSTNZH (x = 9/16) are $\sigma_{bulk} \approx$ 0.45 mS/cm, $\sigma_{\mathrm{gb}} \approx$ 0.59 mS/cm, and $\sigma_{total} \approx$ 0.256 mS/cm, which represents ~26%, ~77%, and ~48% increase from the furnace-cooled sample (as shown in Figure 1, with data listed in Table S3). Moreover, the specific (true) GB conductivities were calculated to be $\sigma_{gb}^{\mathrm{specific}} \approx 1.36 \times 10^{-6}$ S/cm for the air-quenched LSTNZH vs. $\sigma_{gb}^{\mathrm{specific}} \approx 0.77 \times 10^{-6}$ S/cm for the furnace-cooled LSTNZH (x = 9/16) based on the model approach described in Note S1.

Mechanistic study of the cooling rate effects on GB structure and conductivity

To understand the cause of this decreased GB resistivity (or increased GB conductivity), high-spatial-resolution STEM-EDS measurements were performed at general GBs of furnace-cooled vs. air-quenched LSTNZH samples, and DFT calculations were also performed.

Atomic-resolution HAADF-STEM image of a general GB in the furnace-cooled LSTNZH (x = 9/16) is shown in Figure 6C, from which the EDS spectrum was collected. Figure 6D displays the atomic-resolution elemental maps of Sr, Ta, Nb, Hf, Zr, and O. The maps were generated using intensities from Sr-K, Ta-L, Nb-K, Hf-L, Zr-K, and O-K edges. To analyze the correlation between HAADF image and the elemental maps, plots of vertically integrated intensity profiles across the GB

Please cite this article in press as: Ko et al., Compositionally complex perovskite oxides: Discovering a new class of solid electrolytes with interface-enabled conductivity improvements, Matter (2023), https://doi.org/10.1016/j.matt.2023.05.035

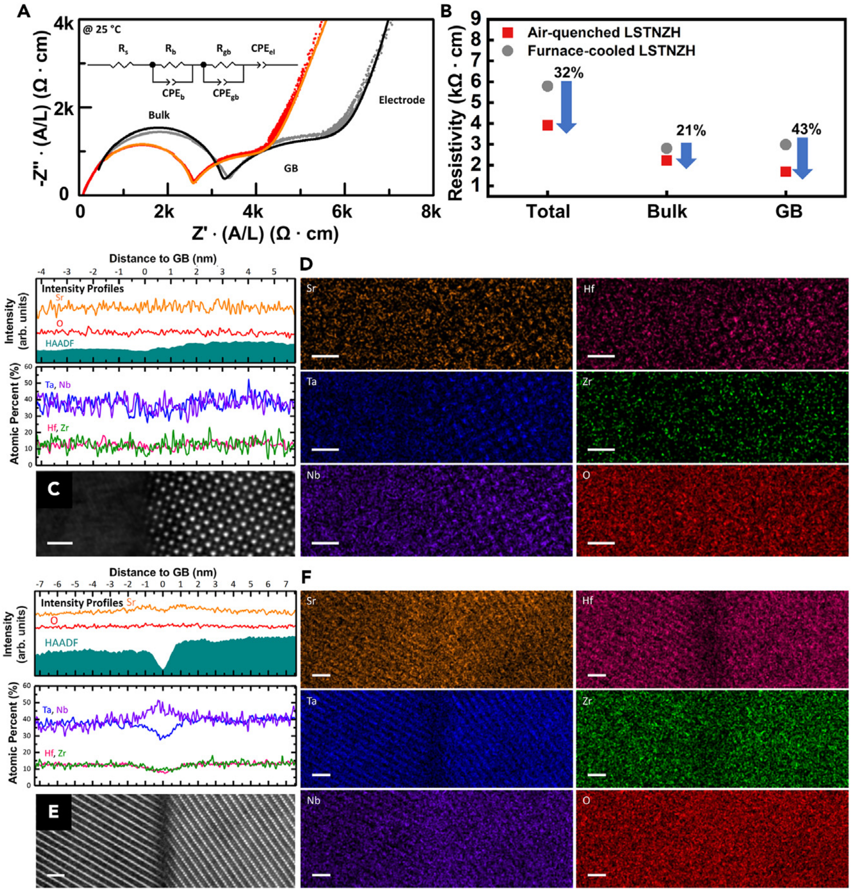

Figure 6. The effects of the cooling rate on structure-property relationship of LSTNZH ($x = 9/16$) samples, including GB structure (segregation) and conductivity

(A) AC impedance spectra of furnace-cooled (gray curve) and air-quenched (red curve) LSTNZH ($x = 9/16$) samples measured at 25°C. Equivalent circuit model used to fit the data is shown in (A).

(B) Bulk, GB, and total resistivity of furnace-cooled and air-quenched LSTNZH ($x = 9/16$) samples.

(C and D) (C) HAADF-STEM image and (D) elemental maps of Sr, Ta, Nb, Hf, Zr, and O collected at the furnace-cooled LSTNZH ($x = 9/16$) general GB.

(E and F) (E) HAADF-STEM image and (F) elemental maps of Sr, Ta, Nb, Hf, Zr, and O collected at the air-quenched LSTNZH ($x = 9/16$) general GB. Scale bars, 1 nm. Additional examples are given in supplemental information to show the statistical significance of the observations.

are shown above the HAADF image (Figure 6C). The intensity profile of the HAADF image increases from left to right because the right grain is in the low-index [100] zone axis, and HAADF intensity of the GB is close to that of the left grain. Consistent with the HAADF image, intensity profiles of Sr, Zr, Hf, and O are mostly uniform, while those of Ta and Nb increase slightly from left to right. Similar results are found at a small-angle GB of furnace-cooled LSTNZH ($x = 9/16$) (Figure S27).

In contrast, significant differences were observed in STEM-EDS of the air-quenched sample. Figure 6E displays the atomic-resolution HAADF-STEM image of an air-quenched LSTNZH ($x = 9/16$) general GB. Similar to the LSTNZS ($y = 9/16$) GBs, an obvious dark band is observed, indicating a compositional variation across the air-quenched LSTNZH ($x = 9/16$) GB. Figure 6F displays the atomic-resolution elemental maps of Sr, Ta, Nb, Hf, Zr, and O generated using the same edges as those used in Figure 6D. To analyze the correlation between HAADF image and

Please cite this article in press as: Ko et al., Compositionally complex perovskite oxides: Discovering a new class of solid electrolytes with interface-enabled conductivity improvements, Matter (2023), https://doi.org/10.1016/j.matt.2023.05.035

the elemental maps, plots of vertically integrated intensity profiles across the GB are again shown above the HAADF image (Figure 6E).

For the Sr profile, a decrease at the GB and an increase at the left and right sides adjacent to the GB was observed. This indicates that the GB has undergone elemental segregation, with Sr segregating out of the GB core and into sides of the abutting grains. This off-center segregation profile, which has been observed in limited other materials such as Co and Ti co-doped WC,[67] represent an interesting feature showing complex interactions of multiple elements (cations) at the GB.

For the B-site elemental signals, Ta, Zr, and Hf decrease while Nb increases at the GB. This indicates Nb is substituting Ta, Zr, and Hf at the GB. Both Sr elemental segregation and Nb substitution suggest greater disorder at the GBs of air-quenched LSTNZH ($x = 9/16$), which can be a factor contributing to their decreased resistivity. To further quantify the B-site stoichiometry at the LSTNZH GBs, Figures S28A, S28B, and S28C plot the total B-site atomic percentage against distance to GB for GBs examined in Figures 6C, S27B, and 6E, respectively. Unlike plots for furnace-cooled LSTNZH (Figures S28A and S28B), the plot for air-quenched LSTNZH (Figure S28C) shows a pronounced decrease in total B-site atomic percentage at the GB. This suggests that quenching resulted in increased B-site vacancies at the GBs, and that Nb does not stoichiometrically fully compensate for the decrease in Ta, Zr, and Hf. Since the O signals do not show a decrease at GBs, the air-quenched LSTNZH GBs likely have higher Li concentration than the nominal value (or net negative charges). Although the Li content cannot be experimentally determined for LSTNZH as well, owing to distinct Li-K edge not observed in low-loss EELS (Figure S29), both excess Li^+ charge carrier at GBs or net negative charges can decrease the GB resistivity.

Moreover, the decrease in HAADF intensity at GB is consistent with the trends observed in elemental signals. Since HAADF-STEM detects inelastically scattered electrons transmitted through the STEM specimen, having less Sr results in less scattering and therefore produces darker A-site atomic columns at the GB core than at the sides of the abutting grains. Similarly, having B-site vacancies at GBs results in darker B-site atomic columns. Furthermore, atomic columns with higher average atomic number appear brighter in HAADF-STEM images, so lighter Nb ($Z = 41$) substituting heavier Hf ($Z = 72$) and Ta ($Z = 73$) results in darker B-site atomic columns at GB. It is also possible the general GBs in quenched specimens are more structurally disordered (quenching the high-temperature interfacial disordering that has been widely observed[68–70] and can be enhanced by compositional complexity[71]). Thus, the likely effects of quenching are as follows. It causes compositions of both GBs and the nearby bulk regions to deviate from the nominal stoichiometry $(Li_{0.375}Sr_{0.4375})(Ta_{0.375}Nb_{0.375}Zr_{0.125}Hf_{0.125})O_{3-\delta}$. This change in composition likely results in increased B-site vacancies and potentially greater chemical (and structural) disorder at the GBs, all of which can facilitate Li^+ ion migration to decrease GB resistivity.

It should be noted that multiple GBs were characterized for both air-quenched and furnace-cooled specimens to ensure the observed differences are general and statistically significant. Additional examples are documented in supplemental information. Further STEM-EDS measurements were performed at one GB formed by grains that have average grain size (Figure S30) and at two GBs by grains that have above-average grain sizes (Figure S31). The results are similar to those found in the general GB shown in Figure 6E. From these observations, it is reasonable to

Please cite this article in press as: Ko et al., Compositionally complex perovskite oxides: Discovering a new class of solid electrolytes with interface-enabled conductivity improvements, Matter (2023), https://doi.org/10.1016/j.matt.2023.05.035

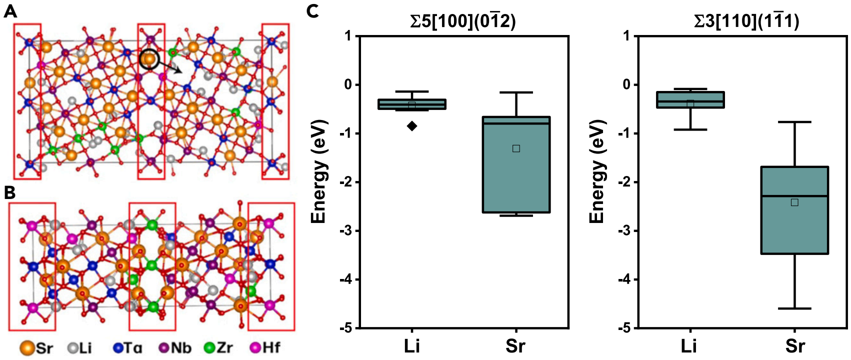

Figure 7. GB models and the corresponding DFT calculations for the stabilization energy investigation

(A and B) The lowest-energy relaxed (A) Σ5 [100](0 $\bar{1}$ 2) and (B) Σ3 [110](1$\bar{1}$ 1) structures of LSTNZH, respectively. The red rectangles indicate the GB regions in the model systems. In (A), the black circle and arrow indicate an Sr locating at GB to be placed at a nearby vacancy away from the GB center for calculating the stabilization energy (the driving force of elemental depletion).

(C) The result of stabilization energy calculations in boxplots. The squares indicate the mean values, and the black diamond represents an outlier.

infer that Sr segregation and Nb substitution are present in all general GBs of air-quenched LSTNZH, regardless of the sizes of grains forming the boundaries. Following the same analysis performed earlier, Figures S28D, S28E, and S28F plot the total B-site atomic percentage against distance to GB for the GBs examined in Figures S30C, S31C, and S31E, respectively. Both Figures S28D and S28F display a pronounced decrease in total B-site atomic percentage at the GBs, further providing confidence to the conclusion that air quenching promotes B-site vacancies at GBs. As for Figure S28E, the decrease is not observed due to a thickness gradient in this selected region, thinner on left and thicker on right of GB, which might be excluded as an artifact of single incident.

It is worth noting that, despite the compositional change, the cubic perovskite crystal structure is still maintained at the GBs of the air-quenched sample, albeit the general GBs can be more disordered as discussed above, as (premelting-like) high-temperature GB disordering induced by the temperature and enhanced by segregation may be partially quenched.[68–70] HAADF-STEM images (Figures 6E, S30C, S31C, and S31E) clearly show the same crystal lattices from the bulk extend all the way to the GBs, with the observed decrease in intensity at GBs. Thus, GBs of air-quenched LSTNZH likely consist of defective perovskite structures with increased number of B-site vacancies and possible (relatively low levels of) GB structural disordering.

Furthermore, first-principles DFT calculations were conducted to investigate the A-site elemental contents at LSTNZH (x = 9/16) GBs. Twenty randomly ordered LSTNZH systems that satisfied nominal stoichiometry at both bulk and GB regions were generated for Σ5 [100](0 $\bar{1}$ 2) and Σ3 [110](1$\bar{1}$ 1) GBs (see Figures 7A and 7B for the lowest-energy relaxed structures). After relaxation, the changes of A-site elemental fractions have been observed in the lowest-energy structure of Σ5 [100](0 $\bar{1}$ 2) GB (the change of fraction from 7/16 to 3/16 for Sr, and from 6/16 to 5/16 for Li), demonstrating a higher tendency for Sr ions to leave the GB regions. For each type of GB, three lowest-lying relaxed structures, which represent various local ordering of A-site and B-site elements, were selected for further stabilization

Please cite this article in press as: Ko et al., Compositionally complex perovskite oxides: Discovering a new class of solid electrolytes with interface-enabled conductivity improvements, Matter (2023), https://doi.org/10.1016/j.matt.2023.05.035

energy calculations. The stabilization energy is defined as the total energy of the system with a target A-site ion placed at nearby A-site vacancy away from GB center minus the total energy of the original system with the ion located at the GB region (see Figure 7A for an example), which estimates the driving force for the depletion of the ion. As shown in Figure 7C, Sr ions in general possess lower stabilization energies, suggesting a larger driving force to depart from GB regions than Li ions for the LSTNZH system. The result is in line with the MTP MC/MD simulations for the comparable system LSTNZS, where Sr depletion and maintaining Li concentration at GBs have been found. The trend can be attributed to the distinct coordination environments and the shorter A-site-to-A-site distance at the GB regions, which have a larger effect on the Sr ion due to its larger ionic radius and valency charge. It appears to be consistent with the off-center GB segregation of Sr, with relative Sr depletion at the GB core, revealed by STEM-EDS (Figure 6E), although it does not explain the off-center segregation directly, which can be a complex interplay (including possible GB disordering effects) at more general GBs (than the simplified special Σ GBs that can be modeled by DFT). Importantly, the calculations suggest less tendency for Li depletion at the GBs for LSTNZH, so that it is less of a concern to reduce the specific GB conductivity of this class of materials (consistent with the MTP MC/MD results of LSTNZS shown above).

Electrochemical stability

To characterize the electrochemical stability window of our CCPOs, cyclic voltammetry (CV) scanned at 0.1 mV/s was performed using half-cell configuration. Figure 8A presents an overlay of the cyclic voltammograms to compare the reduction limits of LSTNZS ($y = 9/16$), LSTNZH ($x = 9/16$), and LSTZ. The onset reduction potential, the voltage at which a large amount of reduction reaction begins to take place, is defined as the intersection point of the dashed line extrapolated from the low-current-response region and that extrapolated from the large negative-current-response region. The onset reduction potential is 1.4 V for both CCPOs and LSTZ (inset in Figure 8A). On the one hand, LSTNZS displays an additional oxidation peak at 0.5 V, corresponding to Sn/Li dealloying reaction.[72] On the other hand, LSTNZH exhibits reduction and oxidation onset potentials comparable with those of LSTZ despite its compositional complexity. According to the grand potential diagram in Figure S1, the calculated electrochemical stability window of LSTNZH is 1.63–3.58 V and that of LSTZ is 1.13–3.56 V. The small discrepancies between simulated and experimental results may be due to sluggish kinetics of decomposition reactions and passivation by decomposition interphase, which was not accounted for in the theoretical calculations.[73]

To validate the cyclability of CCPOs, the liquid-solid hybrid Li | LSTNZS | Li symmetrical cell was assembled and tested at 300 μA cm^{-2}. The result in Figure 8B shows that the cell was cycled for 120 h with a stable overpotential of 200 mV for Li stripping/plating reactions before polarization increased. Since LSTNZH is more electrochemically stable than LSTNZS, CV of LSTNZH coated on Al foil was measured to further test its stability at high voltage. Cyclic voltammogram shows stable cycling from 1.75 to 4.0 V when the electrode was evaluated from 0.8 to 4.3 V (Figure 8C). Given this electrochemical stability window, one possible ASSB would be $LiFePO_4$ || LSTNZH || prelithiated V_2O_5. The voltage profiles in Figure S32 show the galvanostatic charge and discharge curves of prelithiated V_2O_5 and $LiFePO_4$ half-cells, demonstrating their working windows fall within 1.75–4.0 V. Since the ASSB full cell assembly requires extensive optimization in fabrication process, it is out of the scope of this study and will be pursued as future work.

Please cite this article in press as: Ko et al., Compositionally complex perovskite oxides: Discovering a new class of solid electrolytes with interface-enabled conductivity improvements, Matter (2023), https://doi.org/10.1016/j.matt.2023.05.035

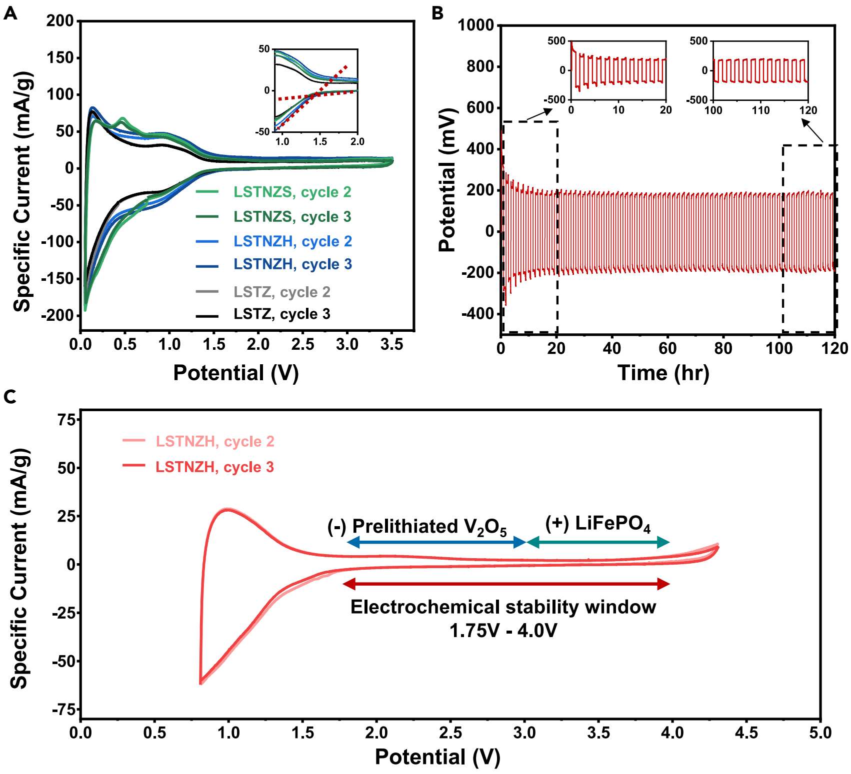

Figure 8. The electrochemical stability testing by cyclic voltammogram using half-cells for LSTNZS, LSTNZH, or LSTZ

(A) The comparison of CV curves among three sample groups, as indicated: LSTNZS (green), LSTNZH (blue), and LSTZ (gray). The half-cells were assembled using Li metal (anode), LP40 with 10 vol % FEC (liquid electrolyte), and testing sample coated on Cu foil (cathode). The CV measurements were scanned within the potential window of 0–3.5 V, with a scan rate of 0.1 mV/s. The enlarged region shows the onset reduction potential at 1.4 V.

(B) The Li-Li symmetrical cell testing using LSTNZS as the solid electrolyte separator with trace LP40 liquid electrolyte and 3501 Celgard separators on both sides between LSTNZS and Li metal. The cell was tested at 300 $\mu A\ cm^{-2}$ for 120 h, with an overpotential of 200 mV.

(C) Cyclic voltammogram of half-cell assembled using Li metal (anode), LP40 with 10 vol % FEC (liquid electrolyte), and LSTNZH coated on Al foil (cathode). The CV curves were scanned from 0.8 to 4.3 V at a scan rate of 0.1 mV/s.

Conclusions

In summary, we have discovered a class of CCPOs as solid electrolytes with improved properties via new compositionally complex materials discovery strategies, followed by a systematic investigation on the influence of mobile carriers (Li^+), vacancy sites (V_A''), and B-site aliovalent substitution (Sn^{4+}, Nb^{5+}) on phase stability, grain size, and ionic conductivity. We have further discovered the composition-phase-property relationship to suggest a suitable cation stoichiometry range for maintaining single phase upon maximizing A-site carrier concentration. Using a fitted active learning MTP, MC/MD simulations revealed increased Sr vacancies and equal or greater Li^+ concentration at the GB regions of LSTNZS (compared with bulk) that explained the reduced GB resistance. Moreover, a statistical analysis of the microstructures uncovered increased grain sizes of CCPOs, which reduced the amounts of GBs to improve total ionic conductivity. To unravel the origin of enhanced grain growth in CCPOs, a controlled experiment suggested that Nb^{5+} substitution in B site promotes grain growth, thereby reducing the total (apparent) GB resistance. It is hypothesized the Nb segregation at GBs (observed in quenched

Please cite this article in press as: Ko et al., Compositionally complex perovskite oxides: Discovering a new class of solid electrolytes with interface-enabled conductivity improvements, Matter (2023), https://doi.org/10.1016/j.matt.2023.05.035

specimens) induces interfacial disordering at high temperatures, thereby promoting grain growth. An additional interesting and useful finding was that quenching can be adopted to enhance the GB, and therefore the total, ionic conductivity of LSTNZH, thereby providing a new knob to tailor and improve the properties. Aberration-corrected STEM-EDS attributed the 77% increase in specific (true) GB ionic conductivity to compositional and structural changes in the GBs of air-quenched LSTNZH. For A-site elements at LSTNZH GBs, DFT calculations revealed that the Sr ions have a higher tendency to leave the GB regions than Li ions. Along with MTP MC/MD results of LSTNZS, the calculations suggest that GB Li depletion is less of a problem for these CCPOs to reduce specific GB ionic conductivity. Finally, cyclic voltammogram of LSTNZH showed stable cycling from 1.75 to 4.0 V, with comparable electrochemical stability with the state-of-the-art LSTZ baseline but achieving $\sim 2.7\times$ increase in the total ionic conductivity.

In a broader perspective, this study has established new strategies to tailor CCCs via a combination of non-equimolar complex compositional designs and microstructure and interface engineering via controlled materials processing. Using solid electrolytes as an exemplar, we have validated these new strategies in this study via discovering a new class of CCPOs to show the possibility of improving ionic conductivities beyond the limit of conventional doping, where controls of the microstructures and interfaces are important beyond the complex compositional designs. This work opens a new window for discovering compositionally complex ceramics or CCCs for energy storage and many other applications.

EXPERIMENTAL PROCEDURES

Resource availability

Lead contact

Further information and requests for resources and materials should be directed to and will be fulfilled by the lead contact, Jian Luo (jluo@alum.mit.edu).

Materials availability

All the materials generated in this study are available from the lead contact, Jian Luo (jluo@alum.mit.edu), upon request.

Data and code availability

The data supporting the conclusions and findings are provided in the article and supplemental information. Additional data are available from the lead contact, Jian Luo (jluo@alum.mit.edu), upon request.

Materials synthesis

All specimens were synthesized using solid-state reactions. The precursor Li_2CO_3 (Acros Organics, 99.999%), $SrCO_3$ (Alfa Aesar, 99.99%), Ta_2O_5 (Inframat Advanced Materials, 99.85%), Nb_2O_5 (Alfa Aesar, 99.9%), ZrO_2 (US Research Nanomaterials, 99.9%), and SnO_2 (US Research Nanomaterials, 99.9%) powders were used for LSTNZS series, and HfO_2 (Alfa Aesar, 325 mesh) was also used for LSTNZH series instead. The 10 wt % excess Li_2CO_3 precursor was added for LSTNZS to compensate Li_2O loss during high-temperature sintering (Figure S33). All weighted precursors were ball milled using SPEX 8000D high-energy ball mill for a continuous 100 min. Subsequently, the powder mixture was calcinated at 800°C for 2 h in air to remove carbonates and was pressed into green pellets 10 mm in diameter by a hydraulic press. The specimens were sintered at 1,300°C for 12 h in air. The air-quenched sample was taken out from the high-temperature furnace at 1,300°C after 12 h of sintering and placed in air to quench to room temperature (>40°C/min cooling rate). All

Please cite this article in press as: Ko et al., Compositionally complex perovskite oxides: Discovering a new class of solid electrolytes with interface-enabled conductivity improvements, Matter (2023), https://doi.org/10.1016/j.matt.2023.05.035

as-sintered pellets were ground and polished on both sides before material characterizations.

Conductivity measurements

The pellet samples were prepared using the procedures described in the materials synthesis section. Ionic conductivity was evaluated at 25°C and frequencies from 100 Hz to 40 MHz with an applied voltage amplitude of 0.1 V, using a Hewlett-Packard 4194A Impedance Analyzer. To validate the negligible electronic conductivity contribution in the impedance measurement, DC polarization was measured at constant voltage of 0.1 V for 8 h and measured from 0.5 to 5.5 V with a 1.0 V interval for 12 h at each step, using a Solartron potentiostat. In Figure S34, the ionic transference number of LSTNZH (x = 9/16) was calculated (t_i = 0.998 at 0.1 V), and the resistance was fitted as the slope of potential-electronic current line (91.81 ± 7.27 MΩ). Before the ionic and electrical conductivity measurements, both planar surfaces of the sintered pellet were polished and subsequently coated with lithium-ion-blocking Ag electrodes. Ag electrodes were coated using the Denton Discovery 635 sputter system.

The temperature dependence of ionic conductivity for LSTNZS (y = 9/16) was measured in the temperature range from 25°C to 150°C. The activation energy (E_a) was calculated from the slope of $\ln(\sigma T)$ vs. $1/T$ plot using the rearranged Arrhenius equation[74]:

$$ln(\sigma T) = -\frac{E_a}{K_B T} + ln(\sigma_0) \qquad \text{(Equation 2)}$$

where E_a is the activation energy, k_B is the Boltzmann's constant (1.380649×10^{-23} J/K), T is temperature, and σ_0 is a constant. Thus, E_a of ionic conductivity can be calculated from the slope fitted from $\ln(\sigma T)$ vs. $1/T$ curve.

Crystallography and microstructure characterization

The crystal structure was characterized by XRD with Rigaku MiniFlex (Cu Kα radiation, λ = 1.5406 Å, scan rate = 2.3°/min, step = 0.01°). SEM (FEI Apreo) with EDS (Oxford N-MAX) was performed to probe the elemental homogeneity using applied current 3.2 nA and voltage 20 kV. The relative densities of sintered pellets were calculated by the ratio of the experimental density (measured by weight and volume) and the theoretical density from XRD refinements. EBSD was conducted at 26 nA and 20 kV, using FEI Apreo LoVac SEM with Oxford Instruments Symmetry EBSD detector. The grain size and coincidence-site lattice grain-boundary (GB) analysis were performed using the inverse pole figures along the sample normal direction. The grain size and coincidence-site lattice (CSL) GB analyses were performed using Tango software.

Electron microscopy

Transmission electron microscopy (TEM) specimen preparation procedures are described in the supplemental information (see supplemental experimental procedures) with a sensitivity test on mechanical polishing medium (Figure S35). HAADF-STEM imaging, core-loss EELS, and EDS measurements were conducted using a JEOL JEM 300CF operated at 300 kV. The microscope was equipped with double aberration correctors, Gatan Image Filter Quantum with Gatan K2 Summit, and dual 100-mm^2 Si drift detectors (SDDs). Z-contrast HAADF-STEM imaging was performed with a probe convergence semiangle of 25.7 mrad and a large inner collection angle of 70 mrad. For core-loss EELS measurements, a dispersion of 0.5 eV per channel was used to collect the edges in the ultra-high-energy-loss regime (Sr-$L_{2,3}$,

Please cite this article in press as: Ko et al., Compositionally complex perovskite oxides: Discovering a new class of solid electrolytes with interface-enabled conductivity improvements, Matter (2023), https://doi.org/10.1016/j.matt.2023.05.035

Ta-$M_{2,3}$, Ta-$M_{4,5}$, Nb-$L_{2,3}$, and Zr-$L_{2,3}$ edges), while 0.1 eV per channel was used to collect the O-K edge. These EELS spectra were obtained using the Gatan K2 Summit direct detection camera. The use of a direct electron detector allows for a low electron dose and minimizes irradiation damage. Edges in the low loss regime (Sr-N_1 and Ta-$O_{2,3}$) were obtained using the US1000 detector, with a dispersion of 0.1 eV per channel. All core-loss EELS spectra were collected using a 2.5-mm aperture and a spectrometer collection angle of 35.89 mrad. For EDS measurements, spectra were acquired using the dual 100-mm^2 SDDs. Seventy-five scans (each with a 0.15-ms dwell time and 0.4 Å pixel size) in the same area at the GBs were summed.

Electrochemistry

The as-sintered pellet samples were ground into powders through high-energy ball milling. The as-ground powders were mixed with carbon black and PVDF binder at a ratio of 50:30:20 by weight in NMP solvent using Thinky mixer. The slurry was cast on the current collector foil (Cu/Al) with a film thickness control of 20 μm and dried at 80°*C* under vacuum for 12 h. The electrodes were punched into 10-mm diameter discs and assembled into 2032-type coin cells in glovebox with Li metal as counter electrodes, LP40 (1 M $LiPF_6$ in 1:1 EC/DEC) with 10 vol % fluoroethylene carbonate (FEC) as liquid electrolyte, and Celgard 3501 as separator. CV measurements were implemented at 0.1 mV/s step, sweeping between vortex potentials for three cycles. Figure S36 shows SEI formation from the decomposition of EC and DEC in the first cycle, but no further influence from LP40 liquid electrolyte was observed in second and third cycles.

The Li-Li symmetrical cells were assembled in a glovebox using Swagelok-type cell with 0.7-mm-thick LSTNZS pellet as the solid electrolyte layer. For wetting purposes at the interface of Li and LSTNZS pellet, 50 μL of LP40 liquid electrolyte with 10 vol % FEC additive and 3501 Celgard separators were applied on both sides between LSTNZS and Li metal. The cell was cycled at a constant discharge and charge current density of 300 $\mu A\ cm^{-2}$ using Landt CT2001A battery tester. The $LiFePO_4$ | Li and prelithiated V_2O_5 | Li half-cells were prepared using the same procedure described for half-cell assembly. The galvanostatic cycling test was done to obtain discharge profile of prelithiated V_2O_5 | Li at 1.8–3.0 V and the charge profile of $LiFePO_4$ | Li at 3.0–4.1 V.

Simulations

For both accurate and efficient simulations, we adopted a slightly modified chemical formula to represent LSTNZS ($y = 9/16$), i.e., $Li_{7/18}Sr_{17/36}Ta_{1/3}Nb_{1/3}Zr_{2/9}Sn_{1/9}O_3$ with the experimentally optimized cation ratios. We utilized the active learning workflow in our study on pristine LSTZ with slight modification to fit an active learning MTP for LSTNZS. The workflow is shown in Figure S37 and described in detail in the supplemental information (see supplemental experimental procedures). The DFT and *ab initio* molecular dynamics (AIMD) simulation procedures are also described in supplemental information (Figures S38–S40). The convergence criteria are the same as our work in LSTZ. The active learning scheme proposed by Podryabinkin and Shapeev was used to develop an MTP that can accurately simulate both bulk and GB structures.[75,76] An extrapolation grade γ is defined to evaluate the extent to which a given configuration is extrapolative with respect to those in the training set, thereby correlating the prediction error without *ab initio* information. All training, active learning, evaluations, and simulations with MTP were performed using MLIP,[77,78] LAMMPS,[79] and the Materials Machine Learning (maml) Python package. The visualization of bulk and GB models were conducted using OVITO. The analysis on MD trajectories to extract diffusivities were performed with the pymatgen-analysis-diffusion package.

SUPPLEMENTAL INFORMATION

Supplemental information can be found online at https://doi.org/10.1016/j.matt.2023.05.035.

ACKNOWLEDGMENTS

This research was supported by the National Science Foundation Materials Research Science and Engineering Center program through the UC Irvine Center for Complex and Active Materials (DMR-2011967). The TEM experiments were conducted using the facilities at the Irvine Materials Research Institute (IMRI) in the University of California, Irvine. The XRD, SEM, and EBSD experiments were performed at UC San Diego Nanoengineering Materials Research Center (NE-MRC). The computing resources were provided by the National Energy Research Scientific Computing Center (NERSC), a US Department of Energy Office of Science User Facility at Lawrence Berkeley National Laboratory and the Extreme Science and Engineering Discovery Environment (XSEDE), which is supported by National Science Foundation grant number ACI-1548562.

AUTHOR CONTRIBUTIONS

J.L. conceived the idea and formulated the overall research plan. J.L., X.P., and S.P.O. supervised different aspects of the project. S.T.K., T.L., and J.Q. designed the specific studies. S.T.K. developed the composition optimization strategy and the systematic composition investigation with the help of D.Z. S.T.K. synthesized CCPO materials and implemented XRD, SEM-EDS, EBSD characterization, and electrical measurements with data analysis. S.T.K. and W.C.T. conducted electrochemical measurements. T.L., S.S., and Z.W. carried out AC impedance measurements and TEM specimen preparation. T.L. and X.W. performed STEM experiments and data analysis. W.J.B. supervised X.W. on STEM characterization. J.Q. conducted MTP fitting, MC/MD simulations, and grand potential phase diagram calculations. J.Q. and W.T.P. constructed GB models and performed DFT calculations. S.T.K., T.L., J.Q., D.Z., and W.T.P. wrote the initial manuscript draft, and J.L. revised and finalized the manuscript. All authors contributed to the discussion and revision of the manuscript.

DECLARATION OF INTERESTS

The authors declare no competing interests.

Received: December 27, 2022
Revised: April 21, 2023
Accepted: May 19, 2023
Published: June 21, 2023

REFERENCES

1. Wright, A.J., and Luo, J. (2020). A step forward from high-entropy ceramics to compositionally complex ceramics: a new perspective. J. Mater. Sci. *55*, 9812–9827. https://doi.org/10.1007/s10853-020-04583-w.
2. Oses, C., Toher, C., and Curtarolo, S. (2020). High-entropy ceramics. Nat. Rev. Mater. *5*, 295–309. https://doi.org/10.1038/s41578-019-0170-8.
3. Rost, C.M., Sachet, E., Borman, T., Moballegh, A., Dickey, E.C., Hou, D., Jones, J.L., Curtarolo, S., and Maria, J.-P. (2015). Entropy-stabilized oxides. Nat. Commun. *6*, 8485. https://doi.org/10.1038/ncomms9485.
4. Gild, J., Zhang, Y., Harrington, T., Jiang, S., Hu, T., Quinn, M.C., Mellor, W.M., Zhou, N., Vecchio, K., and Luo, J. (2016). High-entropy metal diborides: a new class of high-entropy materials and a new type of ultrahigh temperature ceramics. Sci. Rep. *6*, 37946. https://doi.org/10.1038/srep37946.
5. Jiang, S., Hu, T., Gild, J., Zhou, N., Nie, J., Qin, M., Harrington, T., Vecchio, K., and Luo, J. (2018). A new class of high-entropy perovskite oxides. Scripta Mater. *142*, 116–120. https://doi.org/10.1016/j.scriptamat.2017.08.040.
6. Gild, J., Samiee, M., Braun, J.L., Harrington, T., Vega, H., Hopkins, P.E., Vecchio, K., and Luo, J. (2018). High-entropy fluorite oxides. J. Eur. Ceram. Soc. *38*, 3578–3584. https://doi.org/10.1016/j.jeurceramsoc.2018.04.010.
7. Gild, J., Braun, J., Kaufmann, K., Marin, E., Harrington, T., Hopkins, P., Vecchio, K., and Luo, J. (2019). A high-entropy silicide: $(Mo_{0.2}Nb_{0.2}Ta_{0.2}Ti_{0.2}W_{0.2})Si_2$. J. Mater. *5*,

Please cite this article in press as: Ko et al., Compositionally complex perovskite oxides: Discovering a new class of solid electrolytes with interface-enabled conductivity improvements, Matter (2023), https://doi.org/10.1016/j.matt.2023.05.035

337–343. https://doi.org/10.1016/j.jmat.2019.03.002.

8. Qin, M., Vega, H., Zhang, D., Adapa, S., Wright, A.J., Chen, R., and Luo, J. (2022). 21-Component compositionally complex ceramics: discovery of ultrahigh-entropy weberite and fergusonite phases and a pyrochlore-weberite transition. J. Adv. Ceram. *11*, 641–655. https://doi.org/10.1007/s40145-022-0575-5.

9. Nguyen, T.X., Liao, Y., Lin, C., Su, Y., and Ting, J. (2021). Advanced high entropy perovskite oxide electrocatalyst for oxygen evolution reaction. Adv. Funct. Mater. *31*, 2101632. https://doi.org/10.1002/adfm.202101632.

10. Zhou, S., Pu, Y., Zhang, X., Shi, Y., Gao, Z., Feng, Y., Shen, G., Wang, X., and Wang, D. (2022). High energy density, temperature stable lead-free ceramics by introducing high entropy perovskite oxide. Chem. Eng. J. *427*, 131684. https://doi.org/10.1016/J.CEJ.2021.131684.

11. Pu, Y., Zhang, Q., Li, R., Chen, M., Du, X., and Zhou, S. (2019). Dielectric properties and electrocaloric effect of high-entropy $(Na_{0.2}Bi_{0.2}Ba_{0.2}Sr_{0.2}Ca_{0.2})TiO_3$ ceramic. Appl. Phys. Lett. *115*, 223901. https://doi.org/10.1063/1.5126652.

12. Li, X., Ma, J., Chen, K., Li, C., Zhang, X., and An, L. (2022). Design and investigate the electrical properties of $Pb(Mg_{0.2}Zn_{0.2}Nb_{0.2}Ta_{0.2}W_{0.2})O_3$–$PbTiO_3$ high-entropy ferroelectric ceramics. Ceram. Int. *48*, 12848–12855. https://doi.org/10.1016/j.ceramint.2022.01.156.

13. Witte, R., Sarkar, A., Kruk, R., Eggert, B., Brand, R.A., Wende, H., and Hahn, H. (2019). High-entropy oxides: an emerging prospect for magnetic rare-earth transition metal perovskites. Phys. Rev. Mater. *3*, 034406. https://doi.org/10.1103/PhysRevMaterials.3.034406.

14. Zheng, Y., Yang, Y., Wang, M., Hu, S., Wu, J., Yu, Z., and Lin, Y.-H. (2021). Electrical and thermal transport behaviours of high-entropy perovskite thermoelectric oxides. BMC Plant Biol. *21*, 377–384. https://doi.org/10.1007/s40145-021-0462-5.

15. Yin, Y., Shi, F., Liu, G.-Q., Tan, X., Jiang, J., Tiwari, A., and Li, B. (2022). Spin-glass behavior and magnetocaloric properties of high-entropy perovskite oxides. Appl. Phys. Lett. *120*, 082404. https://doi.org/10.1063/5.0081688.

16. Sharma, Y., Musico, B.L., Gao, X., Hua, C., May, A.F., Herklotz, A., Rastogi, A., Mandrus, D., Yan, J., Lee, H.N., et al. (2018). Single-crystal high entropy perovskite oxide epitaxial films. Phys. Rev. Mater. *2*, 060404. https://doi.org/10.1103/PhysRevMaterials.2.060404.

17. Li, Z., Guan, B., Xia, F., Nie, J., Li, W., Ma, L., Li, W., Zhou, L., Wang, Y., Tian, H., et al. (2022). High-entropy perovskite as a high-performing chromium-tolerant cathode for solid oxide fuel cells. ACS Appl. Mater. Interfaces *14*, 24363–24373. https://doi.org/10.1021/acsami.2c03657.

18. Zhang, D., De Santiago, H.A., Xu, B., Liu, C., Trindell, J.A., Li, W., Park, J., Rodriguez, M.A., Coker, E.N., Sugar, J.D., et al. (2023). Compositionally complex perovskite oxides for solar thermochemical water splitting. Chem. Mater. *35*, 1901–1915. https://doi.org/10.1021/acs.chemmater.2c03054.

19. Yan, J., Wang, D., Zhang, X., Li, J., Du, Q., Liu, X., Zhang, J., and Qi, X. (2020). A high-entropy perovskite titanate lithium-ion battery anode. J. Mater. Sci. *55*, 6942–6951. https://doi.org/10.1007/s10853-020-04482-0.

20. Guo, M., Liu, Y., Zhang, F., Cheng, F., Cheng, C., Miao, Y., Gao, F., and Yu, J. (2022). Inactive Al^{3+}-doped $La(CoCrFeMnNiAl_x)_{1/(5+x)}O_3$ high-entropy perovskite oxides as high performance supercapacitor electrodes. J. Adv. Ceram. *11*, 742–753. https://doi.org/10.1007/s40145-022-0568-4.

21. Wright, A.J., Wang, Q., Huang, C., Nieto, A., Chen, R., and Luo, J. (2020). From high-entropy ceramics to compositionally-complex ceramics: a case study of fluorite oxides. J. Eur. Ceram. Soc. *40*, 2120–2129. https://doi.org/10.1016/j.jeurceramsoc.2020.01.015.

22. Manthiram, A., Yu, X., and Wang, S. (2017). Lithium battery chemistries enabled by solid-state electrolytes. Nat. Rev. Mater. *2*, 16103. https://doi.org/10.1038/natrevmats.2016.103.

23. Wu, J., Chen, L., Song, T., Zou, Z., Gao, J., Zhang, W., and Shi, S. (2017). A review on structural characteristics, lithium ion diffusion behavior and temperature dependence of conductivity in perovskite-type solid electrolyte $Li_{3x}La_{2/3-x}TiO_3$. Funct. Mater. Lett. *10*, 1730002. https://doi.org/10.1142/S179360471730002X.

24. Nakayama, M., Usui, T., Uchimoto, Y., Wakihara, M., and Yamamoto, M. (2005). Changes in electronic structure upon lithium insertion into the A-site deficient perovskite type oxides $(Li,La)TiO_3$. J. Phys. Chem. B *109*, 4135–4143. https://doi.org/10.1021/jp046062j.

25. Chen, C. (2001). Ionic conductivity, lithium insertion and extraction of lanthanum lithium titanate. Solid State Ionics *144*, 51–57. https://doi.org/10.1016/S0167-2738(01)00884-0.

26. Wang, M.J., Wolfenstine, J.B., and Sakamoto, J. (2020). Mixed electronic and ionic conduction properties of lithium lanthanum titanate. Adv. Funct. Mater. *30*, 1909140. https://doi.org/10.1002/adfm.201909140.

27. Chen, C. (2004). Stable lithium-ion conducting perovskite lithium–strontium–tantalum–zirconium–oxide system. Solid State Ionics *167*, 263–272. https://doi.org/10.1016/j.ssi.2004.01.008.

28. Bernuy-Lopez, C., Manalastas, W., Lopez del Amo, J.M., Aguadero, A., Aguesse, F., and Kilner, J.A. (2014). Atmosphere controlled processing of Ga-substituted garnets for high Li-ion conductivity ceramics. Chem. Mater. *26*, 3610–3617. https://doi.org/10.1021/cm5008069.

29. Kamaya, N., Homma, K., Yamakawa, Y., Hirayama, M., Kanno, R., Yonemura, M., Kamiyama, T., Kato, Y., Hama, S., Kawamoto, K., and Mitsui, A. (2011). A lithium superionic conductor. Nat. Mater. *10*, 682–686. https://doi.org/10.1038/nmat3066.

30. Yao, R., Liu, Z.-G., Ding, Z.-Y., Jin, Y.-J., Cao, G., Wang, Y.-H., and Ouyang, J.-H. (2020). Effect of Sn or Ta doping on the microstructure and total conductivity of perovskite $Li_{0.24}La_{0.587}TiO_3$ solid electrolyte. J. Alloys Compd. *844*, 156023. https://doi.org/10.1016/j.jallcom.2020.156023.

31. Teranishi, T., Yamamoto, M., Hayashi, H., and Kishimoto, A. (2013). Lithium ion conductivity of Nd-doped (Li, La)TiO_3 ceramics. Solid State Ionics *243*, 18–21. https://doi.org/10.1016/j.ssi.2013.04.014.

32. Morata-Orrantia, A., García-Martín, S., and Alario-Franco, M.Á. (2003). Optimization of lithium conductivity in La/Li titanates. Chem. Mater. *15*, 3991–3995. https://doi.org/10.1021/cm0300563.

33. Chung, H., Kim, J.-G., and Kim, H.-G. (1998). Dependence of the lithium ionic conductivity on the B-site ion substitution in $(Li_{0.5}La_{0.5})Ti_{1-x}M_xO_3$ (M=Sn, Zr, Mn, Ge). Solid State Ionics *107*, 153–160. https://doi.org/10.1016/S0167-2738(97)00525-0.

34. Okumura, T., Ina, T., Orikasa, Y., Arai, H., Uchimoto, Y., and Ogumi, Z. (2011). Improvement of lithium ion conductivity for A-site disordered lithium lanthanum titanate perovskite oxides by fluoride ion substitution. J. Mater. Chem. *21*, 10061. https://doi.org/10.1039/c0jm04367b.

35. Lee, S.J., Bae, J.J., and Son, J.T. (2019). Structural and electrical effects of Y-doped $Li_{0.33}La_{0.56-x}Y_xTiO_3$ solid electrolytes on all-solid-state lithium ion batteries. J. Kor. Phys. Soc. *74*, 73–77. https://doi.org/10.3938/jkps.74.73.

36. Goldschmidt, V.M. (1926). Die gesetze der Krystallochemie. Naturwissenschaften *14*, 477–485. https://doi.org/10.1007/BF01507527.

37. Yazhou, K., and Zhiren, Y. (2022). Synthesis, structure and electrochemical properties of Al doped high entropy perovskite $Li_x(LiLaCaSrBa)Ti_{1-x}Al_xO_3$. Ceram. Int. *48*, 5035–5039. https://doi.org/10.1016/j.ceramint.2021.11.041.

38. Fu, Z., and Ferguson, J. (2022). Processing and characterization of an $Li_7La_3Zr_{0.5}Nb_{0.5}Ta_{0.5}Hf_{0.5}O_{12}$ high-entropy Li–garnet electrolyte. J. Am. Ceram. Soc. *105*, 6175–6183. https://doi.org/10.1111/jace.18576.

39. Bérardan, D., Franger, S., Meena, A.K., and Dragoe, N. (2016). Room temperature lithium superionic conductivity in high entropy oxides. J. Mater. Chem. *4*, 9536–9541. https://doi.org/10.1039/C6TA03249D.

40. Zeng, Y., Ouyang, B., Liu, J., Byeon, Y.W., Cai, Z., Miara, L.J., Wang, Y., and Ceder, G. (2022). High-entropy mechanism to boost ionic conductivity. Science *378*, 1320–1324. https://doi.org/10.1126/science.abq1346.

41. Botros, M., and Janek, J. (2022). Embracing disorder in solid-state batteries. Science *378*, 1273–1274. https://doi.org/10.1126/science.adf3383.

42. Haile, S.M., Staneff, G., and Ryu, K.H. (2001). Non-stoichiometry, grain boundary transport and chemical stability of proton conducting perovskites. J. Mater. Sci. *36*, 1149–1160. https://doi.org/10.1023/A:1004877708871.

43. Shannon, R.D. (1976). Revised effective ionic radii and systematic studies of interatomic distances in halides and chalcogenides. Acta Crystallogr. A *32*, 751–767. https://doi.org/10.1107/S0567739476001551.

Please cite this article in press as: Ko et al., Compositionally complex perovskite oxides: Discovering a new class of solid electrolytes with interface-enabled conductivity improvements, Matter (2023), https://doi.org/10.1016/j.matt.2023.05.035

44. Yu, R., Du, Q.-X., Zou, B.-K., Wen, Z.-Y., and Chen, C.-H. (2016). Synthesis and characterization of perovskite-type (Li,Sr)(Zr,Nb)O_3 quaternary solid electrolyte for all-solid-state batteries. J. Power Sources *306*, 623–629. https://doi.org/10.1016/j.jpowsour.2015.12.065.

45. Kong, Y., Li, Y., Li, J., Hu, C., Wang, X., and Lu, J. (2018). Li ion conduction of perovskite $Li_{0.375}Sr_{0.4375}Ti_{0.25}Ta_{0.75}O_3$ and related compounds. Ceram. Int. *44*, 3947–3950. https://doi.org/10.1016/j.ceramint.2017.11.186.

46. Thangadurai, V., Shukla, A.K., and Gopalakrishnan, J. (1999). $LiSr_{1.65}\square_{0.35}B_{1.3}B'_{1.7}O_9$ (B = Ti, Zr; B' = Nb, Ta) : new lithium ion conductors based on the Perovskite structure. Chem. Mater. *11*, 835–839. https://doi.org/10.1021/cm9810382.

47. Inaguma, Y., Liquan, C., Itoh, M., Nakamura, T., Uchida, T., Ikuta, H., and Wakihara, M. (1993). High ionic conductivity in lithium lanthanum titanate. Solid State Commun. *86*, 689–693. https://doi.org/10.1016/0038-1098(93)90841-A.

48. Bartoszek, J., Liu, Y.-X., Karczewski, J., Wang, S.-F., Mrozinski, A., and Jasinski, P. (2017). Distribution of relaxation times as a method of separation and identification of complex processes measured by impedance spectroscopy. In 21st European Microelectronics and Packaging Conference (EMPC) & Exhibition (IEEE),, pp. 1–5. https://doi.org/10.23919/EMPC.2017.8346901.

49. Braun, P., Uhlmann, C., Weber, A., Störmer, H., Gerthsen, D., and Ivers-Tiffée, E. (2017). Separation of the bulk and grain boundary contributions to the total conductivity of solid lithium-ion conducting electrolytes. J. Electroceram. *38*, 157–167. https://doi.org/10.1007/s10832-016-0061-y.

50. Dierickx, S., Weber, A., and Ivers-Tiffée, E. (2020). How the distribution of relaxation times enhances complex equivalent circuit models for fuel cells. Electrochim. Acta *355*, 136764.

51. Paul, T., Chi, P.W., Wu, P.M., and Wu, M.K. (2021). Computation of distribution of relaxation times by Tikhonov regularization for Li ion batteries: usage of L-curve method. Sci. Rep. *11*, 12624. https://doi.org/10.1038/s41598-021-91871-3.

52. Symington, A.R., Molinari, M., Dawson, J.A., Statham, J.M., Purton, J., Canepa, P., and Parker, S.C. (2021). Elucidating the nature of grain boundary resistance in lithium lanthanum titanate. J. Mater. Chem. *9*, 6487–6498. https://doi.org/10.1039/D0TA11539H.

53. Lee, T., Qi, J., Gadre, C.A., Huyan, H., Ko, S.-T., Zuo, Y., Du, C., Li, J., Aoki, T., Wu, R., et al. (2023). Atomic-scale origin of the low grain-boundary resistance in perovskite solid electrolyte $Li_{0.375}Sr_{0.4375}Ta_{0.75}Zr_{0.25}O_3$. Nat. Commun. *14*, 1940. https://doi.org/10.1038/s41467-023-37115-6.

54. Dawson, J.A., Canepa, P., Famprikis, T., Masquelier, C., and Islam, M.S. (2018). Atomic-scale influence of grain boundaries on Li-ion conduction in solid electrolytes for all-solid-state batteries. J. Am. Chem. Soc. *140*, 362–368. https://doi.org/10.1021/jacs.7b10593.

55. Kozinsky, B. (2020). Transport in frustrated and disordered solid electrolytes. In Handbook of Materials Modeling (Springer International Publishing), pp. 1255–1274. https://doi.org/10.1007/978-3-319-44680-6_54.

56. Kuhn, A., Duppel, V., and Lotsch, B.V. (2013). Tetragonal $Li_{10}GeP_2S_{12}$ and Li_7GePS_8 – exploring the Li ion dynamics in LGPS Li electrolytes. Energy Environ. Sci. *6*, 3548. https://doi.org/10.1039/c3ee41728j.

57. Kuhn, A., Gerbig, O., Zhu, C., Falkenberg, F., Maier, J., and Lotsch, B.V. (2014). A new ultrafast superionic Li-conductor: ion dynamics in $Li_{11}Si_2PS_{12}$ and comparison with other tetragonal LGPS-type electrolytes. Phys. Chem. Chem. Phys. *16*, 14669–14674. https://doi.org/10.1039/C4CP02046D.

58. Sun, K., Lan, Z., Yu, Z., Li, L., and Huang, J. (2008). Grain growth and magnetic properties of Nb_2O_5 -doped NiZn ferrites. Jpn. J. Appl. Phys. *47*, 7871–7875. https://doi.org/10.1143/JJAP.47.7871.

59. Zaspalis, V.T., Antoniadis, E., Papazoglou, E., Tsakaloudi, V., Nalbandian, L., and Sikalidis, C.A. (2002). The effect of Nb_2O_5 dopant on the structural and magnetic properties of MnZn-ferrites. J. Magn. Magn Mater. *250*, 98–109. https://doi.org/10.1016/S0304-8853(02)00367-0.

60. Kobayashi, S., Yokoe, D., Fujiwara, Y., Kawahara, K., Ikuhara, Y., and Kuwabara, A. (2022). Lithium lanthanum titanate single crystals: dependence of lithium-ion conductivity on crystal domain orientation. Nano Lett. *22*, 5516–5522. https://doi.org/10.1021/acs.nanolett.2c01655.

61. Kataoka, K., Nagata, H., and Akimoto, J. (2018). Lithium-ion conducting oxide single crystal as solid electrolyte for advanced lithium battery application. Sci. Rep. *8*, 9965. https://doi.org/10.1038/s41598-018-27851-x.

62. Gupta, V.K., Yoon, D.-H., Meyer, H.M., and Luo, J. (2007). Thin intergranular films and solid-state activated sintering in nickel-doped tungsten. Acta Mater. *55*, 3131–3142. https://doi.org/10.1016/j.actamat.2007.01.017.

63. Luo, J.C., Lin, H.Y., Lu, C.L., Chen, T.S., Lin, H.C., Li, C.P., Liao, W.C., Chang, F.Y., and Lee, S.D. (2008). Liquid-like interface complexion: from activated sintering to grain boundary diagrams. Transl. Res. *152*, 81–87. https://doi.org/10.1016/j.cossms.2008.12.001.

64. Luo, J. (2012). Developing interfacial phase diagrams for applications in activated sintering and beyond: current status and future directions. J. Am. Ceram. Soc. *95*, 2358–2371. https://doi.org/10.1111/j.1551-2916.2011.05059.x.

65. Luo, J., Gupta, V.K., Yoon, D.H., and Meyer, H.M. (2005). Segregation-induced grain boundary premelting in nickel-doped tungsten. Appl. Phys. Lett. *87*, 231902. https://doi.org/10.1063/1.2138796.

66. Luo, J., Wang, H., and Chiang, Y.M. (1999). Origin of solid-state activated sintering in Bi_2O_3-doped ZnO. J. Am. Ceram. Soc. *82*, 916–920. https://doi.org/10.1111/j.1151-2916.1999.tb01853.x.

67. Luo, Z., Hu, C., Xie, L., Nie, H., Xiang, C., Gu, X., He, J., Zhang, W., Yu, Z., and Luo, J. (2020). A highly asymmetric interfacial superstructure in WC: expanding the classic grain boundary segregation and new complexion theories. Mater. Horiz. *7*, 173–180. https://doi.org/10.1039/C9MH00969H.

68. Luo, J. (2007). Stabilization of nanoscale quasi-liquid interfacial films in inorganic materials: a review and critical assessment. Crit. Rev. Solid State Mater. Sci. *32*, 67–109. https://doi.org/10.1080/10408430701364388.

69. Hu, T., Yang, S., Zhou, N., Zhang, Y., and Luo, J. (2018). Role of disordered bipolar complexions on the sulfur embrittlement of nickel general grain boundaries. Nat. Commun. *9*, 2764. https://doi.org/10.1038/s41467-018-05070-2.

70. Cantwell, P.R., Tang, M., Dillon, S.J., Luo, J., Rohrer, G.S., and Harmer, M.P. (2014). Grain boundary complexions. Acta Mater. *62*, 1–48. https://doi.org/10.1016/j.actamat.2013.07.037.

71. Hu, C., and Luo, J. (2022). Data-driven prediction of grain boundary segregation and disordering in high-entropy alloys in a 5D space. Mater. Horiz. *9*, 1023–1035. https://doi.org/10.1039/d1mh01204e.

72. Dufficy, M.K., Huang, S.-Y., Khan, S.A., and Fedkiw, P.S. (2017). Effects of composition and structure on the performance of tin/graphene-containing carbon nanofibers for Li-ion anodes. RSC Adv. *7*, 15428–15438. https://doi.org/10.1039/C6RA26371B.

73. Zhu, Y., He, X., and Mo, Y. (2015). Origin of outstanding stability in the lithium solid electrolyte materials: insights from thermodynamic analyses based on first-principles calculations. ACS Appl. Mater. Interfaces *7*, 23685–23693. https://doi.org/10.1021/acsami.5b07517.

74. Ramesh, S., Upender, G., Raju, K.C.J., Padmaja, G., Reddy, S.M., and Reddy, C.V. (2013). Effect of Ca on the properties of Gd-doped ceria for IT-SOFC. J. Mod. Phys. *04*, 859–863. https://doi.org/10.4236/jmp.2013.46116.

75. Shapeev, A.V. (2016). Moment tensor potentials: a class of systematically improvable interatomic potentials. Multiscale Model. Simul. *14*, 1153–1173. https://doi.org/10.1137/15M1054183.

76. Gubaev, K., Podryabinkin, E.V., Hart, G.L., and Shapeev, A.V. (2019). Accelerating high-throughput searches for new alloys with active learning of interatomic potentials. Comput. Mater. Sci. *156*, 148–156. https://doi.org/10.1016/j.commatsci.2018.09.031.

77. Podryabinkin, E.V., and Shapeev, A.V. (2017). Active learning of linearly parametrized interatomic potentials. Comput. Mater. Sci. *140*, 171–180. https://doi.org/10.1016/j.commatsci.2017.08.031.

78. Novikov, I.S., Gubaev, K., Podryabinkin, E.V., and Shapeev, A.V. (2021). The MLIP package: moment tensor potentials with MPI and active learning. Mach. Learn, Sci. Technol. *2*, 025002. https://doi.org/10.1088/2632-2153/abc9fe.

79. Plimpton, S. (1995). Fast parallel algorithms for short-range molecular dynamics. J. Comput. Phys. *117*, 1–19. https://doi.org/10.1006/jcph.1995.1039.

Matter, Volume *6*

Supplemental information

Compositionally complex perovskite oxides: Discovering a new class of solid electrolytes with interface-enabled conductivity improvements

Shu-Ting Ko, Tom Lee, Ji Qi, Dawei Zhang, Wei-Tao Peng, Xin Wang, Wei-Che Tsai, Shikai Sun, Zhaokun Wang, William J. Bowman, Shyue Ping Ong, Xiaoqing Pan, and Jian Luo

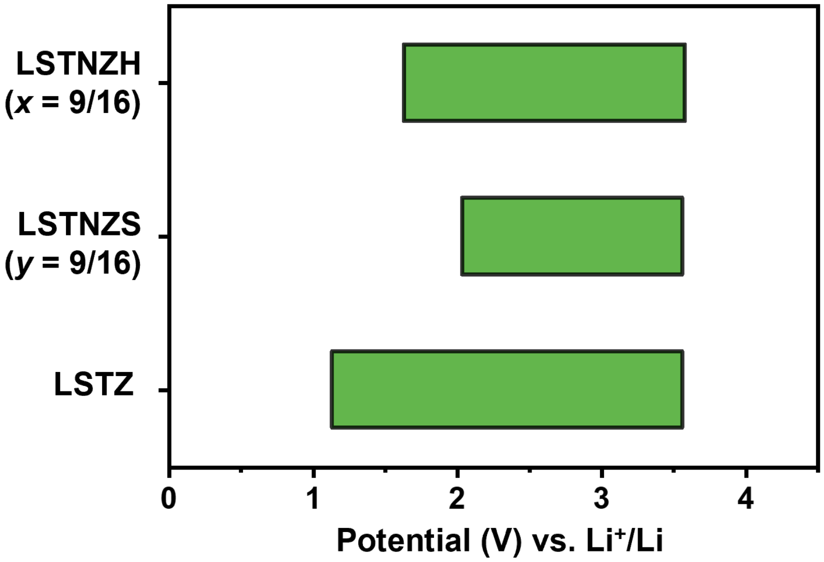

Figure S1. Thermodynamic electrochemical potential windows of LSTNZH (*x* = 9/16), LSTNZS (*y* = 9/16), and LSTZ (from top to bottom) according to the calculated grand potential phase diagrams using the Materials Project database
LSTNZH (*x* = 9/16) and LSTNZS (*y* = 9/16) retain metastable structures at 1.63-3.58 V and 2.04-3.56 V, respectively. By comparison, LSTZ is stable at 1.13-3.56 V.

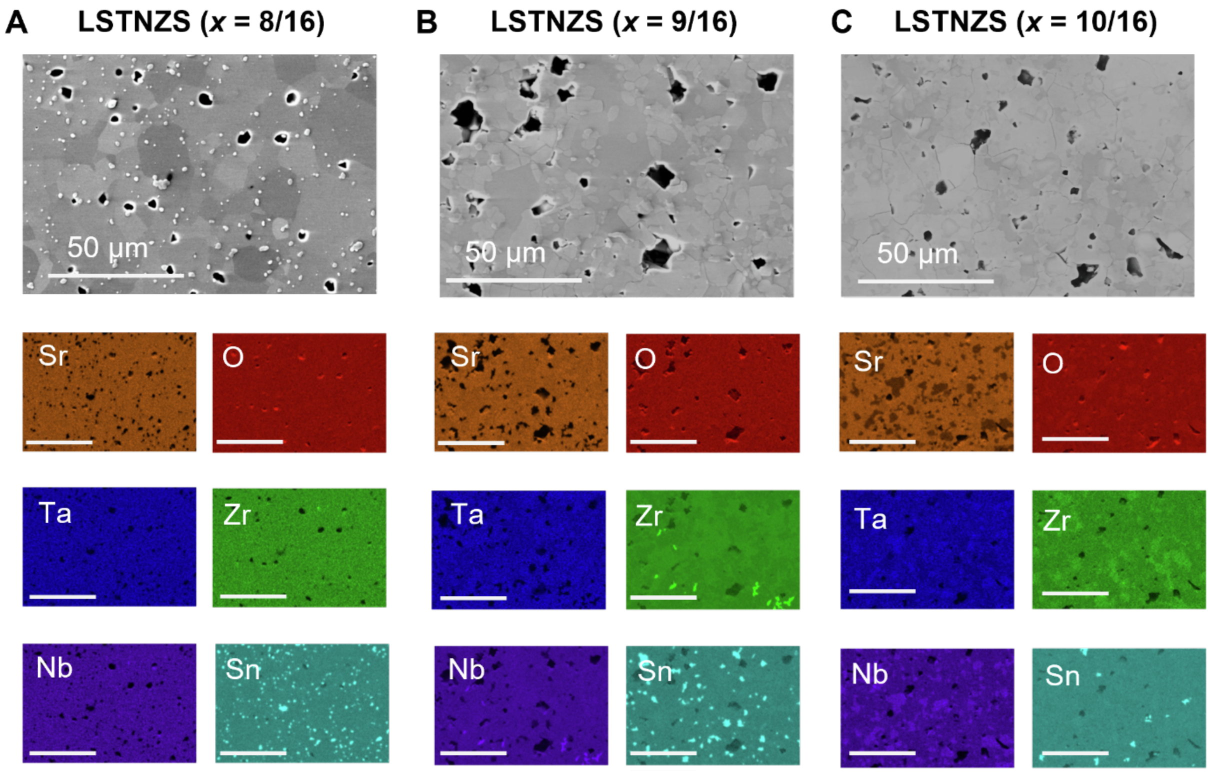

Figure S2. SEM-EDS elemental maps for the LSTNZS *x* series
(A) to (C) present elemental distribution maps of (A) LSTNZS (*x* = 8/16), (B) LSTNZS (*x* = 9/16) and (C) LSTNZS (*x* =10/16), based on Sr-Lα1 (orange), Ta-Lα1 (blue), Nb-Lα1 (purple), Zr-Lα1 (green), Sn-Lα1 (aqua) and O-Kα1 (red) peaks. The scale bar is 50 µm.

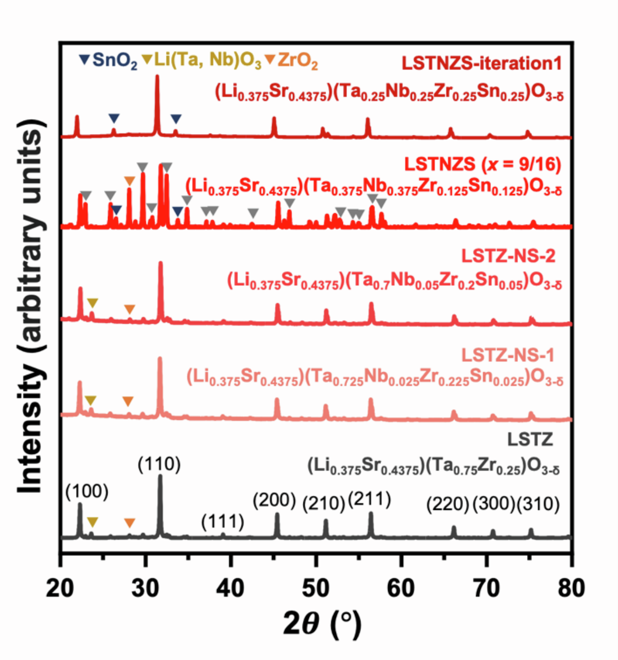

Figure S3. B-site stoichiometry effect on the phase stability of the Nb and Sn co-doped LSTZ-NS series $(Li_{0.375}Sr_{0.4375})(Ta_{0.75-k}Nb_{k}Zr_{0.25-k}Sn_{k})O_{3-\delta}$ (*k* = 0.025, 0.05), LSTNZS (*x* = 9/16) and the LSTNZS-iteration1 (equimolar B-site cations), benchmarked with the LSTZ

The XRD patterns from the bottom to top are patterns of the LSTZ, LSTZ-NS-1 (*k* = 0.025), LSTZ-NS-2 (*k* = 0.05), LSTNZS (*x* = 9/16), and LSTNZS-iteration1 with equimolar B-site cations. Given the same A-site stoichiometry, the phase instability becomes pronounced when the half of Ta^{5+} sites and the half of Zr^{4+} sites are replaced by Nb^{5+} and Hf^{4+} with 5B:4B = 3:1 by molar to maintain the charge balance. The secondary phases are suppressed again when B-site cations are equimolar with 5B:4B = 1:1 by molar and the configurational entropy of the B site is maximized despite of the slight deviation from charge balance. The secondary phases are indicated as: SnO_2 (blue), Li(Ta, Nb)O_3 (brown) and ZrO_2 (orange).

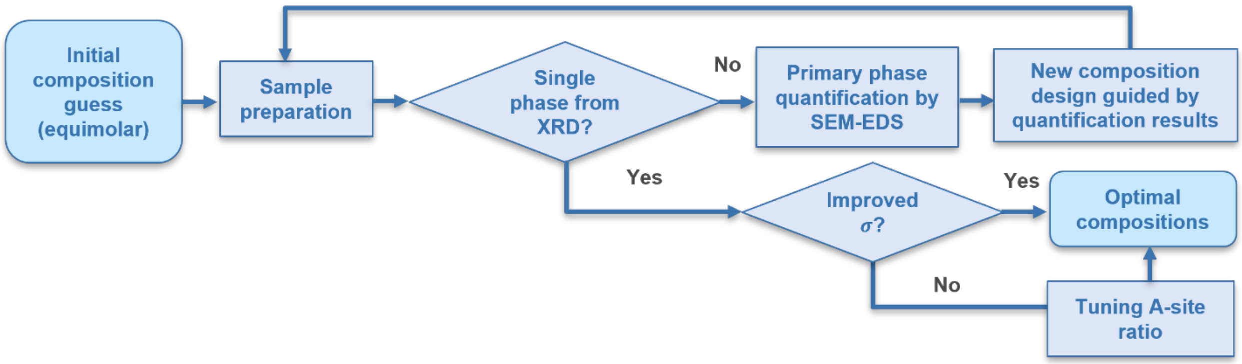

Figure S4. The composition optimization methodology adopted in this work following a "natural selection" rule

In the optimization iteration loop, an initial composition guess was given: $(Li_{0.375}Sr_{0.4375})(Ta_{0.25}Nb_{0.25}Zr_{0.25}Sn_{0.25})O_{3-\delta}$. After sample preparation process described in the experimental procedures section, the samples were characterized by XRD to determine phase stability. If the samples presented trace/no secondary phases, the impedance measurements were conducted to evaluate ionic conductivity. If not, the cation ratio at the primary phase region was quantified using SEM-EDS, and the new composition was designed following the quantified ratio. At the end of the iterations, if the measured ionic conductivity was not enhanced, A-site cation ratio was further tuned to maximize the performance.

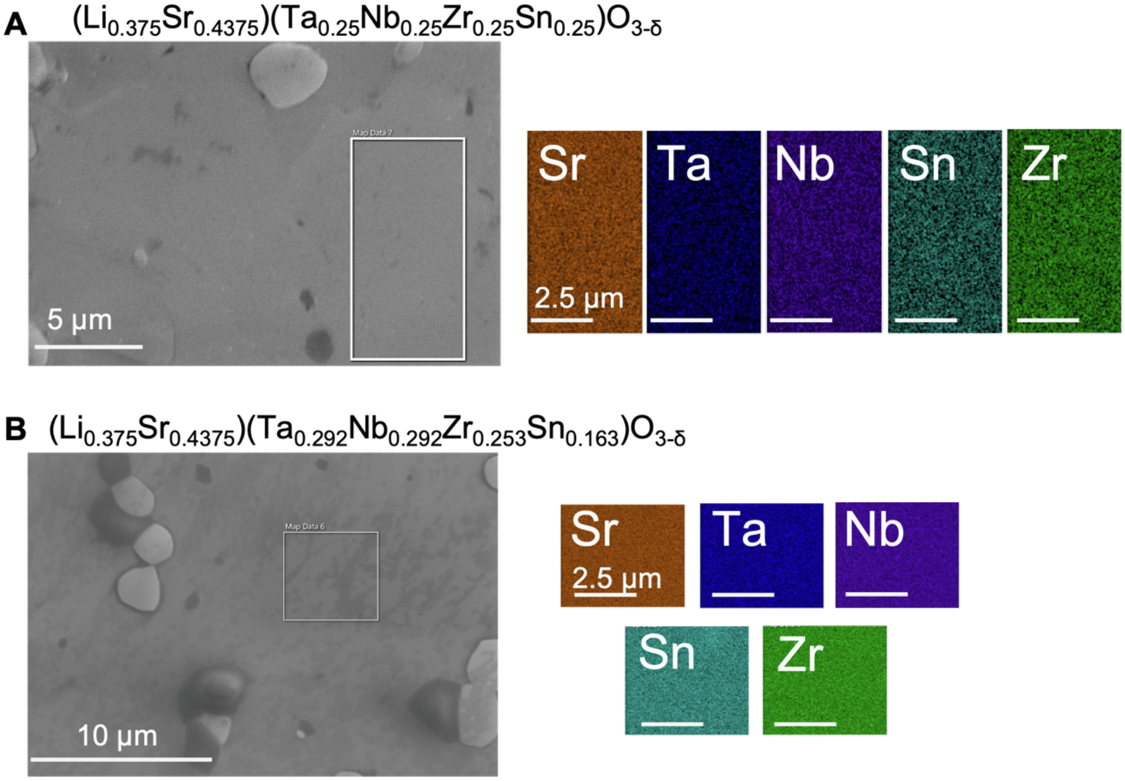

A $(Li_{0.375}Sr_{0.4375})(Ta_{0.25}Nb_{0.25}Zr_{0.25}Sn_{0.25})O_{3-\delta}$

B $(Li_{0.375}Sr_{0.4375})(Ta_{0.292}Nb_{0.292}Zr_{0.253}Sn_{0.163})O_{3-\delta}$

Figure S5. SEM-EDS elemental maps at the primary phase regions of LSTNZS-iteration1 and LSTNZS-iteration2 in the composition optimization loops described in Figure S4

(A) and (B) present primary-phase elemental distribution maps of (A) the initial LSTNZS-iteration1 with equimolar B-site cations and (B) LSTNZS-iteration2 with non-equimolar B-site cations. The maps are from the Sr-Lα1 (orange), Ta-Lα1 (blue), Nb-Lα1 (purple), Zr-Lα1 (green) and Sn-Lα1 (aqua) peaks. The homogeneous elemental distribution justifies the selection of the primary phase regions. The quantification results are shown in Table S5. Notably, the contrast and brightness of maps are scaled automatically during data collection and have variations between different samples.

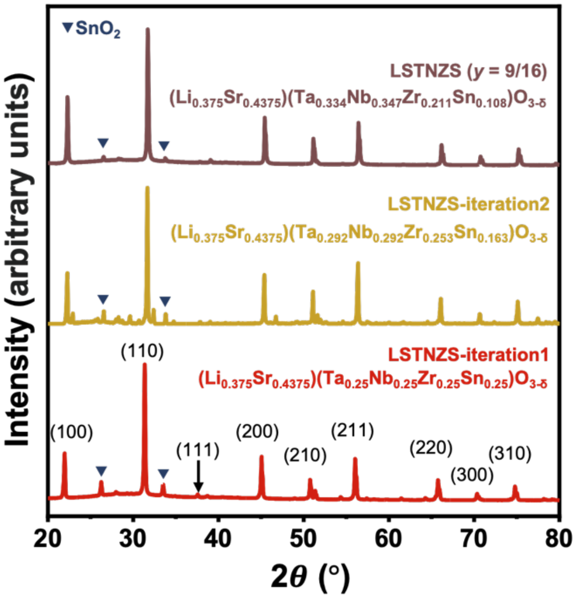

Figure S6. Phase stability comparison of CCPOs developed in the composition optimization loop
The XRD patterns from the bottom to top are patterns of the LSTNZS-iteration1, LSTNZS-iteration2, and LSTNZS (y = 9/16) designed based on LSTNZS-iteration2. With fixed A-site stoichiometry, the fraction of SnO_2 secondary phase (indicated by blue triangles) decreases upon changing B-site stoichiometry.

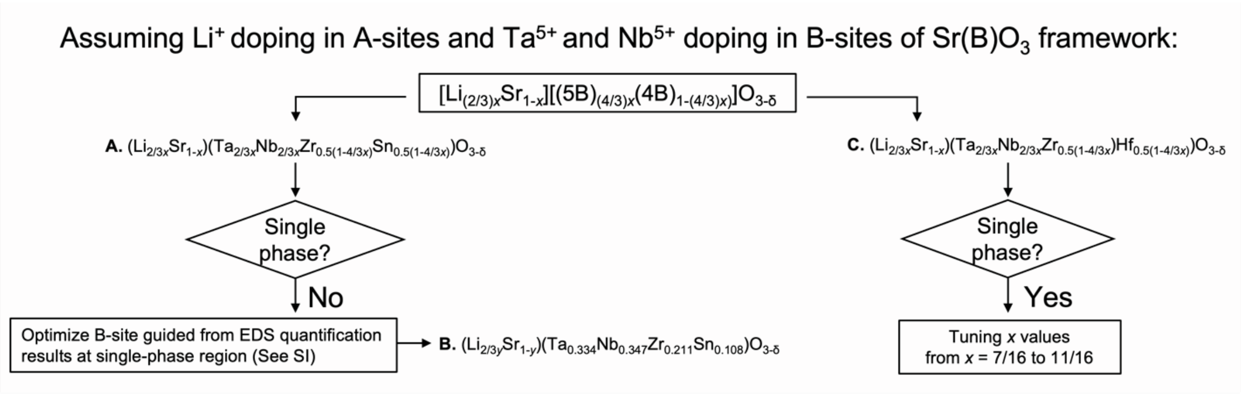

Figure S7. Composition development workflow from *x* series to *y* series

The initial x series composition design follows the assumption of A-site and B-site substitution by Li^+ and 5B cations (Ta^{5+}, Nb^{5+}). We firstly examine phase stability of samples with $x = 9/16$. If the specimen shows a single phase in $Pm\bar{3}m$ cubic structure, the x is varied to investigate the effect of x value on phase stability and ionic conductivity. If the specimen shows poor phase stability, the additional optimization strategy described in Figure S4 is used to obtain the y series.

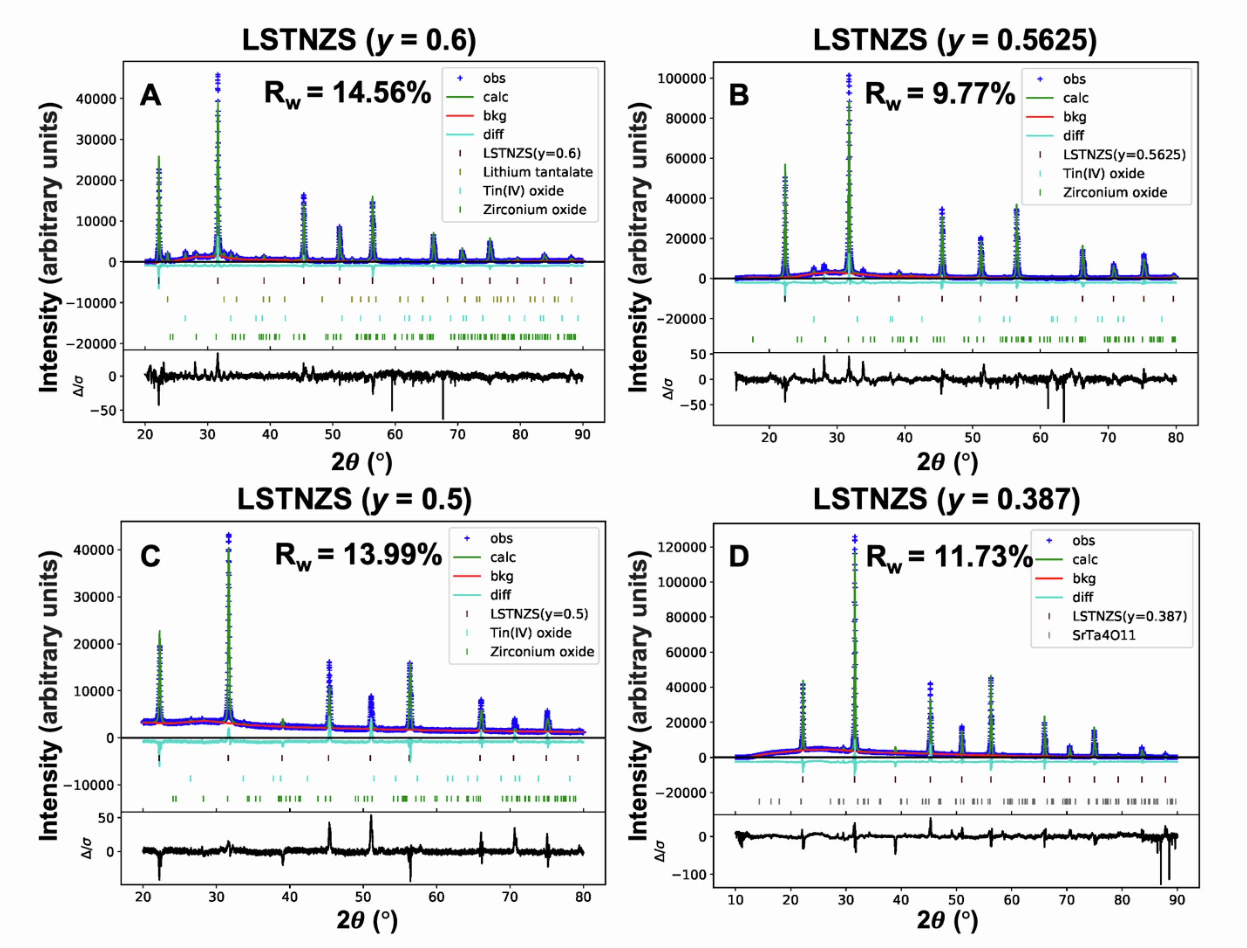

Figure S8. Rietveld refinements of XRD data of LSTNZS (*y* series)

(A)-(D) present the calculated XRD patterns (green curve) of LSTNZS samples with (A) *y* = 0.6, (B) *y* = 0.5625, (C) *y* = 0.5 and (D) *y* = 0.387. The phase identification fingerprints are primary phase (brown), SnO_2 (light blue), ZrO_2 (green), $LiTaO_3$ (yellow-green), and $SrTa_4O_{11}$ (grey). $LiTaO_3$ powder diffraction pattern was used to represent Li(Ta, Nb)O_3 phase.

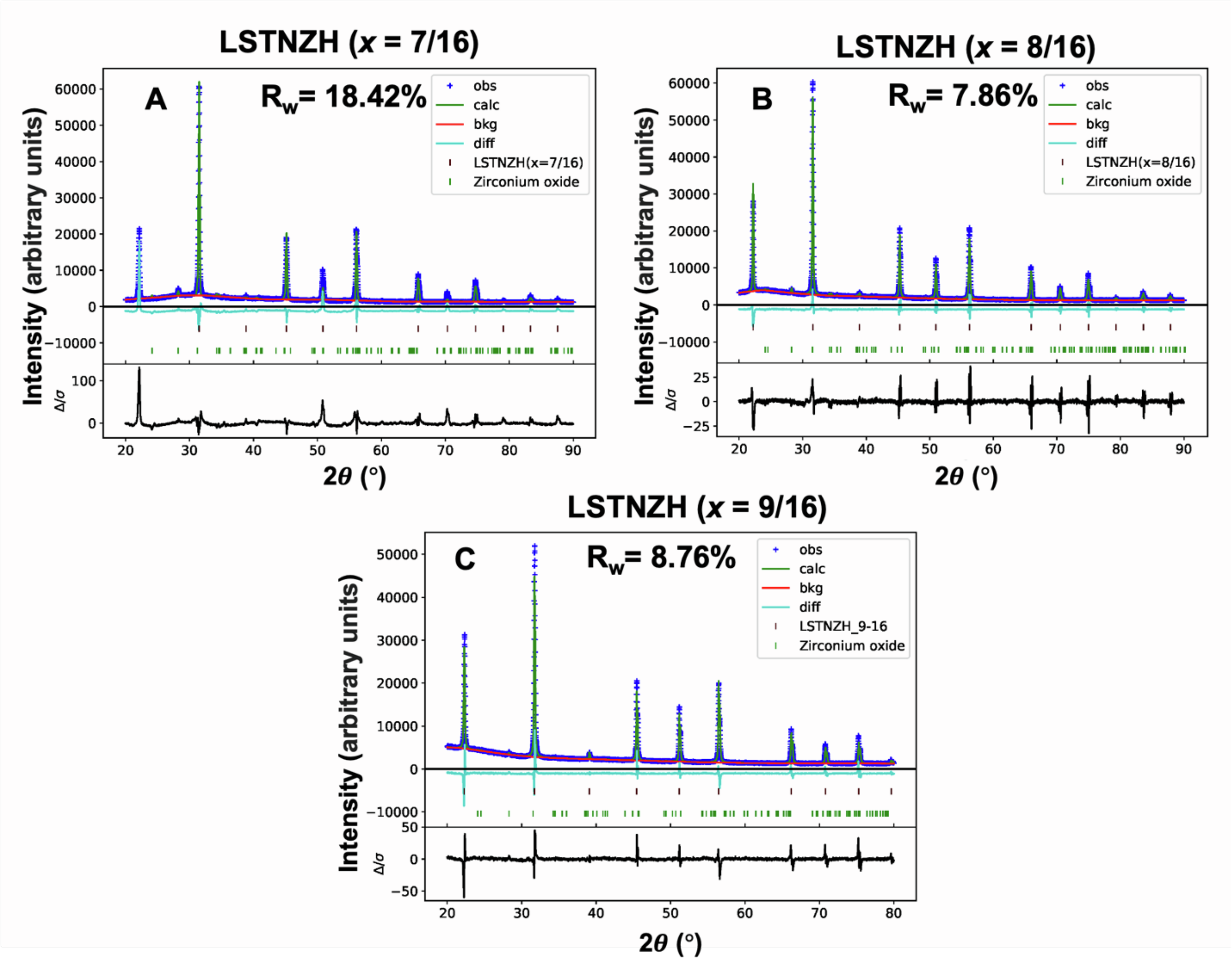

Figure S9. Rietveld refinements of XRD data of LSTNZH (*x* series)

(A)-(C) present the calculated XRD patterns (green curve) of LSTNZH samples with (A) *x* = 7/16, (B) *x* = 8/16 and (C) *x* = 9/16. The phase identification fingerprints are primary phase (brown) and ZrO_2 (green).

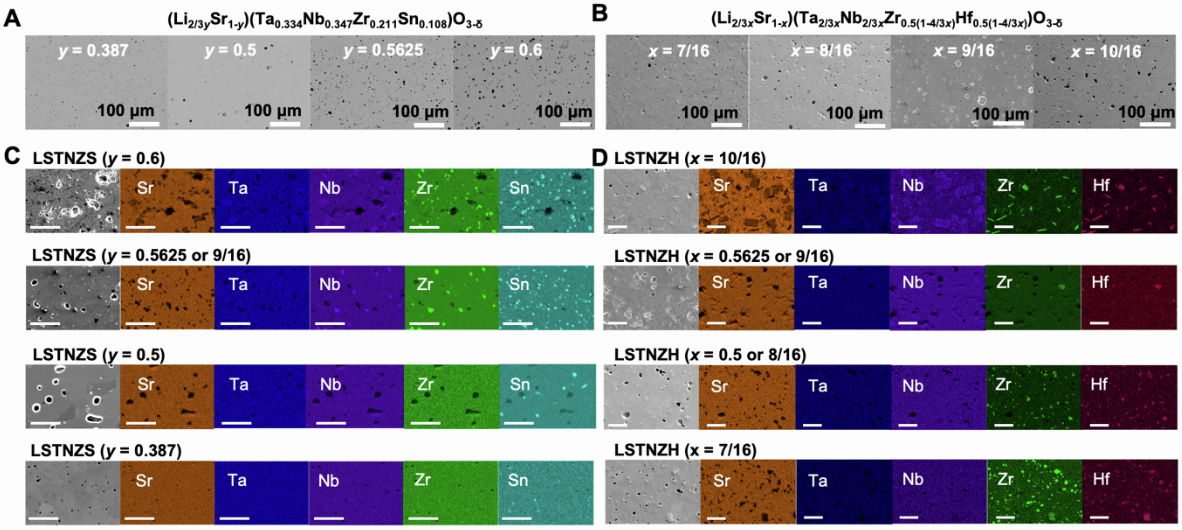

Figure S10. Morphology of polished sample surfaces and SEM-EDS maps for LSTNZS (*y* series) and LSTNZH (*x* series)

(A) and (B) present sample morphology of (A) LSTNZS (*y* series) from *y* = 0.387 to 0.6 (left to right) and (B) LSTNZH (*x* series) from *x* = 7/16 to 10/16 (left to right) from SEM images. As-sintered pellets show relative density of over 97%. As *y* and *x* values get larger, the sample porosity gets higher. (C) and (D) display the EDS maps of elemental distribution of (C) LSTNZS (*y* series) from *y* = 0.387 to 0.6 (bottom to top) and (B) LSTNZH (*x* series) from *x* = 7/16 to 10/16 (bottom to top). As *y* increases from 0.387 to 0.5, SnO_2 formation becomes pronounced because of the increase of Li/Sr molar ratio. When *y* = 0.5625, ZrO_2 starts to form. Finally, Nb segregation at *y* = 0.6 indicates the formation of $LiTaO_3$/$LiNbO_3$ as Li/Sr molar ratio is approaching 1 and A-site to B-site valence ratio is close to 0.2 for $A^{1+}B^{5+}O_3$. On the other hand, the ZrO_2 and HfO_2 secondary phase fraction is the least for LSTNZH (*x* = 9/16). As *x* increases or decreases from 9/16, more amounts of ZrO_2 and HfO_2 are observed.

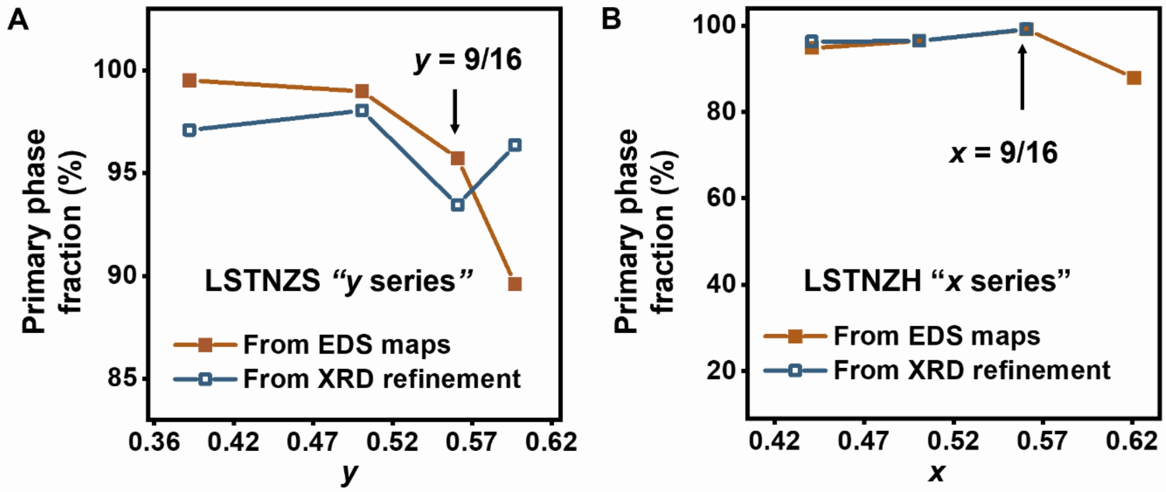

Figure S11. The comparison of primary phase fraction quantification using SEM-EDS image analyses *vs.* XRD Rietveld refinements

The primary phase fractions are quantified for (A) LSTNZS (*y* series) and for LSTNZH (*x* series) by imaging processing on EDS maps (brown dots and lines) and by XRD refinement (navy blue dots and lines). The Rietveld refinement accuracy is too low for LSTNZH (x = 10/16) due to the overlap of XRD peaks of multiple secondary phases (ZrO_2, Li(Ta, Nb)O_3, and Ta_2O_5). Thus, it is not included here.

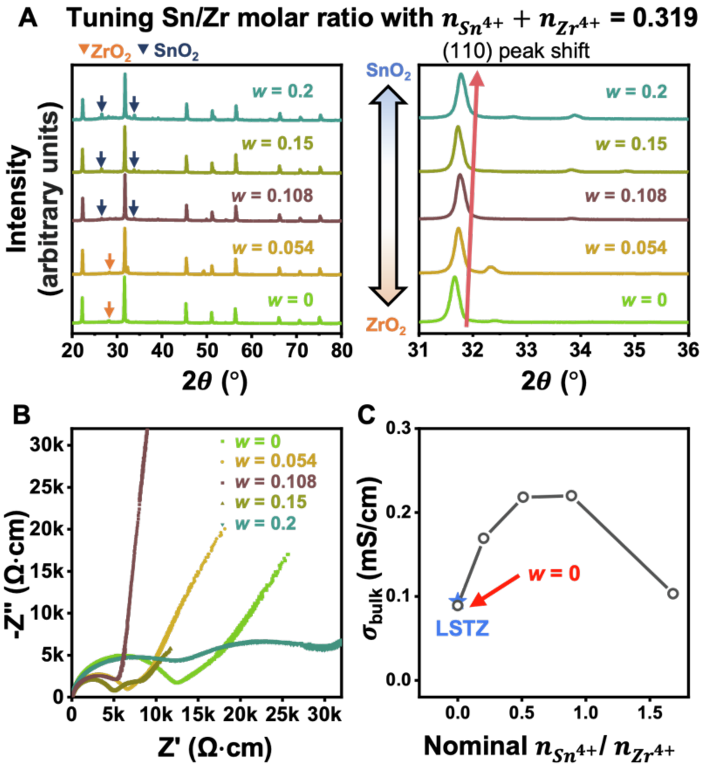

Figure S12. Phase stability and ionic conductivity characterization for LSTNZS Sn/Zr "*w* series" (A) XRD patterns of $(Li_{0.375}Sr_{0.4375})(Ta_{0.334}Nb_{0.347}Zr_{0.319-w}Sn_{w})O_{3-\delta}$ (w = 0, 0.054, 0.108, 0.15, 0.2), where ZrO_2 forms at $w < 0.108$, while SnO_2 forms at $w \geq 0.108$. The (110) peak shifts towards higher diffraction angle, representing a decrease in lattice constant upon Sn^{4+} substitution. (B) Nyquist plot of the overlay of impedance curves. As Sn fraction increases, the bulk resistance reduces till the SnO_2 formation becomes pronounced at w = 0.15. (C) The σ_{bulk} correlation with nominal Sn/Zr molar ratio. At w = 0, no Sn cation is in B-site, which shows similar σ_{bulk} magnitude compared to that of LSTZ. σ_{bulk} is maximized and saturated at w = 0.108 and 0.15; however, σ_{total} is smaller at w = 0.15 due to the increasing amount of SnO_2. σ_{bulk} is further reduced at w = 0.2 because of the phase instability.

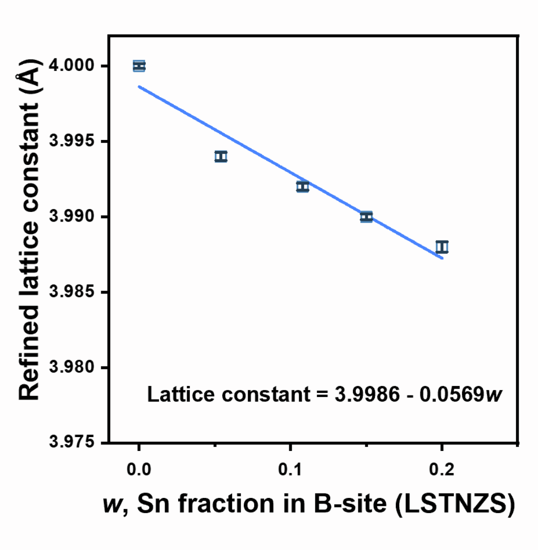

Figure S13. The change in the lattice constant with respect to the Sn fraction in the B site of LSTNZS

The refined lattice constant is plotted against *w* values in $(Li_{0.375}Sr_{0.4375})(Ta_{0.334}Nb_{0.347}Zr_{0.319-w}Sn_{w})O_{3-\delta}$. The error bars are defined as three times the estimated standard deviations from the refinements.

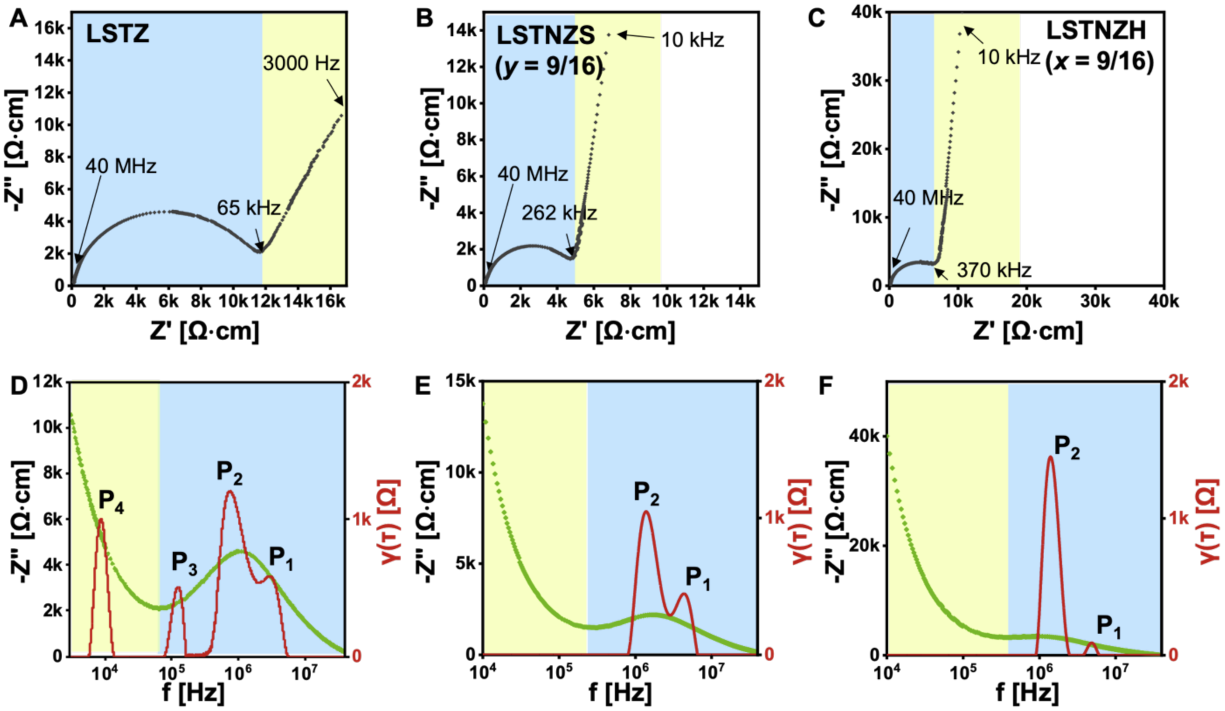

Figure S14. Distribution of relaxation time analyses of LSTZ, LSTNZS (*y* = 9/16) and LSTNZH (*x* = 9/16)

(A)-(C) The Nyquist plots as indicated: (A) LSTZ, (B) LSTNZS (*y* = 9/16) and (C) LSTNZH (*x* = 9/16). The blue shade highlights the semicircle parts at high frequency regime, whereas the yellow shade represents the low frequency regime. The overlay of Bode plots and DRT peaks is presented for (D) LSTZ, (E) LSTNZS (*y* = 9/16), and (F) LSTNZH (*x* = 9/16). P_1, P_2, and P_3 stand for responses from the bulk, and P_4 is the response from low-frequency process (GB or secondary phases). However, we are unable to fit P_4 contribution in the original Nyquist plot (Figure S15B). By comparison, P_4 is not shown in CCPOs, which indicates the change of polarization processes in CCPOs that requires further investigation.

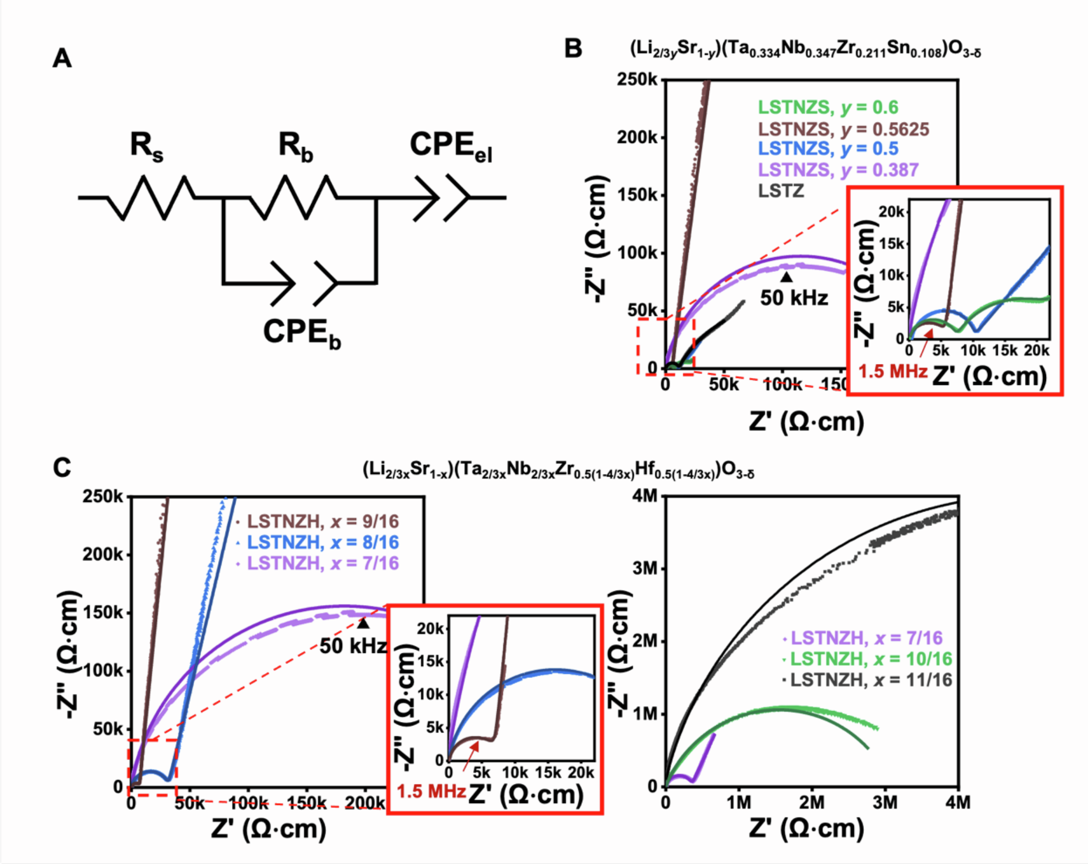

Figure S15. Nyquist plots of LSTNZS (*y* series) and LSTNZH (*x* series)

(A) The equivalent circuit model used in impedance curve fitting, which is composed of a series resistance, an RC circuit, and a constant phase element. (B) Impedance curves change upon increasing *y* values indicated as: LSTNZS (*y* = 0.387) (purple), LSTNZS (*y* = 0.5) (blue), LSTNZS (*y* = 0.5625) (brown) and LSTNZS (*y* = 0.6) (green). The smallest semicircle for LSTNZS (*y* = 0.5625) is presented in the range of 1.5 MHz shown in the enlarged figure in (B). Similarly, (C) Impedance curves as indicated as: LSTNZH (*x* = 7/16) (purple), LSTNZH (*x* = 8/16) (blue), LSTNZH (*x* = 9/16) (brown), LSTNZH (*x* = 10/16) (green), and LSTNZH (*x* = 11/16) (black). The smallest semicircle is also shown at *x* = 9/16 in the range of 1.5 MHz in the enlarged figure in (C).

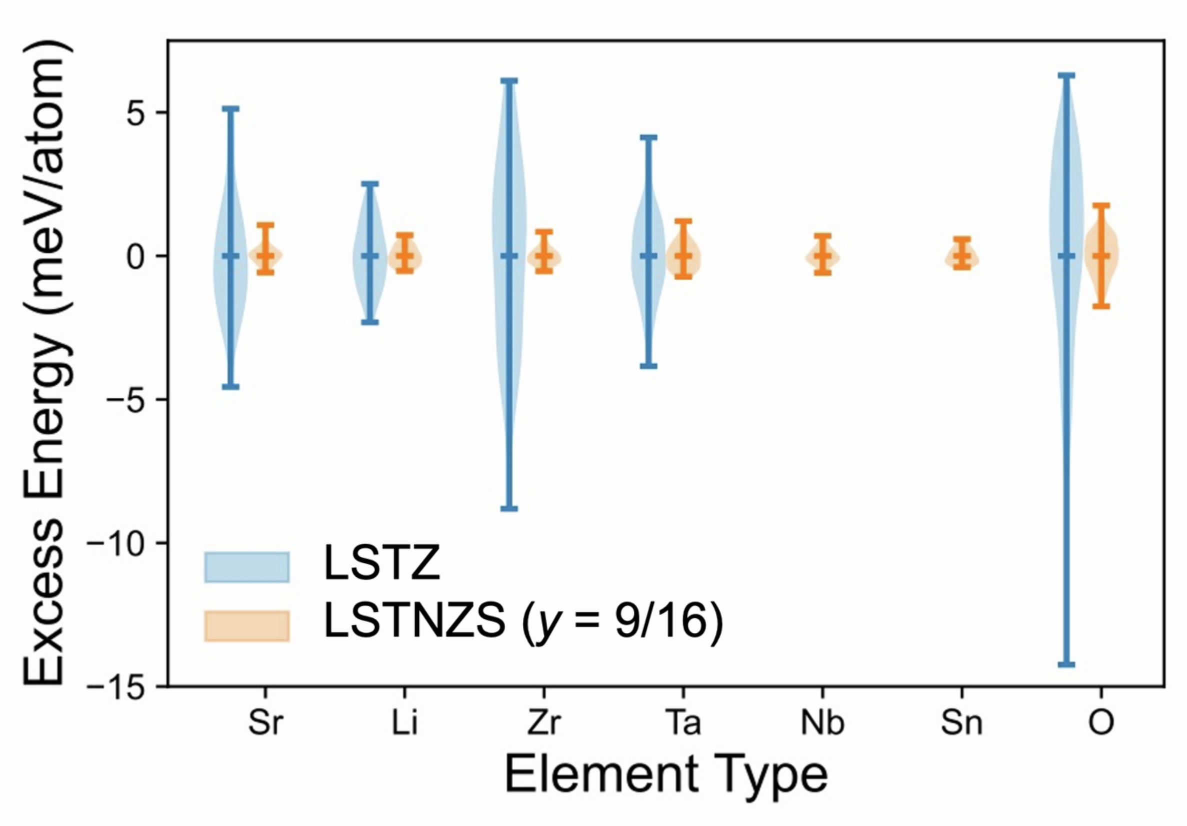

Figure S16. The distributions of excess energies calculated in LSTNZS (*y* = 9/16) and LSTZ
The calculation of excess energies of elements is described in Note S3. The distributions of excess energies for all elements in LSTNZS (*y* = 9/16) (orange) are narrower than those in LSTZ (blue), which indicates lower energy differences between different atom sites of same elements.

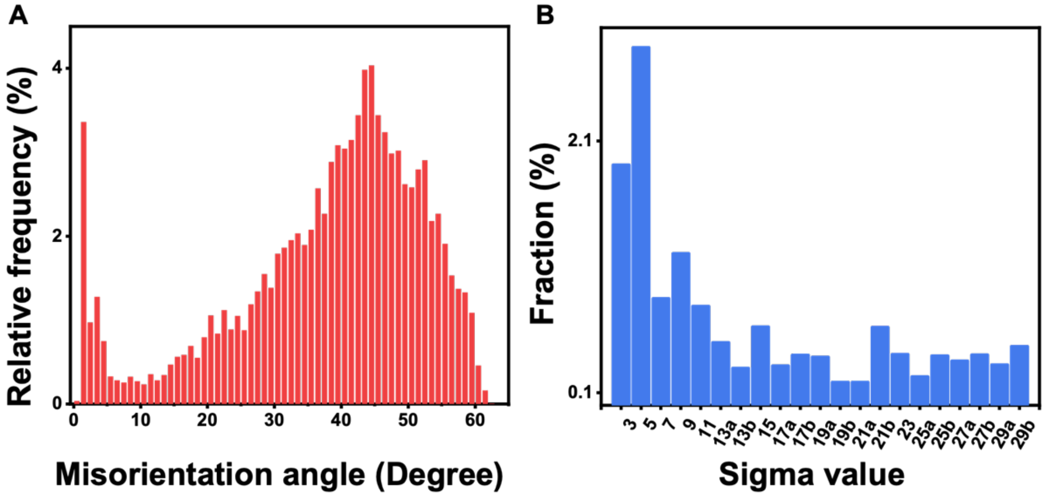

Figure S17. The misorientation angle distribution and the statistics of low-Σ GB fraction for LSTNZS (*y* = 9/16) from EBSD maps

(A) The misorientation angle distribution from 0.5 to 61.5 degrees. The distribution follows a normal grain growth, where no preferential orientation is observed. (B) The fraction of low sigma GBs from Σ3 to Σ29, where Σ3 and Σ5 GBs are dominant and most representative among low-Σ GB groups.

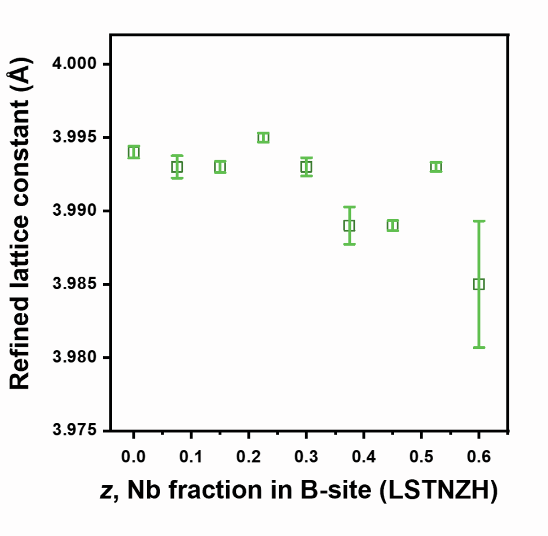

Figure S18. The change in the lattice constant with respect to the Nb fraction in the B-site of LSTNZH

The refined lattice constant is plotted against *z* values in $(Li_{0.375}Sr_{0.4375})(Ta_{0.75-z}Nb_zZr_{0.125}Hf_{0.125})O_{3-\delta}$. The error bars are defined as three times the estimated standard deviations from the refinements. The error bar becomes large in the last composition of $z = 0.6$, where multiple secondary phases are present.

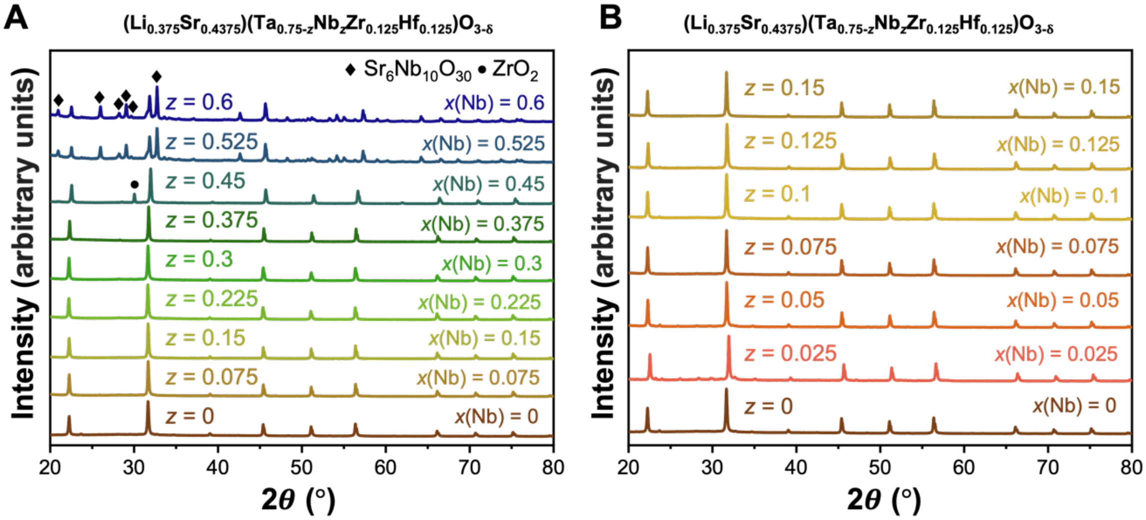

Figure S19. XRD patterns of the LSTNZH Ta/Nb "*z* series"
(A) Phase stability of $(Li_{0.375}Sr_{0.4375})(Ta_{0.75-z}Nb_zZr_{0.125}Hf_{0.125})O_{3-\delta}$ from $z = 0$ to 0.6 with an interval of 0.075. z represents the molar fraction of Nb in B site. From $z = 0$ to 0.375, the single phase is stable without observed secondary phase peaks. At $z = 0.45$, ZrO_2 peak is indicated by circle symbol. At $z = 0.525$ and 0.6, $Sr_6Nb_{10}O_{30}$ is indicated by diamond symbol. (B) Phase stability from $z = 0$ to 0.15 with an interval of 0.025, which shows single phase of cubic perovskite.

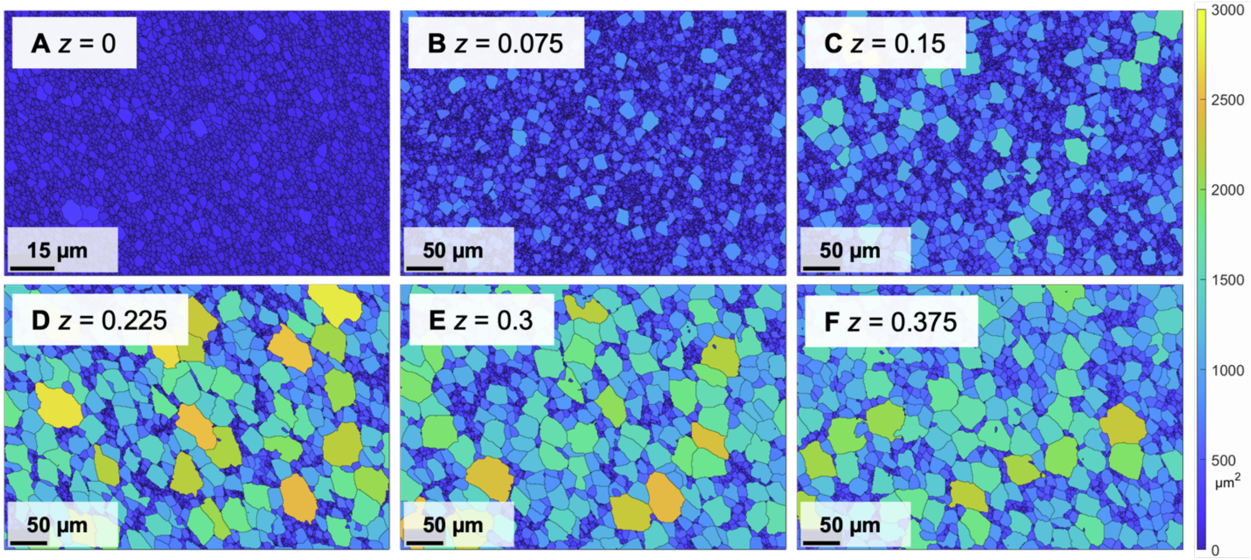

Figure S20. The spatial distribution of grains color-coded with mean grain size values for LSTNZH Ta/Nb *"z series"* in the single-phase regime

(A)-(F) The color-coded EBSD maps visualized by MTEX toolbox[S1] as indicated from $z = 0$ to $z = 0.375$. The larger grains are colored in gold; the intermediate size grains are colored in green; the smaller grains are colored in blue. An isotropic grain growth is presented without preferential growth direction.

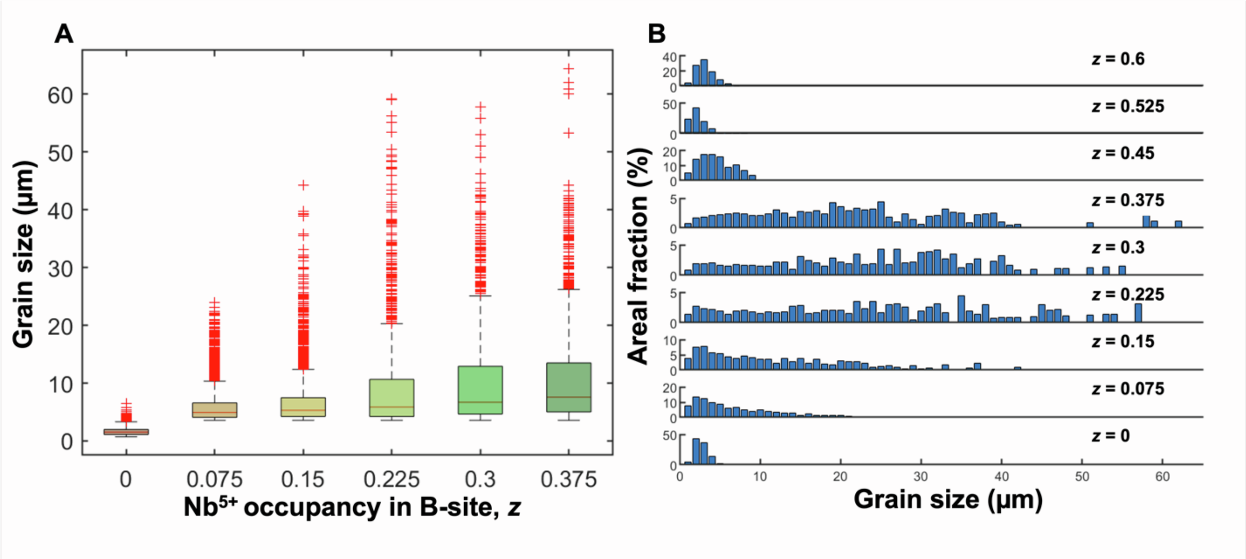

Figure S21. Statistical plots of the grain size distribution for LSTNZH Ta/Nb "*z* series" in the single-phase regime

(A) The box plot with median value as the red lines within boxes. The upper limit of a box stands for 75th percentile, while the lower limit is 25th percentile. The red cross marks represent outliners. As Nb occupancy in B-site increases to 0.375, the values of grain size median, maximum and standard deviation (SD) as well as the distribution of outliers all increased. (B) The grain size distribution in terms of areal fraction. The broader distribution and large grains are shown at *z* = 0.375.

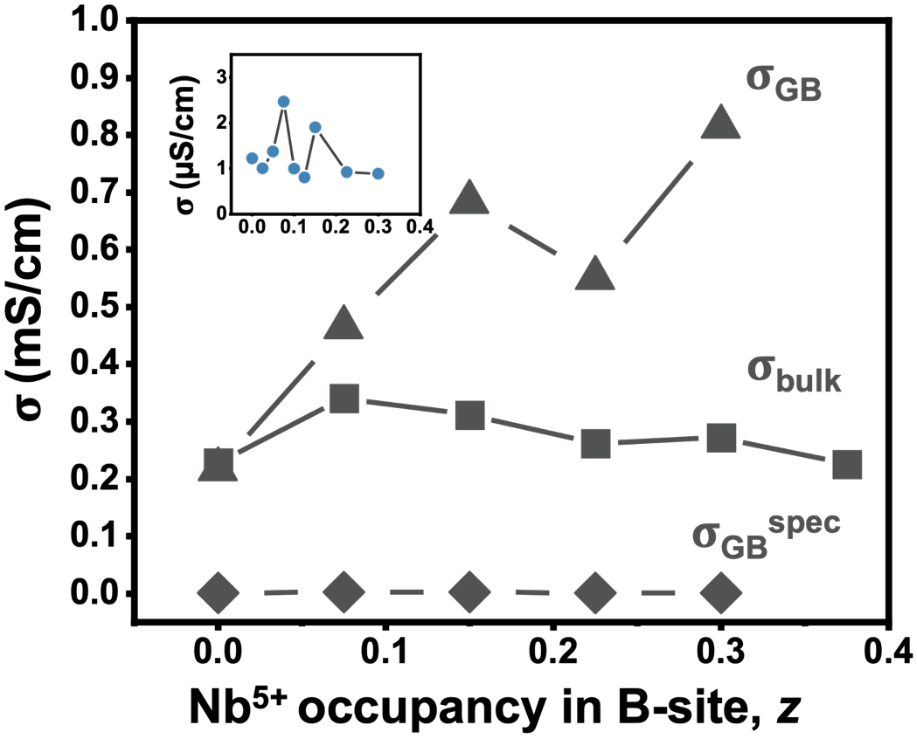

Figure S22. The correlation of the bulk ionic conductivity, GB ionic conductivity, and specific GB ionic conductivity with the Nb occupancy in the B site

The apparent GB ionic conductivity increases significantly upon increasing the Nb occupancy in B-site. In contrast, the bulk ionic conductivity is independent of Nb occupancy. The variation of specific GB ionic conductivity is shown in the inset figure on the upper left. The large variation is due to the fitting error caused by the overlapping of semicircles.

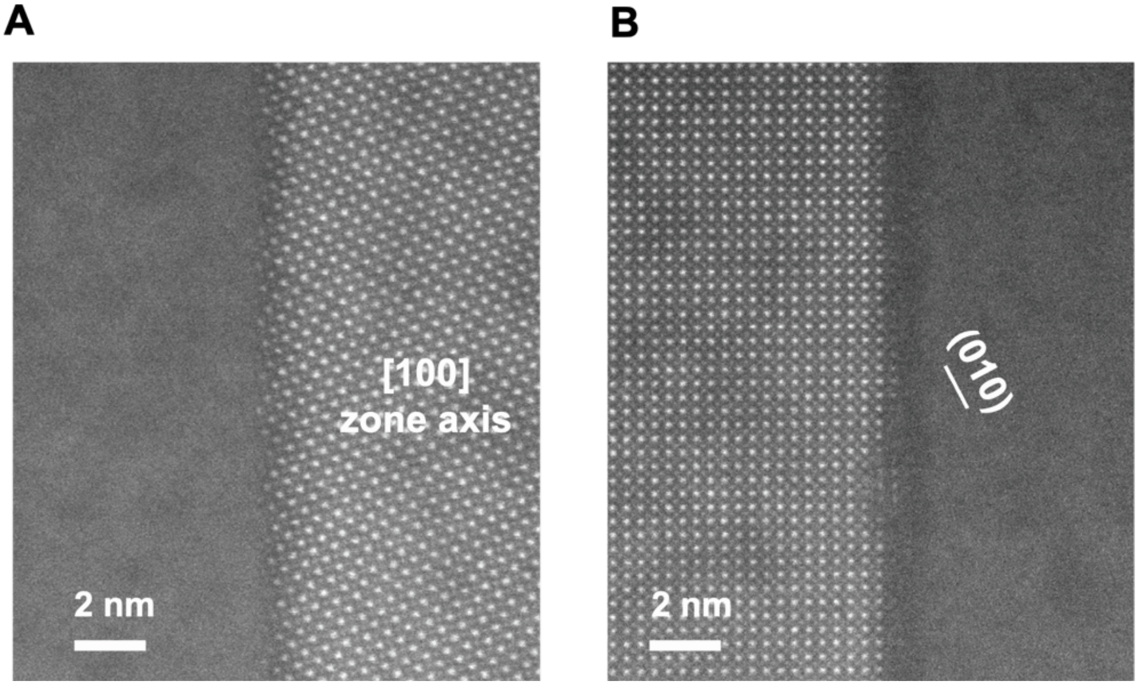

Figure S23. Atomic-scale GB structures of LSTNZS (*y* = 9/16)
Atomic-resolution HAADF-STEM images of (A) a general grain boundary and (B) a (010) faceted grain boundary (with respect to the left-side grain). The zone axes parallel with the incident electron beam were indicated. The left-side grain in (A) and right-side grain in (B) were not oriented along any particular zone axis, and the crystallographic plane corresponding to the lattice fringes was indexed for the latter.

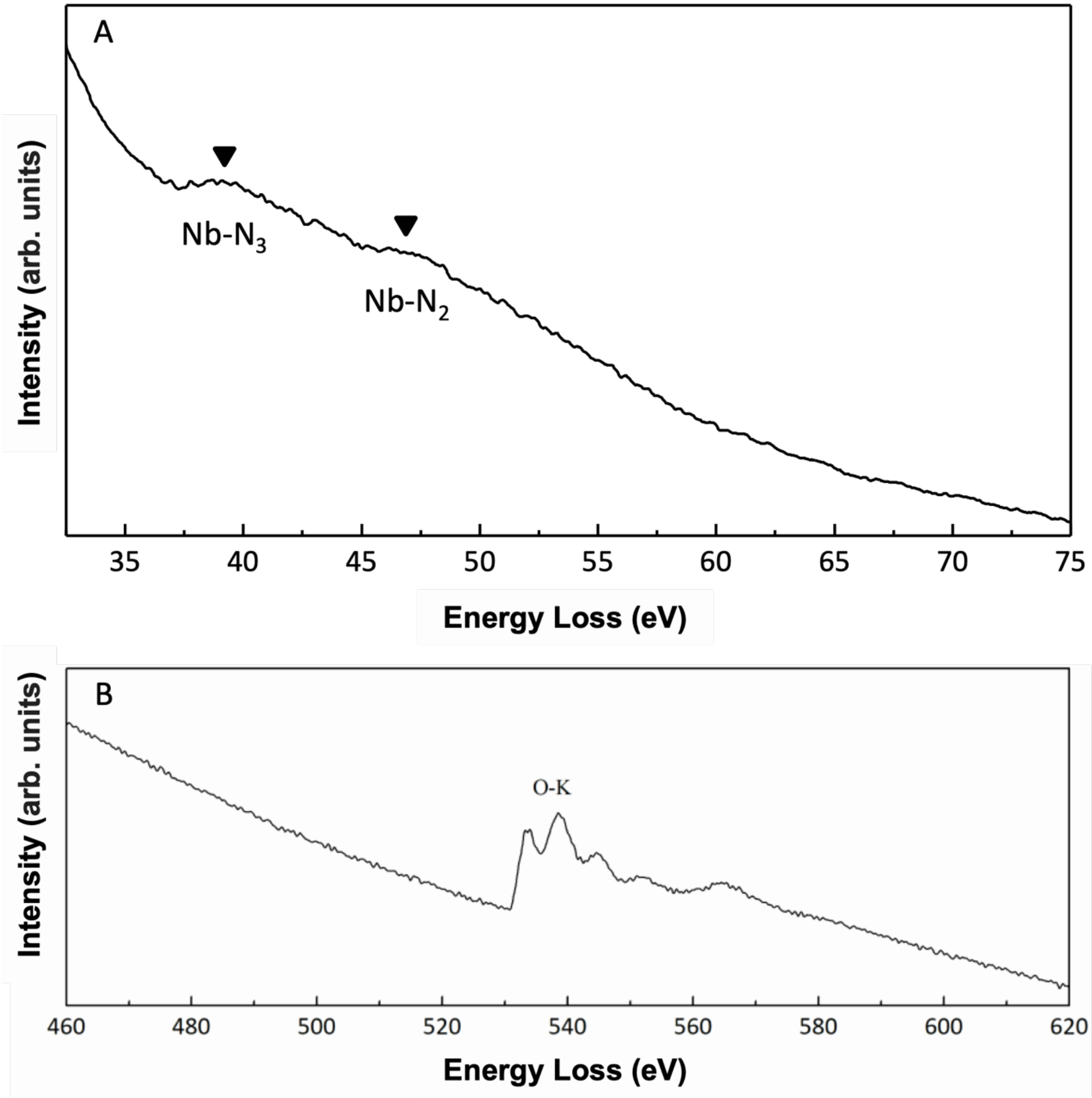

Figure S24. Distinct Li-K and Sn-M$_{4,5}$ edges of LSTNZS (*y* = 9/16) are not observed in the EELS spectra

(A) Raw integrated EELS spectrum collected at the low energy loss regime. Edge corresponding to each peak is assigned. Distinct Li-K edge of LSTNZS (*y* =9/16) is not observed due to its close proximity to the Nb-N$_{2,3}$ edge. (B) Raw integrated EELS spectrum collected at the energy loss range where Sn-M$_{4,5}$ edge is expected (485 eV).

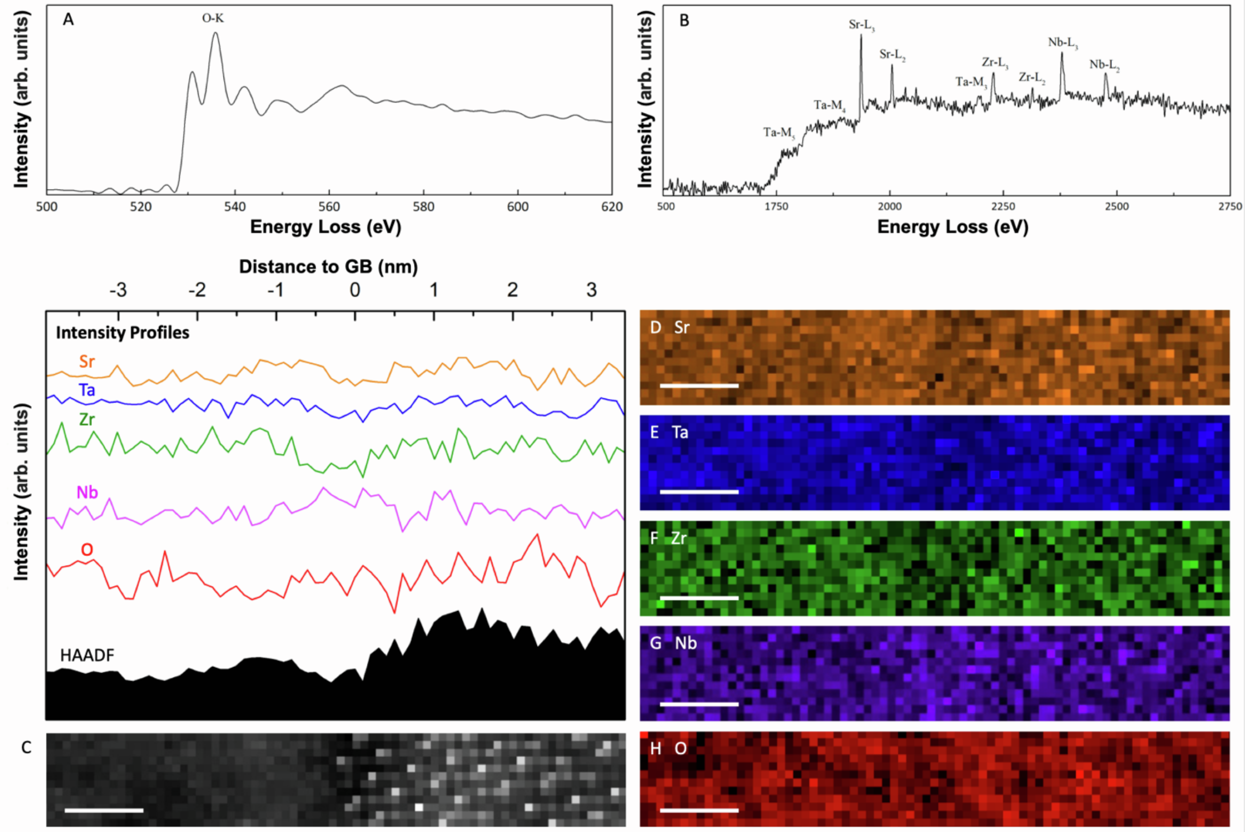

Figure S25. Core-loss EELS data of a LSTNZS (*y* = 9/16) general GB
Integrated EELS spectra of (A) O-K and (B) Sr-$L_{2,3}$, Ta-$M_{2,3}$, Ta-$M_{4,5}$, Nb-$L_{2,3}$, and Zr-$L_{2,3}$ edges for the general grain boundary shown in (C). (C) Atomic-resolution HAADF-STEM image of a general grain boundary. Elemental maps of (D) Sr, (E) Ta, (F) Zr, (G) Nb, and (H) O. All scale bars are 1 nm. Intensity profiles of (C) – (H) are shown above (C).

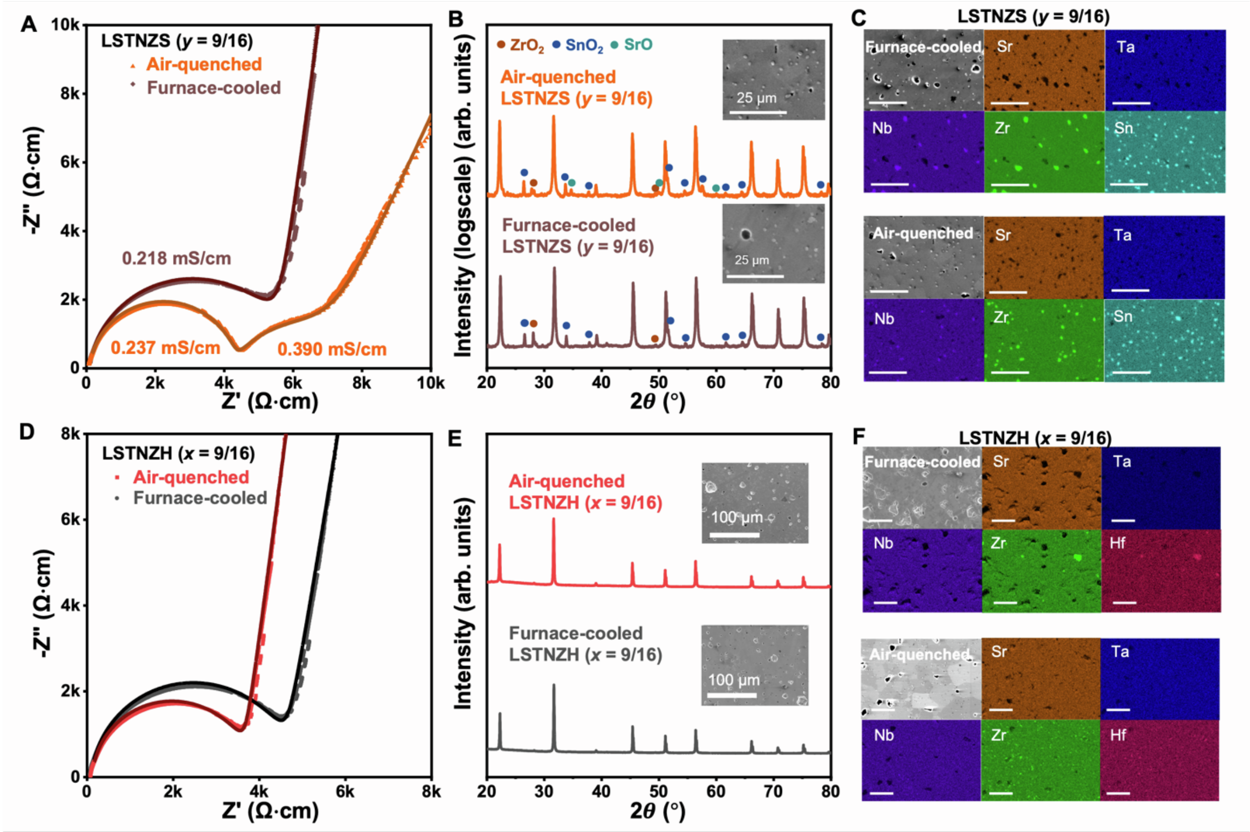

Figure S26. The Nyquist plots, XRD patterns, and SEM-EDS maps of the furnace-cooled and air-quenched LSTNZS (*y* = 9/16) and LSTNZH (*x* = 9/16)

(A)-(C) Impedance curves, phase stability and elemental distribution of furnace-cooled and air-quenched LSTNZS (*y* = 9/16). (D)-(F) The same set of data for the furnace-cooled and air-quenched LSTNZH (*x* = 9/16).

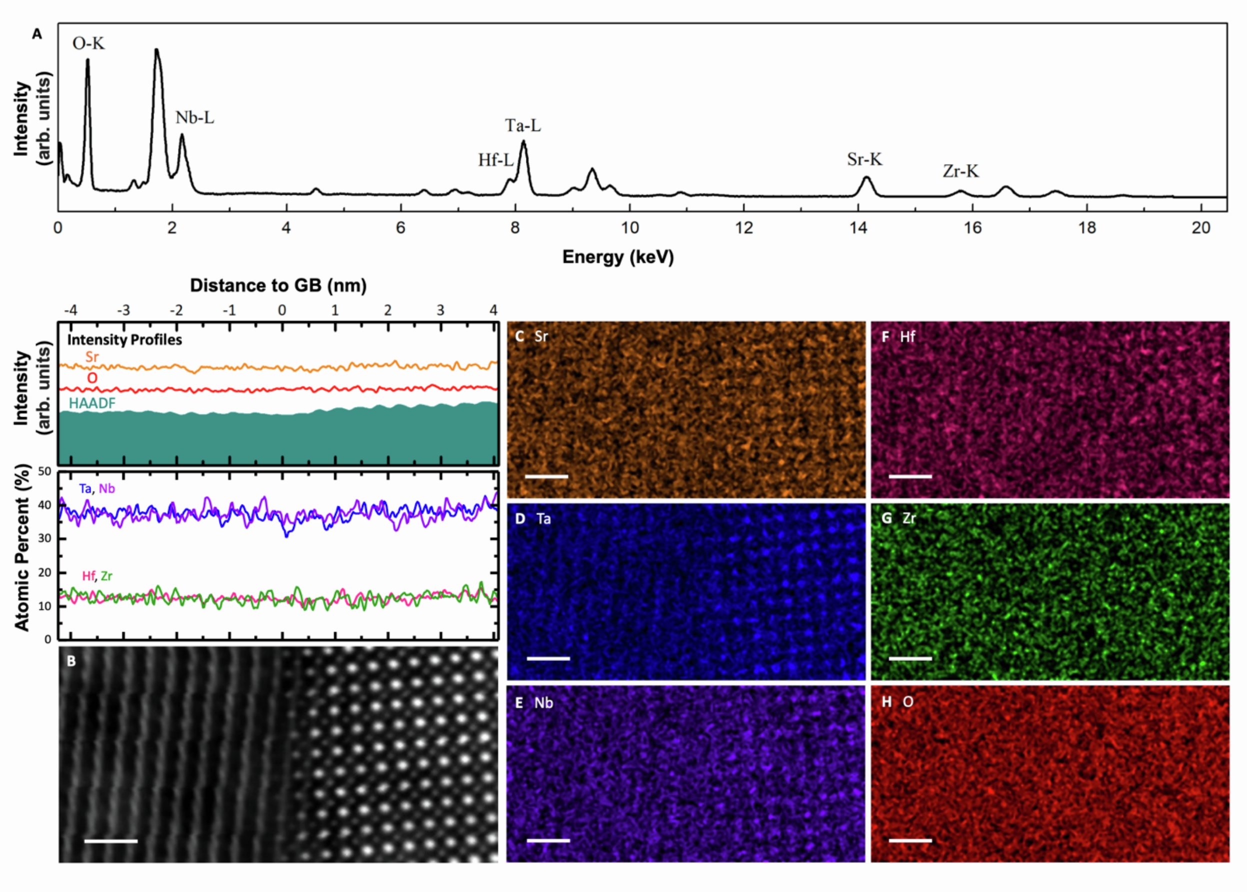

Figure S27. STEM-EDS data of furnace-cooled LSTNZH (*y* = 9/16) small-angle GB
(A) Integrated EDS spectrum for the small-angle grain boundary shown in (B). (B) HAADF-STEM image and elemental maps of (C) Sr, (D) Ta, (E) Nb, (F) Hf, (G) Zr, and (H) O collected at the furnace-cooled LSTNZH (*y* = 9/16) small-angle GB. Scale bars are 1 nm.

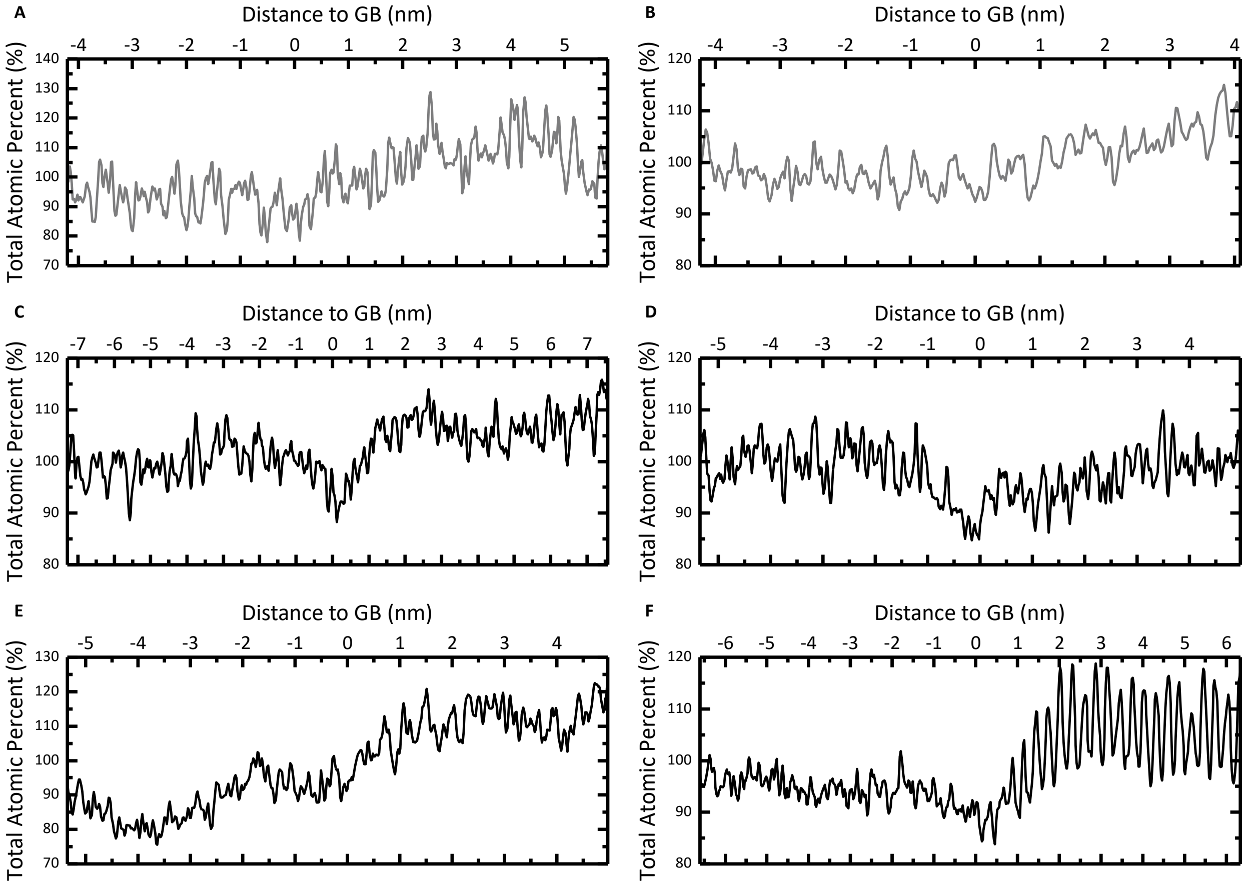

Figure S28. More B-site vacancies observed in the GBs of air-quenched LSTNZH (*x* = 9/16) than in those of furnace-cooled LSTNZH (*x* = 9/16)

Total B-site atomic percent plotted against distance to GB for furnace-cooled LSTNZH (*x* = 9/16): (A) General GB and (B) small-angle GB. The individual B-site elemental atomic percentages that sum up to the total shown in (A) and (B) are displayed above Figure 6C and Figure S27B, respectively. Total B-site atomic percent plotted against distance to GB for air-quenched LSTNZH *(x* = 9/16) (C–F) General GBs. The individual B-site elemental atomic percentages that sum up to the total shown in (C), (D), (E), and (F) are displayed above Figure 6E, Figure S30C, Figure S31C, and Figure S31E, respectively.

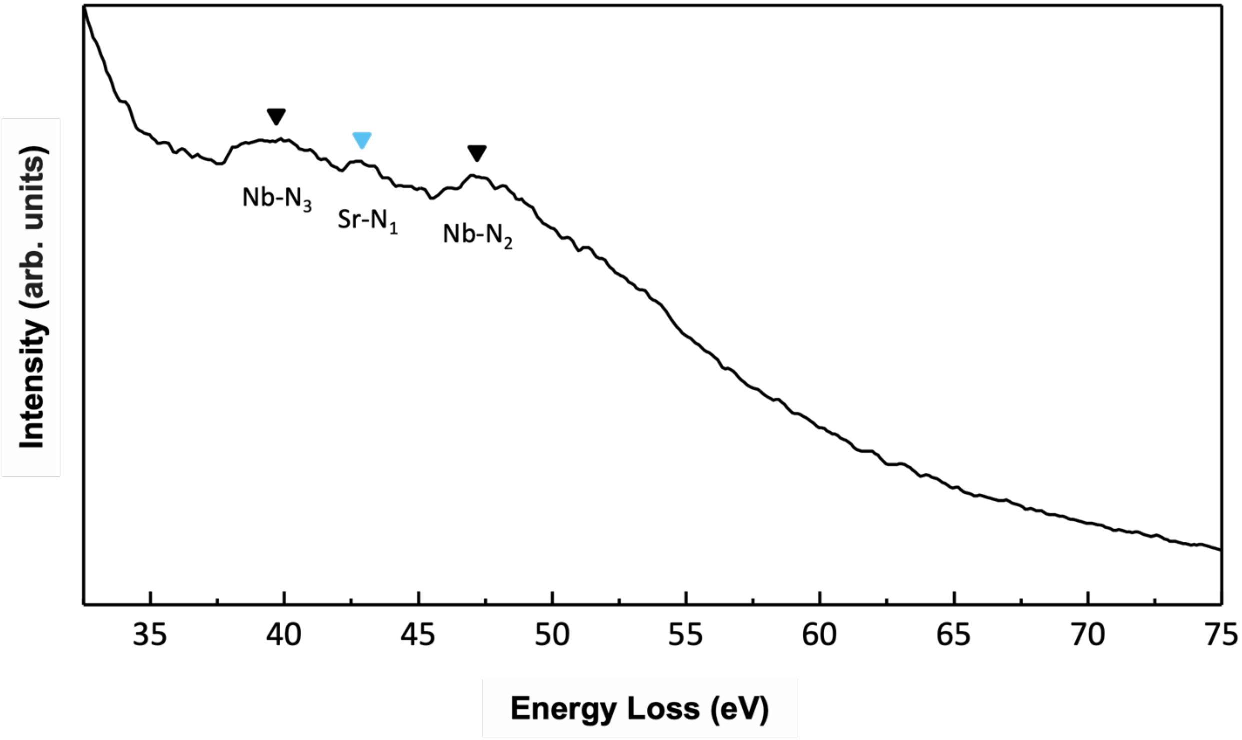

Figure S29. Distinct Li-K edge of the LSTNZH (*x* = 9/16) is not observed in the EELS spectrum Raw integrated EELS spectrum collected at the low energy loss regime. Edge corresponding to each peak is assigned. Distinct Li-K edge of LSTNZH (*x* = 9/16) is not observed due to its close proximity to the Nb-$N_{2,3}$ edge, the low Li^+ content in LSTNZH (*x* = 9/16), and the poor scattering power of Li (*Z* = 3).

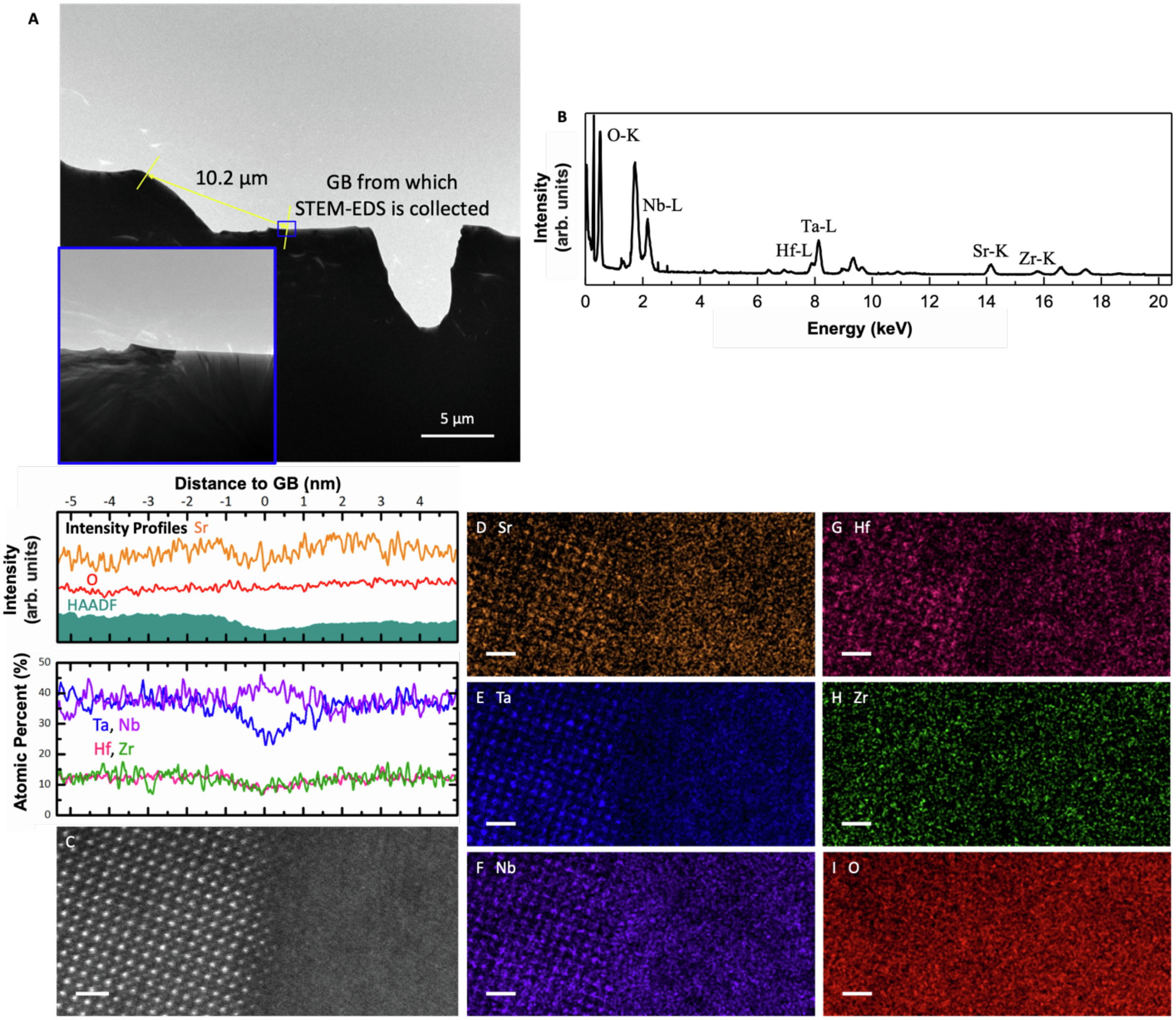

Figure S30. STEM-EDS data of air-quenched LSTNZH (*x* = 9/16) general GBs formed by average sized abutting grain

(A) Shadow image of general GB formed by grain that have average grain size. Inset shows high magnification shadow images of the GB. (B) Integrated EDS spectrum for the GB shown in (A). (C) HAADF-STEM image and elemental maps of (D) Sr, (E) Ta, (F) Nb, (G) Hf, (H) Zr, and (I) O collected at the general GB boxed in (A). Scale bars are 1 nm.

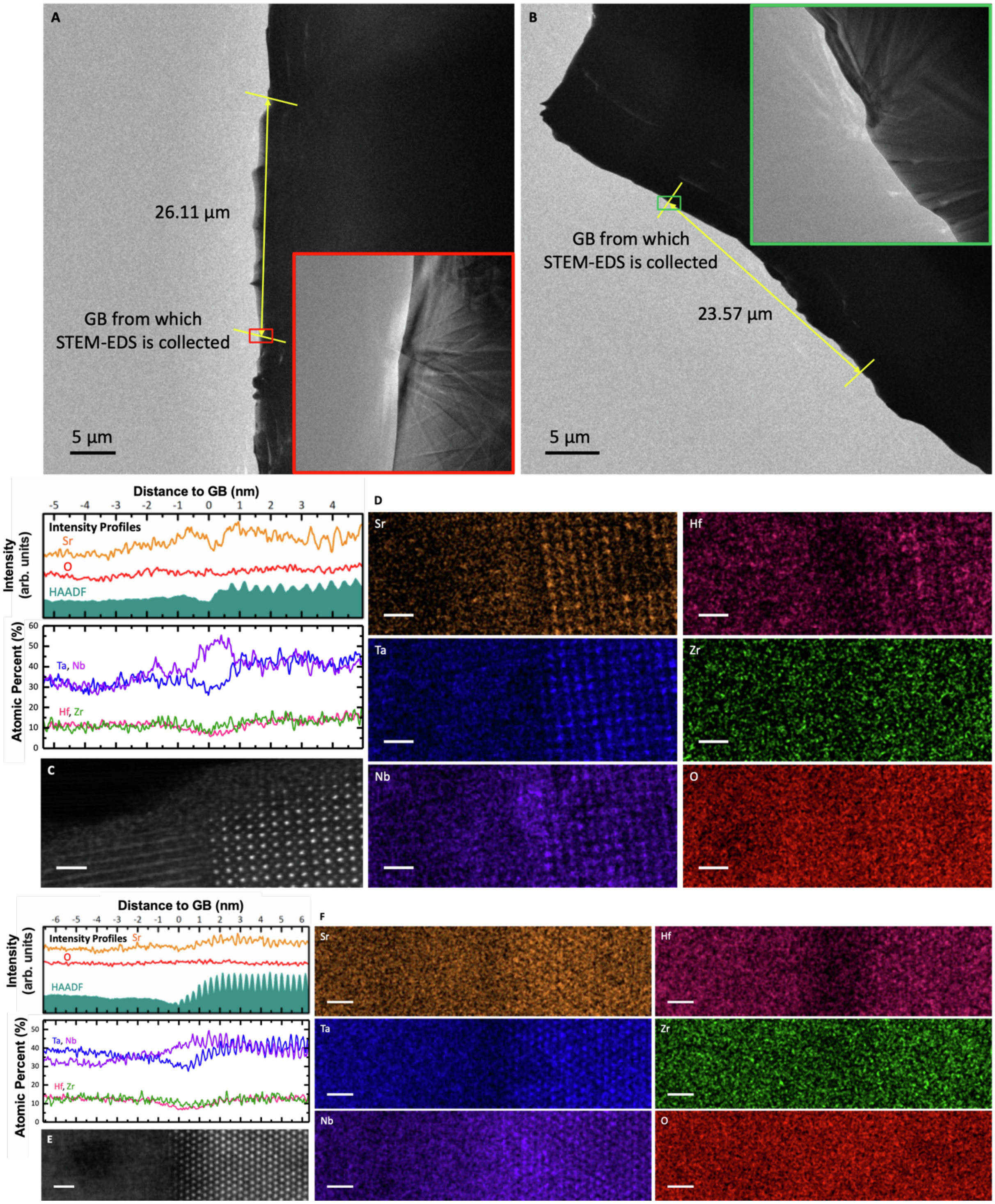

Figure S31. STEM-EDS data of air-quenched LSTNZH ($x = 9/16$) general GBs formed by large abutting grains

(A) and (B) Shadow images of general GBs formed by grains that have above average grain sizes. Insets show high magnification shadow images of the GBs. (C), (E) HAADF-STEM image and (D), (F) elemental maps of Sr, Ta, Nb, Hf, Zr, and O collected at the general GBs boxed in (A) and (B), respectively. Scale bars are 1 nm.

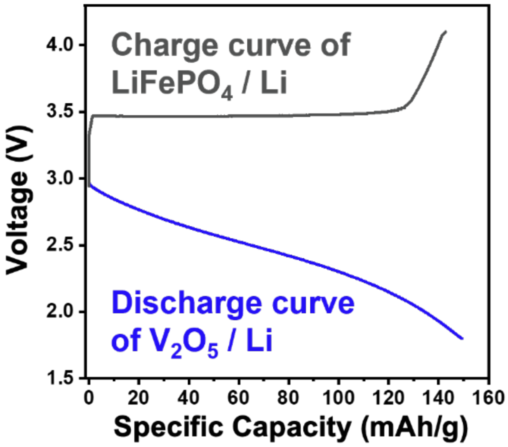

Figure S32. The voltage profiles of galvanostatic charge-discharge curves of prelithiated V_2O_5 and $LiFePO_4$ half-cells

The 1st cycle charge curve of $LiFePO_4$ | Li half-cell (grey) and the 1st cycle discharge curve of prelithiated V_2O_5 | Li half-cell (blue) are used to evaluate the working potential of anode (1.8 V - 3.0 V for prelithiated V_2O_5) and cathode (3.0 V - 4.1 V for $LiFePO_4$).

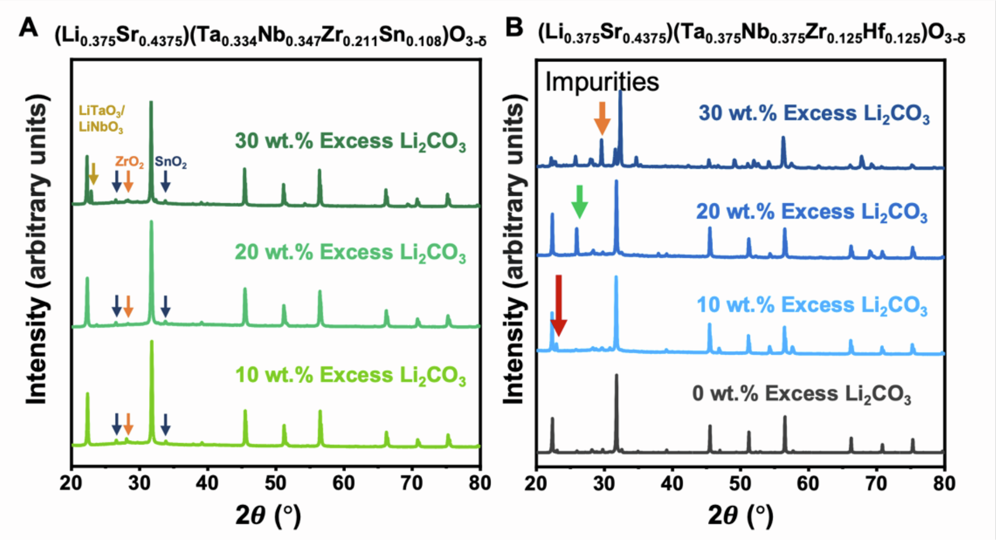

Figure S33. The phase stability test on excess Li_2CO_3 precursor amount added in LSTNZS (*y* = 9/16) and LSTNZH (*x* = 9/16)

(A) The influence of the amount of excess Li_2CO_3 precursor on the phase stability of LSTNZS (*y* = 9/16). 10 wt. % excess Li_2CO_3 was chosen in LSTNZS. (B) The same test on LSTNZH (*x* = 9/16), which shows the best stability when no excess Li_2CO_3 was added.

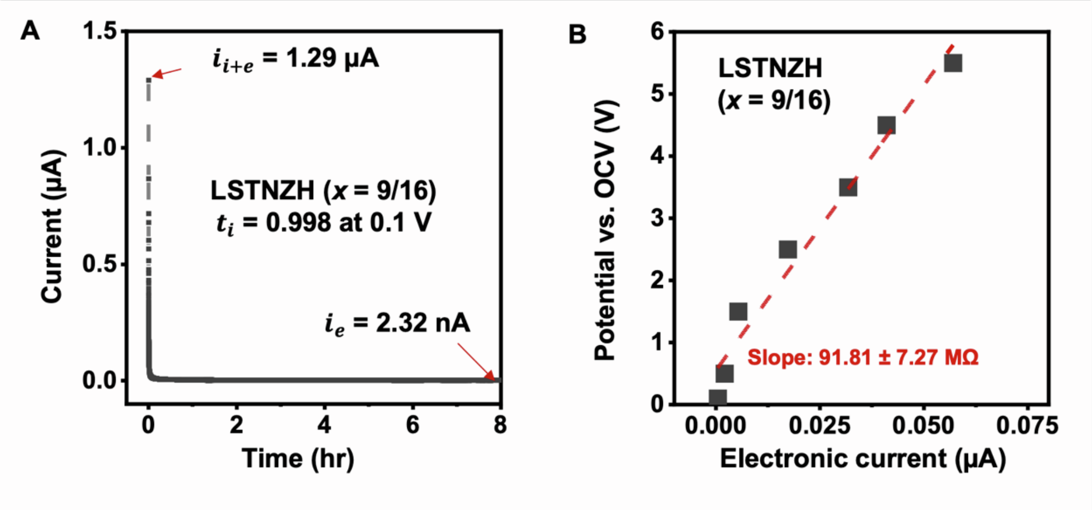

Figure S34. DC polarization measurements of LSTNZH (*x* = 9/16)
(A) The DC polarization measurement of LSTNZH (*x* = 9/16) at a constant applied voltage of 0.1 V for 8 hours. (B) The electronic current values after applying various constant potentials for 12 hours. The fitted slope represents the ohmic resistance of LSTNZH (*x* = 9/16).

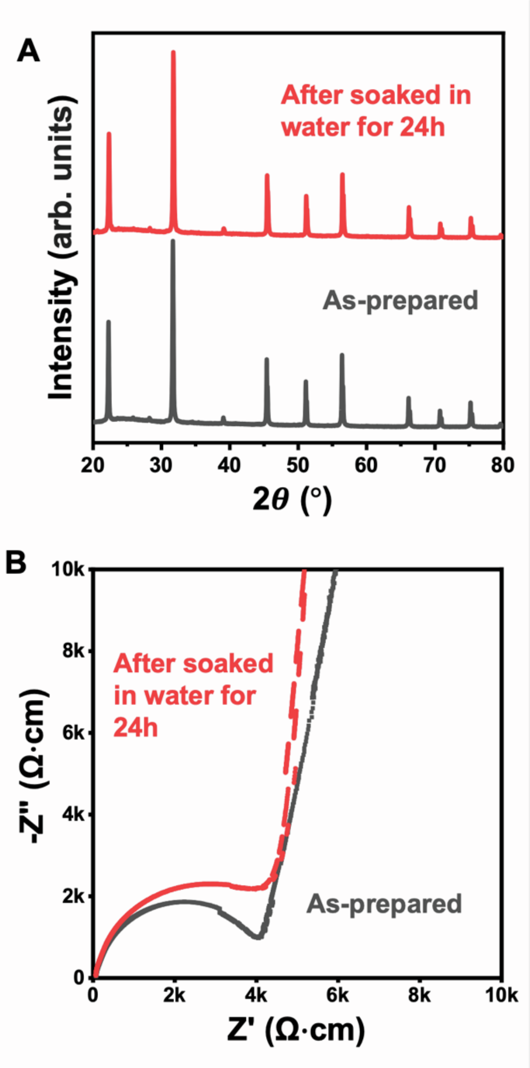

Figure S35. Moisture test on the phase stability of LSTNZH (*x* = 9/16)

(A) The XRD patterns of LSTNZH (*x* = 9/16) before and after soaked in DI water for 24h. No secondary phases/surface impurities are observed after moisture test. (B) Impedance curves of samples before and after moisture test. The fitted ionic conductivity is 0.23 mS/cm after moisture test (*vs.* 0.255 mS/cm before the test).

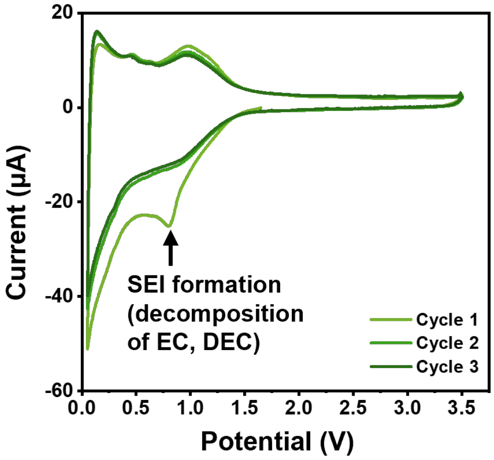

Figure S36. The cyclic voltammetry profile of $(Li_{0.375}Sr_{0.4375})(Ta_{0.334}Nb_{0.347}Zr_{0.211}Sn_{0.108})O_{3-\delta}$ using scan rates of 0.1 mV/s.

In the first cycle, the reduction of FEC occurs at a potential of 1.3 V (vs. Li/Li^+). Subsequently, the cathodic peak at 0.8 V (vs. Li/Li^+) indicates the formation of solid electrolyte interphase (SEI) due to the reduction of organic solvent (EC, DEC) used in the liquid electrolyte.[S2] From the second to the third cycles, the redox reactions are reversible without the influence of SEI reactions.

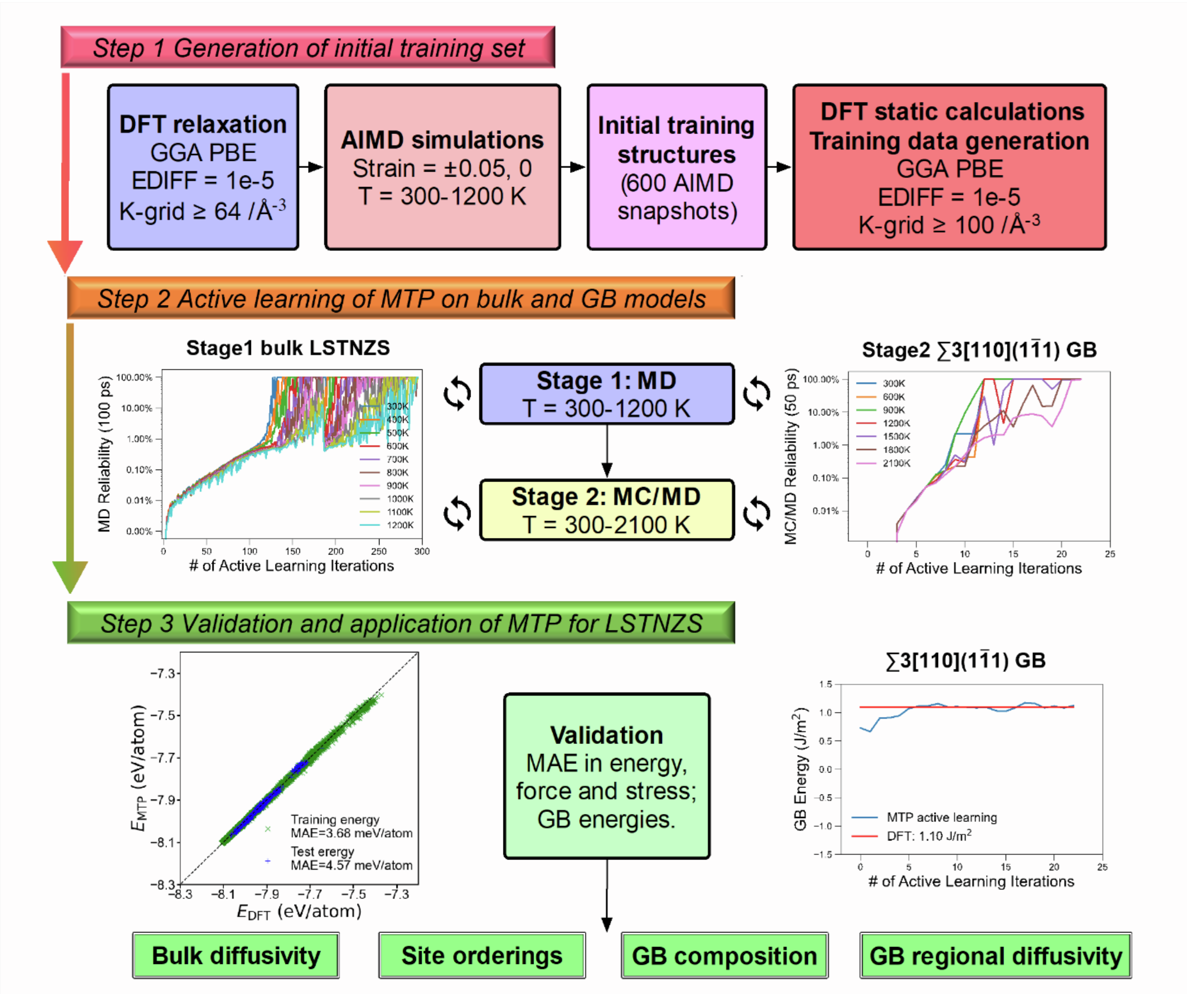

Figure S37. Flowchart for the training and validation of MTP to study bulk and GB models of LSTNZS (*y* = 9/16)

The flowchart describes three steps of training and validation of MTP, including i) generation of initial training set, ii) active learning of MTP on the bulk and GB models, and iii) validation and application of MTP to study bulk and GB models of LSTNZS (*y* = 9/16).

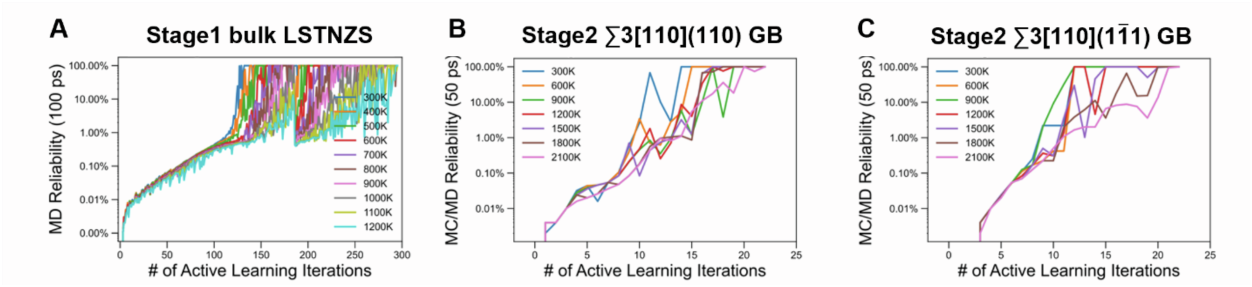

Figure S38. The iterative improvement of MTP with two stages of active learning
(A-C) MD simulations (A) up to 1200 K with the bulk structure and MC/MD simulations up to 2100 K with the (B) simple twist Σ3[110](110) and (C) symmetric tilt Σ3[110](1$\bar{1}$1) GB models.

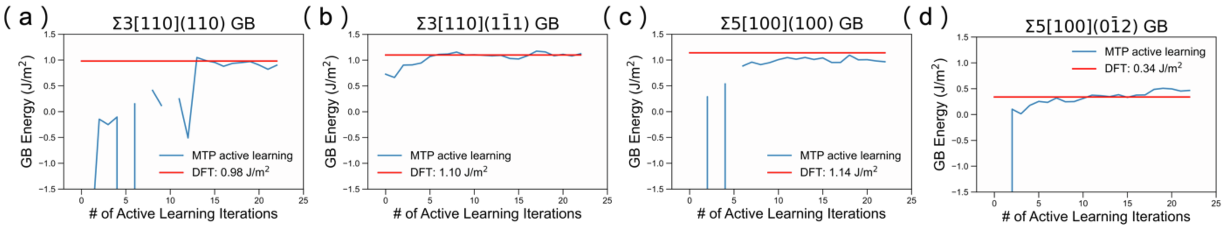

Figure S39. The convergence of predicted GB energies by MTP with respect to DFT references throughout the second stage of active learning

Beside the (A) simple twist Σ3[110](110) and (B) symmetric tilt Σ3[110](1$\bar{1}$1) GB orientations included in the training set, another two GB orientations out of the training set, i.e., (C) simple twist Σ5[100](100) and (D) symmetric tilt Σ5[100](0$\bar{1}$2) were also considered to verify the ability of our optimized MTP to accurately simulate GB orientations out of the training set.

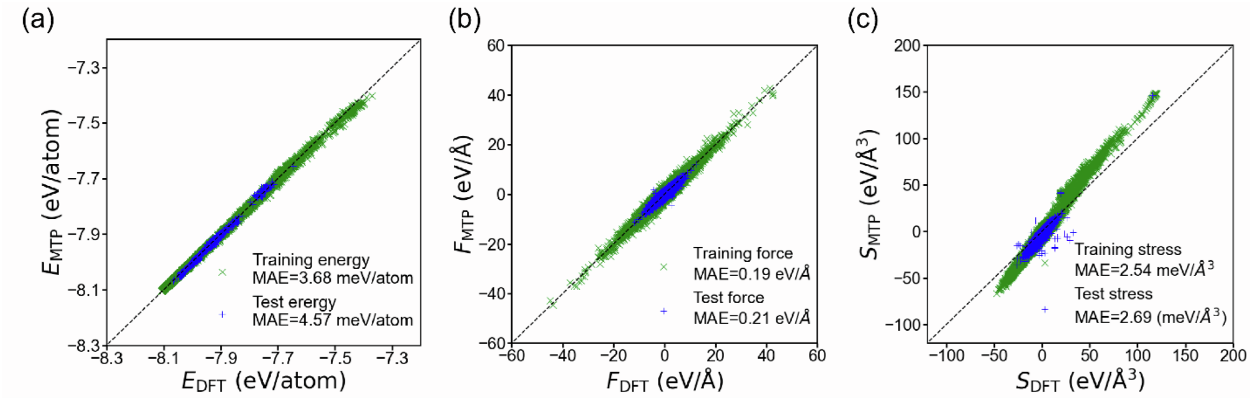

Figure S40. The distribution of training and test errors of MTP energies, forces, and stresses with respect to DFT

The training set contains 600 AIMD snapshots and 4133 active learning snapshots. The test set contains 880 structures collected from 1 ns MD and MC/MD simulations on the two GB models used in active learning from 300 to 1200 K with 300 K intervals and from 298 to 1573 K with 425 K intervals, respectively. At each temperature, 110 structures were collected.

Table S1. Summary of the physical properties of selected CCPO LSTNZS series and LSTZ presented in this work

Group	Nominal composition with Sample ID	Nominal V_{sr}'' fraction	Li/Sr molar ratio	Lattice constant (Å)	σ_{bulk} (mS/cm)	σ_{total} (mS/cm)	Secondary phases
LSTZ	$(Li_{0.375}Sr_{0.4375})(Ta_{0.75}Zr_{0.25})O_{3-\delta}$, **LSTZ**	0.1875	0.86	3.994	0.094	0.094	ZrO_2, $LiTaO_3$, $LiNbO_3$, $Sr_{2.83}Ta_5O_{15}$
LSTNZS "*x* series"	$(Li_{0.3333}Sr_{0.5})(Ta_{0.333}Nb_{0.333}Zr_{0.167}Sn_{0.167})O_{3-\delta}$, **LSTNZS (*x* = 8/16)**	0.1667	0.52	3.997	0.110	0.053	SnO_2
	$(Li_{0.375}Sr_{0.4375})(Ta_{0.375}Nb_{0.375}Zr_{0.125}Sn_{0.125})O_{3-\delta}$, **LSTNZS (*x* = 9/16)**	0.1875	0.67	–	–	–	SnO_2, ZrO_2 , Ta_2O_5, $Sr_{2.83}Ta_5O_{15}$
	$(Li_{0.4167}Sr_{0.375})(Ta_{0.417}Nb_{0.417}Zr_{0.083}Sn_{0.083})O_{3-\delta}$, **LSTNZS (*x* = 10/16)**	0.2083	0.86	–	–	–	SnO_2, ZrO_2 , $LiTaO_3$, $LiNbO_3$, Ta_2O_5, $Sr_{2.83}Ta_5O_{15}$
LSTNZS "*y* series"	$(Li_{0.258}Sr_{0.613})(Ta_{0.334}Nb_{0.347}Zr_{0.211}Sn_{0.108})O_{3-\delta}$, **LSTNZS (*y* = 0.387)**	0.129	0.42	4.002	0.004	0.004	$SrTa_4O_{11}$
	$(Li_{0.332}Sr_{0.5})(Ta_{0.334}Nb_{0.347}Zr_{0.211}Sn_{0.108})O_{3-\delta}$, **LSTNZS (*y* = 0.5)**	0.168	0.67	3.991	0.118	0.118	SnO_2, ZrO_2
	$(Li_{0.375}Sr_{0.4375})(Ta_{0.334}Nb_{0.347}Zr_{0.211}Sn_{0.108})O_{3-\delta}$, **LSTNZS (*y* = 9/16 or 0.5625)**	0.1875	0.86	3.992	0.218	0.218	SnO_2
	$(Li_{0.4}Sr_{0.4})(Ta_{0.334}Nb_{0.347}Zr_{0.211}Sn_{0.108})O_{3-\delta}$, **LSTNZS (*y* = 0.6)**	0.2	1.00	3.991	0.140	0.038	SnO_2, ZrO_2, $LiTaO_3$, $LiNbO_3$
LSTNZS Sn/Zr "*w* series"	$(Li_{0.375}Sr_{0.4375})(Ta_{0.334}Nb_{0.347}Zr_{0.119}Sn_{0.2})O_{3-\delta}$, **LSTNZS (*w* = 0.2)**	0.1875	0.86	3.988	0.103	0.034	SnO_2
	$(Li_{0.375}Sr_{0.4375})(Ta_{0.334}Nb_{0.347}Zr_{0.169}Sn_{0.15})O_{3-\delta}$, **LSTNZS (*w* = 0.15)**	0.1875	0.86	3.990	0.220	0.114	SnO_2
	$(Li_{0.375}Sr_{0.4375})(Ta_{0.334}Nb_{0.347}Zr_{0.211}Sn_{0.108})O_{3-\delta}$, **LSTNZS (*w* = 0.108), equivalent to LSTNZS (*y* = 9/16 or 0.5625)**	0.1875	0.86	3.992	0.218	0.218	SnO_2
	$(Li_{0.375}Sr_{0.4375})(Ta_{0.334}Nb_{0.347}Zr_{0.265}Sn_{0.054})O_{3-\delta}$, **LSTNZS (*w* = 0.054)**	0.1875	0.86	3.994	0.169	0.169	ZrO_2
	$(Li_{0.375}Sr_{0.4375})(Ta_{0.334}Nb_{0.347}Zr_{0.319})O_{3-\delta}$, **LSTNZS (*w* = 0)**	0.1875	0.86	4.000	0.089	0.089	ZrO_2

Table S2. Summary of physical properties of selected CCPO LSTNZH series presented in this work

Group	Nominal composition with Sample ID	Nominal V_{sr}'' fraction	Li/Sr molar ratio	Lattice constant (Å)	σ_{bulk} (mS/cm)	σ_{total} (mS/cm)	Secondary phases
LSTNZH “*x* series”	$(Li_{0.2917}Sr_{0.5625})(Ta_{0.292}Nb_{0.292}Zr_{0.208}Hf_{0.208})O_{3-\delta}$, **LSTNZH (*x* = 7/16)**	0.1458	0.52	4.014	0.005	0.005	ZrO_2
	$(Li_{0.3333}Sr_{0.5})(Ta_{0.333}Nb_{0.333}Zr_{0.167}Hf_{0.167})O_{3-\delta}$, **LSTNZH (*x* = 8/16)**	0.1667	0.67	4.004	0.032	0.032	ZrO_2
	$(Li_{0.375}Sr_{0.4375})(Ta_{0.375}Nb_{0.375}Zr_{0.125}Hf_{0.125})O_{3-\delta}$, **LSTNZH (*x* = 9/16)**	0.1875	0.86	3.987	0.151	0.151	No
	$(Li_{0.4167}Sr_{0.375})(Ta_{0.417}Nb_{0.417}Zr_{0.083}Hf_{0.083})O_{3-\delta}$, **LSTNZH (*x* = 10/16)**	0.2083	1.11	–	0.0003	0.0003	$LiTaO_3$, $LiNbO_3$, ZrO_2 , Ta_2O_5
	$(Li_{0.4583}Sr_{0.3125})(Ta_{0.458}Nb_{0.458}Zr_{0.042}Hf_{0.042})O_{3-\delta}$, **LSTNZH (*x* = 11/16)**	0.2292	1.47	–	0.0001	0.0001	$LiTaO_3$, $LiNbO_3$, ZrO_2 , Ta_2O_5
LSTNZH Ta/Nb “*z* series”	$(Li_{0.375}Sr_{0.4375})(Ta_{0.75}Zr_{0.125}Hf_{0.125})O_{3-\delta}$, **LSTNZH (*z* = 0)**	0.1875	0.86	3.994	0.229	0.111	No
	$(Li_{0.375}Sr_{0.4375})(Ta_{0.675}Nb_{0.075}Zr_{0.125}Hf_{0.125})O_{3-\delta}$, **LSTNZH (*z* = 0.075)**	0.1875	0.86	3.993	0.341	0.197	No
	$(Li_{0.375}Sr_{0.4375})(Ta_{0.6}Nb_{0.15}Zr_{0.125}Hf_{0.125})O_{3-\delta}$, **LSTNZH (*z* = 0.15)**	0.1875	0.86	3.993	0.311	0.214	No
	$(Li_{0.375}Sr_{0.4375})(Ta_{0.525}Nb_{0.225}Zr_{0.125}Hf_{0.125})O_{3-\delta}$, **LSTNZH (*z* = 0.225)**	0.1875	0.86	3.995	0.262	0.178	No
	$(Li_{0.375}Sr_{0.4375})(Ta_{0.45}Nb_{0.3}Zr_{0.125}Hf_{0.125})O_{3-\delta}$, **LSTNZH (*z* = 0.3)**	0.1875	0.86	3.993	0.272	0.204	No
	$(Li_{0.375}Sr_{0.4375})(Ta_{0.375}Nb_{0.375}Zr_{0.125}Hf_{0.125})O_{3-\delta}$, **LSTNZH (*z* = 0.375), equivalent to LSTNZH (*x* = 9/16)**	0.1875	0.86	3.987	0.151	0.151	No
	$(Li_{0.375}Sr_{0.4375})(Ta_{0.3}Nb_{0.45}Zr_{0.125}Hf_{0.125})O_{3-\delta}$, **LSTNZH (*z* = 0.45)**	0.1875	0.86	3.980	0.206	0.131	ZrO_2
	$(Li_{0.375}Sr_{0.4375})(Ta_{0.225}Nb_{0.525}Zr_{0.125}Hf_{0.125})O_{3-\delta}$, **LSTNZH (*z* = 0.525)**	0.1875	0.86	3.993	0.150	0.068	$Sr_6Nb_{10}O_{30}$
	$(Li_{0.375}Sr_{0.4375})(Ta_{0.15}Nb_{0.6}Zr_{0.125}Hf_{0.125})O_{3-\delta}$, **LSTNZH (*z* = 0.6)**	0.1875	0.86	3.985	0.048	0.009	$Sr_6Nb_{10}O_{30}$

Table S3. Summary of the measured conductivities of the furnace-cooled vs. air-quenched LSTNZH (*x* = 9/16).

Nominal composition with Sample ID	σ_{bulk} (mS/cm)	σ_{gb} (mS/cm)	σ_{gb}^{spec} (mS/cm)	σ_{total} (mS/cm)
$(Li_{0.375}Sr_{0.4375})(Ta_{0.375}Nb_{0.375}Zr_{0.125}Hf_{0.125})O_{3-\delta}$, **LSTNZH (*x* = 9/16) furnace-cooled**	0.357	0.335	7.67×10^{-4}	0.173
$(Li_{0.375}Sr_{0.4375})(Ta_{0.375}Nb_{0.375}Zr_{0.125}Hf_{0.125})O_{3-\delta}$, **LSTNZH (*x* = 9/16) air-quenched**	0.450	0.592	1.36×10^{-3}	0.256

Table S4. Summary of valence and Shannon ionic radii of selected B-site elements[S3]

Element	Valence	Ionic radius (Å)	Coordination number
Ta	5	0.64	6
Nb	5	0.64	6
Zr	4	0.72	6
Sn	4	0.69	6
Hf	4	0.71	6

Table S5. The SEM-EDS quantification of normalized cation ratios of the primary phase region in $(Li_{0.375}Sr_{0.4375})(Ta_{0.25}Nb_{0.25}Zr_{0.25}Sn_{0.25})O_{3-\delta}$ (LSTNZS-iteration1) and $(Li_{0.375}Sr_{0.4375})(Ta_{0.292}Nb_{0.292}Zr_{0.252}Sn_{0.163})O_{3-\delta}$ (LSTNZS-iteration2) in a "natural selection" search

Sample ID	Composition	Areal EDS	Sr-Lα1	Nb-Lα1	Ta-Lα1	Zr-Lα1	Sn-Lα1
LSTNZS-iteration1	$(Li_{0.375}Sr_{0.4375})(Ta_{0.25}Nb_{0.25}Zr_{0.25}Sn_{0.25})O_{3-\delta}$	Atomic %	38.6	17.8	18.1	15.5	10
		Normalized Cation Ratio	0.629	0.290	0.295	0.252	0.163
LSTNZS-iteration2	$(Li_{0.375}Sr_{0.4375})(Ta_{0.292}Nb_{0.292}Zr_{0.252}Sn_{0.163})O_{3-\delta}$	Atomic %	38	21.5	20.7	13.1	6.7
		Normalized Cation Ratio	0.613	0.347	0.334	0.211	0.108

Table S6: The compositions and relevant physical descriptors of Nb and Sn co-doped LSTZ and LSTNZS synthesized during composition optimization

Sample ID	Nominal composition	Averaged valency of A- and B-site cations	Molar ratio of 5B/4B cations
LSTZ	$(Li_{0.375}Sr_{0.4375})(Ta_{0.75}Zr_{0.25})O_{3-\delta}$	6	3
LSTZ-NS-1	$(Li_{0.375}Sr_{0.4375})(Ta_{0.725}Nb_{0.025}Zr_{0.225}Sn_{0.025})O_{3-\delta}$	6	3
LSTZ-NS-2	$(Li_{0.375}Sr_{0.4375})(Ta_{0.7}Nb_{0.05}Zr_{0.2}Sn_{0.05})O_{3-\delta}$	6	3
LSTNZS-iteration1	$(Li_{0.375}Sr_{0.4375})(Ta_{0.25}Nb_{0.25}Zr_{0.25}Sn_{0.25})O_{3-\delta}$	5.75	1
LSTNZS-iteration2	$(Li_{0.375}Sr_{0.4375})(Ta_{0.292}Nb_{0.292}Zr_{0.253}Sn_{0.163})O_{3-\delta}$	5.83	1.404
LSTNZS (*y* = 9/16 or 0.5625)	$(Li_{0.375}Sr_{0.4375})(Ta_{0.334}Nb_{0.347}Zr_{0.211}Sn_{0.108})O_{3-\delta}$	5.931	2.1348

Table S7. The Rietveld refinement results and refined phase fractions for LSTNZS (*y* series) and LSTNZH (*x* series, excluding *x* = 9/16 since it contains close to 0% secondary phase)

Sample ID	Weighted *R*-factor	Refined phase percentage (%)				
		Primary	SnO_2	ZrO_2	$SrTa_4O_{11}$	Li(Ta, Nb)O_3
LSTNZS (*y* = 0.6)	14.56%	96.37	2.117	1.092		0.417
LSTNZS (*y* = 0.5625)	13.99%	93.45	5.872	0.675		
LSTNZS (*y* = 0.5)	9.767%	98.05	0.957	0.990		
LSTNZS (*y* = 0.387)	11.73%	97.10			2.899	
LSTNZH (*x* = 7/16)	18.42%	96.26		3.741		
LSTNZH (*x* = 8/16)	7.86%	96.45		3.545		

Table S8. The summary of activation energies at 300 – 700K and 700 – 1000K, and Li-ion diffusivities of the bulk and two GB models at 300K for LSTNZS (*y* = 9/16)

Structure	Activation Energy (eV)		$D_{\mathrm{Li,\ 300K}}$ (10^{-9} cm^2/s)
	300 - 700 K	700 - 1000K	
Bulk	0.33	0.20	7.92
$\sum3[110](110)$	0.32	0.30	3.22
$\sum5[100](0\bar{1}2)$	0.33	0.23	4.59

Table S9. Interplanar distance ($d_{\mathrm{interplanar}}$), GB thickness (d_{GB}), cell dimensions (*x*, *y* and *z*; *z* is perpendicular to GB planes) and total number of atoms (N_{total}) of GB models of LSTNZS (*y* = 9/16)

GB orientations	$d_{\mathrm{interplanar}}$* (Å)	d_{GB}* (Å)	GB dimensions* (Å)			N_{total}
			x	*y*	*z*	
$\Sigma3[110](110)$	2.82	5.65	41.48	39.11	90.33	11,200
$\Sigma3[110](1\bar{1}1)$	2.30	9.22	33.87	45.16	82.97	8,400
$\Sigma5[100](100)$	3.99	7.98	53.56	35.70	95.80	14,000
$\Sigma5[100](0\bar{1}2)$	1.79	7.14	47.90	35.70	107.11	14,000

*The d_{GB} was defined to be either two or four times the $d_{\mathrm{interplanar}}$ of GB planes in the lattice with a general requirement of d_{GB} > 5 Å. The $d_{\mathrm{interplanar}}$, d_{GB}, and GB dimensions are values of the unrelaxed GB models, which change with temperature. The GB regions for regional composition and diffusivity analysis were defined with fractional z coordinates to make the GB regions consistent at different temperatures.

Note S1. Calculations of the bulk, grain boundary (GB), total conductivities, and specific GB ionic conductivity

In a brick layer model for polycrystals proposed by Van Dijk and Burggraaf,[S4] the grains are assumed to be cube-shaped with grain size (*d*), separated by flat grain boundary layers with thickness (δ_{gb}). The bulk ionic conductivity (σ_{bulk}) and the macroscopic grain boundary (GB) ionic conductivity (σ_{gb}) are calculated as

$$\sigma_{bulk} = \frac{L}{R_{bulk} \cdot A} \qquad \text{(Equation S1)}$$

and

$$\sigma_{gb} = \frac{L}{R_{gb} \cdot A}, \qquad \text{(Equation S2)}$$

where R_{bulk} and R_{gb} are bulk and GB resistance using the equivalent circuit model shown in Figure 6A. L is the sample thickness and A is the sample cross-section area. Considering R_{bulk} and R_{gb} in series, the total ionic conductivity (σ_{total}) is calculated as:

$$\sigma_{total} = \frac{\sigma_{bulk} \cdot \sigma_{gb}}{\sigma_{bulk} + \sigma_{gb}}. \qquad \text{(Equation S3)}$$

For the microscopic estimation, the specific (*i.e.*, true) GB ionic conductivity is approximated to be:

$$\sigma_{gb}^{spec} = \sigma_{gb} \frac{\delta_{gb}}{d}. \qquad \text{(Equation S4)}$$

If the dielectric constant is approximately the same for the GBs and for the bulk,

$$\frac{\delta_{gb}}{d} = \frac{C_{bulk}}{C_{gb}}, \qquad \text{(Equation S5)}$$

where C_{bulk} and C_{gb} are bulk and GB capacitance. Therefore, combining Equations (S2), (S4) and (S5), the specific GB conductivity is:

$$\sigma_{gb}^{spec} = \frac{L}{R_{gb} \cdot A} \frac{C_{bulk}}{C_{gb}}. \qquad \text{(Equation S6)}$$

Given the equivalent circuit model shown in Figure 6A, the constant phase element (CPE) is employed to describe the non-ideality of semicircles in the Nyquist plot. The CPE is composed of the pseudo capacitance (CPE-T), denoted as Q and the non-ideality term (CPE-P) between 0-1, denoted as n. Therefore, the bulk and grain boundary capacitance are expressed as:

$$C_{bulk} = R_{bulk}^{\left(\frac{1}{n_{bulk}} - 1\right)} Q_{bulk}^{\frac{1}{n_{bulk}}}; \; C_{gb} = R_{gb}^{\left(\frac{1}{n_{gb}} - 1\right)} Q_{gb}^{\left(\frac{1}{n_{gb}}\right)}. \qquad \text{(Equation S7)}$$

The specific GB conductivity values presented in Figure 1 was calculated using Equations (S6) and (S7) from the Nyquist plot fitting results in Figure 6A.

Note S2. The composition optimization strategy based on "natural selection"

To further improve the single-phase formability of LSTNZS systems, we initially synthesized $(Li_{0.375}Sr_{0.4375})(Ta_{0.25}Nb_{0.25}Zr_{0.25}Sn_{0.25})O_{3-\delta}$ with equimolar B-site cations (LSTNZS-iteration1), which shows less amount of secondary phases compared to LSTNZS (x = 9/16) (Figure S3). Next, we adopted the "natural selection" strategy explained in Figure S4 to synthesize composition of the primary phase obtained from SEM-EDS quantification results (Figure S5 and Table S5). Thus, the second composition $(Li_{0.375}Sr_{0.4375})(Ta_{0.292}Nb_{0.292}Zr_{0.252}Sn_{0.163})O_{3-\delta}$ (LSTNZS-iteration2) listed on Table S5 shows a non-equimolar B-site stoichiometry following the relative B-site cation ratio from LSTNZS-iteration1 primary phase.

Based on the SEM-EDS elemental quantification results on LSTNZS-iteration2, we designed the third composition as $(Li_{0.375}Sr_{0.4375})(Ta_{0.334}Nb_{0.347}Zr_{0.211}Sn_{0.108})O_{3-\delta}$, which exhibits less amount of secondary phases according to XRD patterns in Figure S6. The full list of samples in the composition optimization process is shown in Table S6. Finally, the optimal stoichiometry follows the formula $(Li_{(2/3)y}Sr_{1-y})(Ta_{0.334}Nb_{0.347}Zr_{0.211}Sn_{0.108})O_{3-\delta}$ (y series) with a fixed optimized B-site cation ratio.

Note S3. The calculation of excess energies of elements in LSTNZS (*y* = 9/16) and LSTZ

The excess energy of atom i with type j, $E_{excess}^{i,j}$ equals to the difference between its atomic energy, $E_{atomic}^{i,j}$, and the averaged atomic energy of all type j atoms, $E_{average}^{j}$, in the system:

$$E_{excess}^{i,j} = E_{atomic}^{i,j} - E_{average}^{j} . \qquad \text{(Equation S8)}$$

Excess energies have a much narrower range of distribution in LSTNZS (*y* = 9/16) than those in LSTZ. The narrowed distribution of excess energies for all elements in LSTNZS (*y* = 9/16) indicates lower energy differences between different atom sites of same elements. This effect is also reported in a recent work reported by Zeng *et al.* on high-entropy solid electrolytes,[S5] where the introduction of high-entropy mixing to transition metal sites lowered the energy difference between two different Li sites and induced lower diffusion barrier. However, in our LSTNZS (*y* = 9/16), we observed activation energy comparable with that of LSTZ. We attribute this to the fact that there is just one Li site in the perovskite structure; thus, the high-entropy effect has minimal effect on the activation energy. For future material designs with the aim of achieving lower diffusion barriers, this high-entropy concept can potentially be helpful for materials with different Li sites.

Note S4. Investigation of LSTNZS (*y* = 9/16) GB structures through STEM-EELS

Dark bands can be observed at both GBs in Figure S23A and S23B. Since the HAADF-STEM image intensity is dictated by the average atomic number of the elements present,[S6] this observation indicated compositional or mean density variation across the GB. To better understand the dark bands observed at GBs, STEM-EELS measurements were performed at the GB shown in Figure S23A. Because LSTNZS (*y* = 9/16) is beam sensitive, large step size (1 Å) was used to collect the data. Figure S25A and S25B shows the integrated EELS spectra of O-K edge and edges in the high energy loss regime (Sr-$L_{2,3}$, Ta-$M_{2,3}$, Ta-$M_{4,5}$, Nb-$L_{2,3}$, and Zr-$L_{2,3}$ edges), respectively. An atomic-resolution HAADF-STEM image of the GB, from which the EELS spectra were collected, is shown in Figure S25C. The GB again exhibited a significantly lower image intensity in comparison with the bulk. Figure S25D, S25E, S25F, S25G, and S25H display the atomic-resolution elemental maps of Sr, Ta, Zr, Nb, and O, respectively. The maps were generated using intensities from Sr-$L_{2,3}$, Ta-$M_{4,5}$, Zr-$L_{2,3}$, Nb-$L_{2,3}$, and O-K edges. As expected, the elemental maps (Figure S25D-G) show Sr atoms reside in the A-site positions, and Ta, Nb, and Zr atoms reside in the B-site positions. To analyze the correlation between HAADF image and the elemental maps, a plot of vertically integrated intensity profiles across the GB is shown above the HAADF image (Figure S25C). For the GB, the significant decrease in image intensity correlates well with the decrease in intensity of Sr, Ta, and Zr signals, though the decrease in Ta signal is much less than the other two. For the Sr signal, a decrease at the GB and an increase at the left and right sides adjacent to the GB is observed. This indicates that the GB exhibits elemental segregation, with Sr segregating out of the GB core and into sides of the abutting grains. For the B-site elemental signals, Ta and Zr decrease while Nb increases at the GB. This indicates that Nb is substituting Ta and Zr at the GB. Both Sr elemental segregation and Nb substitution suggest greater chemical disorder at the GBs of LSTNZS (*y* = 9/16), which can be a factor contributing to its low GB resistance. Finally, no decrease is observed in the intensity of O signals at the GB.

Although attempts were made to investigate the Li and Sn distribution at the GBs, low stoichiometric ratios of these two elements in $Li_{0.375}Sr_{0.4375}Ta_{0.334}Nb_{0.347}Zr_{0.211}Sn_{0.108}O_3$ made the Li-K and Sn-$M_{4,5}$ edges undetectable. Figure S24A shows the raw EELS spectrum of LSTNZS (*y* = 9/16). The two peaks at 39 and 47 eV are assigned to Nb-$N_{2,3}$ edge. Due to the broad shape of the Nb-N_2 edge, its proximity to the Li-K edge, the low Li^+ content in LSTNZS (*y* = 9/16), and the poor scattering power of Li (Z = 3), the Li-K edge is overwhelmed and cannot be detected. Previous studies have also reported distinct Li-K edges were difficult to identify in perovskite-type solid electrolytes, owing to their lower volume densities of Li^+ ions compared to other types of electrolytes.[S7,S8] Figure S24B shows that the Sn-M4,5 edge (expected at 485 eV) is also not detected in the EELS spectrum of LSTNZS (*y* = 9/16) due to the low concentration of Sn in composition.

Supplemental Experimental Procedures

TEM Sample Preparation and Moisture Sensitivity Test

TEM specimens were prepared by mechanical polishing. Moisture sensitivity of LSTNZH (x = 9/16) ceramics was first investigated in order to determine the material's compatibility with polishing fluid (either water or mineral oil). Moisture sensitivity test was done by submerging the pristine LSTNZH (x = 9/16) pellets in deionized water for 24 hours and then dried at 100 °C for 15 minutes. Crystal structure and ionic conductivity characterization of the water exposed specimen were conducted using the same method as the pristine specimen, and the results are shown in Figure S35. Results of both characterizations indicated LSTNZH (x = 9/16) to be moisture insensitive.

To mechanically polish the TEM specimen, bulk pellets were first cut into rectangular blocks by a diamond saw. The rectangular blocks were 3 mm by 2 mm in area and were cut to the least possible thickness (typically ~0.5 mm). Then, a single rectangular piece was placed on an Allied Multiprep Polishing System, thinned, and fine-polished against diamond lapping films (Ted Pella, Inc.) of various grit sizes. Since we have found LSTNZH (x = 9/16) to be moisture insensitive, this procedure was performed with water. The thinned ceramic was glued to a molybdenum ring (Structure Probe, Inc.) with M-Bond 610 epoxy (Vishay Precision Group, Inc.). The polished pieces were then ion-milled under Ar gas for finer polishing using a Gatan model 695 Precision Ion Polishing System.

Computation Methods and Simulations

Figure S37 displays the flowchart for the training and validation of MTP to study bulk and GB models of LSTNZS (*y* = 9/16). In the first step, we generated an initial training set for LSTNZS (*y* = 9/16). A $3 \times 3 \times 2$ supercell with 175 atoms were generated from a primitive cell with space group of Pm$\bar{3}$m. The distribution of cations was randomly assigned with the SQS code. AIMD simulations using NVT ensemble were carried out on the relaxed supercell, wherein simulations were performed at three strains (0, ±0.05) and four temperatures (300 K to 1200 K with 300 K intervals). Snapshots were extracted from a production run of 5 ps at 0.1 ps intervals, i.e., 50 structures for each temperature and strain, resulting in a total of 600 training structures (50 × 4 temperatures × 3 strains). Static self-consistent calculations were performed on the training structures to obtain accurate energies, forces, and stresses for active learning moment tensor potential (MTP) training. The convergence criteria are the same as our prior work in LSTZ.[S9]

In the second step, we use two stages of active learning to optimize the pretrained MTP for MD and MC/MD simulations. Our MTP model complexity was set with the level of max (lev$_{\max}$) and the radial basis size equal to 12 and 8, respectively, while the cutoff radius was set as 5 Å, and the relative weights of energies, forces and stresses was set as 100:1:0.1, in line with previous studies.[S10,S11] In each active learning stage, the MTP was iteratively optimized in scenarios where the MTP will eventually be used. These trial simulations were terminated if structures with γ over the break threshold, γ_{break}, emerge, and structures with γ over the select threshold, γ_{select}, will be added into the training set, with which a new MTP is fitted. This iterative loop is repeated until the trained MTP can complete a simulation without the emergence of structures above γ_{break}. In the first stage of active learning, the "early break" strategy, i.e., $\gamma_{break} = \gamma_{select}$ = 20 was used so that the MTP can complete 100 ps NPT simulation for the bulk supercell without breaking after 186 iterations. Furthermore, a stricter strategy, $\gamma_{break} = \gamma_{select}$ = 5 was applied until the 295th iteration, where the MTP can reliably complete 100 ps NPT simulation up to 1200 K (Figure S38). In the second stage, the MTP was improved with a "loose break" strategy, i.e., the γ_{break} and γ_{select} were set as 20 and 5, respectively. Hybrid Monte Carlo/molecular dynamics (MC/MD) simulations were done to two low-sigma GBs, i.e., symmetric tilt $\Sigma3[110](1\bar{1}1)$ GB and simple twist $\Sigma3[110](110)$ GB. For the MC runs, a swap attempt was evaluated by the Metropolis criterion at every timestep, where swaps between Li/Sr on A-sites and swaps between Ta/Nb/Zr/Sn on B-sites, i.e., seven distinguishable atom pairs, were considered. After 22 iterations (Figure S38), the MTP was able to reliably perform 50 ps MC/MD simulations up to 2100 K, and the GB energies γ_{GB} were converged to within 0.15 J/m2 of DFT values (Figure S39).

In the third step, the active learning MTP was verified to reproduce the training energies, forces and stresses with mean absolute errors (MAEs) of 3.68 meV/atom, 0.19 eV/Å and 2.54 meV/Å^3, comparable to our previous works.[S12] A test set of 880 structures were generated from 1 ns MD and MC/MD simulations at a range of target temperatures to verify the accuracy of MTP for long time simulation of target scenarios. The MAEs of test energies, forces and stresses were 4.57 meV/atom, 0.21 eV/Å and 2.69 meV/Å^3, consistent to the respective training MAEs, which shows little sign of overfitting or underfitting (Figure S40). Meanwhile, the predicted GB energies by DFT were reproduced by the MTP with absolute errors within 0.15 J/m^2. We then apply this verified MTP for Large scale and longtime MD simulations. A $6 \times 6 \times 4$ supercell with 700 atoms were generated from a primitive cell with space group of Pm$\bar{3}$m as the bulk model. GB models were constructed for four low-sigma GB orientations, i.e., simple twist $\Sigma3$[110](110), symmetric tilt $\Sigma3$[110](1$\bar{1}$1), simple twist $\Sigma5$[100](100), and symmetric tilt $\Sigma5$[100](0$\bar{1}$2). The interfacial distances between the two GB cores in each GB model were over 40 Å. The GB models and their dimensions are shown in Figure 5A and Table S9, respectively. MC/MD simulations were performed to bulk and GB models at the experimental calcination temperature of 1573 K, with the same settings as those used in the second stage of active learning. Next, MD simulations were performed to both bulk and GB models to study Li-ion diffusion in LSTNZS (*y* = 9/16). The simulations were performed at 300 to 1000 K with 50 and 100 K intervals below and above 500 K, respectively. To collect sufficient Li-ion diffusion at lower temperatures, the simulation times were set as 10 ns and 2 ns at below and above 400 K, respectively. At each temperature, five parallel MD runs were performed with randomly generated initial speeds, to average out the effect of different initial states. The NPT ensembles were used, and the timestep was set as 1 fs. The methods of calculation of Li diffusivity at bulk and GB regions were same as those in our previous works.[S12]

All DFT calculations were performed using the Vienna ab initio simulation package (VASP) with the projector augmented-wave (PAW) approach.[S13] The Perdew-Burke-Ernzerhof (PBE) generalized gradient approximation (GGA) was used as the exchange-correlation functional.[S14,S15] The PBE functional was verified in our previous work to have comparable accuracy with the optB88-vdW functional[S16,S17] in terms of matching the experimental lattice constants, lattice expansion and room temperature ionic conductivities of the perovskite LLTO.[S18] All DFT and *ab initio* molecular dynamics (AIMD) simulations were carried out using fully automated workflows built on the Python Materials Genomics (pymatgen) library and the FireWorks scientific workflow package.[S19–S21]

Supplemental References

S1. Hielscher, R., and Schaeben, H. (2008). A novel pole figure inversion method: specification of the MTEX algorithm. J. Appl. Crystallogr. *41*, 1024–1037.

S2. Xu, C., Lindgren, F., Philippe, B., Gorgoi, M., Björefors, F., Edström, K., and Gustafsson, T. (2015). Improved Performance of the Silicon Anode for Li-Ion Batteries: Understanding the Surface Modification Mechanism of Fluoroethylene Carbonate as an Effective Electrolyte Additive. Chem. Mater. *27*, 2591–2599.

S3. Shannon, R.D. (1976). Revised effective ionic radii and systematic studies of interatomic distances in halides and chalcogenides. Acta Crystallogr. Sect. A *32*, 751–767.

S4. Van Dijk, T., and Burggraaf, A.J. (1981). Grain boundary effects on ionic conductivity in ceramic $Gd_xZr_{1-x}O_{2-(x/2)}$ solid solutions. Phys. status solidi (a) *63*, 229–240.

S5. Zeng, A.Y., Ouyang, B., Liu, J., Byeon, Y., Cai, Z., and Lincoln, J. (2022). High-entropy mechanism to boost ionic conductivity. *1324*, 1320–1324.

S6. Pennycook, S.J. (1992). Z-Contrast Transmission Electron Microscopy: Direct Atomic Imaging of Materials. Annu. Rev. Mater. Sci. *22*, 171–195.

S7. Saitoh, M., Gao, X., Ogawa, T., Ikuhara, Y.H., Kobayashi, S., Fisher, C.A.J., Kuwabara, A., and Ikuhara, Y. (2018). Systematic analysis of electron energy-loss near-edge structures in Li-ion battery materials. Phys. Chem. Chem. Phys. *20*, 25052–25061.

S8. Gao, X., Fisher, C.A.J., Ikuhara, Y.H., Fujiwara, Y., Kobayashi, S., Moriwake, H., Kuwabara, A., Hoshikawa, K., Kohama, K., Iba, H., et al. (2015). Cation ordering in A-site-deficient Li-ion conducting perovskites $La_{(1-x)/3}Li_xNbO_3$. J. Mater. Chem. A *3*, 3351–3359.

S9. Lee, T., Qi, J., Gadre, C.A., Huyan, H., Ko, S.-T., Zuo, Y., Du, C., Li, J., Aoki, T., Wu, R., et al. (2023). Atomic-scale origin of the low grain-boundary resistance in perovskite solid electrolyte $Li_{0.375}Sr_{0.4375}Ta_{0.75}Zr_{0.25}O_3$. Nat. Commun. *14*, 1940.

S10. Novikov, I.S., Gubaev, K., Podryabinkin, E. V, and Shapeev, A. V (2020). The MLIP package: moment tensor potentials with MPI and active learning. Mach. Learn. Sci. Technol. *2*, 025002.

S11. Shapeev, A. V (2016). Moment Tensor Potentials: A Class of Systematically Improvable Interatomic Potentials. Multiscale Model. Simul. *14*, 1153–1173.

S12. Lee, T., Qi, J., Gadre, C.A., Huyan, H., Ko, S.-T., Zuo, Y., Du, C., Li, J., Aoki, T., Stippich, C.J., et al. (2022). Atomic-scale origin of the low grain-boundary resistance in perovskite solid electrolytes. arXiv Prepr. arXiv:2204.00091.

S13. Blöchl, P.E. (1994). Projector augmented-wave method. Phys. Rev. B *50*, 17953–17979.

S14. Kresse, G., and Furthmüller, J. (1996). Efficient iterative schemes for ab initio total-energy calculations using a plane-wave basis set. Phys. Rev. B *54*, 11169.

S15. John P. Perdew, Kieron Burke, and M.E. (1996). Generalized Gradient Approximation Made Simple. Phys. Rev. Lett. *77*, 3865–3868.

S16. Klimeš, J., Bowler, D.R., and Michaelides, A. (2011). Van der Waals density functionals applied to solids. Phys. Rev. B - Condens. Matter Mater. Phys. *83*, 1–13.

S17. Klimeš, J., Bowler, D.R., and Michaelides, A. (2010). Chemical accuracy for the van der Waals density functional. J. Phys. Condens. Matter *22*, 022201.

S18. Qi, J., Banerjee, S., Zuo, Y., Chen, C., Zhu, Z., Holekevi Chandrappa, M.L., Li, X., and Ong, S.P. (2021). Bridging the gap between simulated and experimental ionic conductivities in lithium superionic conductors. Mater. Today Phys. *21*, 100463.

S19. Deng, Z., Zhu, Z., Chu, I.H., and Ong, S.P. (2017). Data-driven first-principles methods for the study and design of alkali superionic conductors. Chem. Mater. *29*, 281–288.

S20. Ong, S.P., Richards, W.D., Jain, A., Hautier, G., Kocher, M., Cholia, S., Gunter, D., Chevrier, V.L., Persson, K.A., and Ceder, G. (2013). Python Materials Genomics (pymatgen): A robust, open-source python library for materials analysis. Comput. Mater. Sci. *68*, 314–319.

S21. Jain, A., Ong, S. P., Chen, W., Medasani, B., Qu, X., Kocher, M., ... & Persson, K.A. (2015). FireWorks: a dynamic workflow system designed for high-throughput applications. Concurr. Comput. Pract. Exp. *27*, 5037–5059.